

COPYRIGHT WARNING

This paper is protected by copyright. You are advised to print or download **ONE COPY** of this paper for your own private reference, study and research purposes. You are prohibited having acts infringing upon copyright as stipulated in Laws and Regulations of Intellectual Property, including, but not limited to, appropriating, impersonating, publishing, distributing, modifying, altering, mutilating, distorting, reproducing, duplicating, displaying, communicating, disseminating, making derivative work, commercializing and converting to other forms the paper and/or any part of the paper. The acts could be done in actual life and/or via communication networks and by digital means without permission of copyright holders.

The users shall acknowledge and strictly respect to the copyright. The recitation must be reasonable and properly. If the users do not agree to all of these terms, do not use this paper. The users shall be responsible for legal issues if they make any copyright infringements. Failure to comply with this warning may expose you to:

- Disciplinary action by the Vietnamese-German University.
- Legal action for copyright infringement.
- Heavy legal penalties and consequences shall be applied by the competent authorities.

The Vietnamese-German University and the authors reserve all their intellectual property rights.



Impact of various filling fractions and diffuser densities in the MBBR process on the oxygen transfer rate of fine-bubble aeration systems – Oxygen Transfer Tests in a glass test tank



Vietnamese - German University

Master Thesis in Water Technology, Water Reuse and Water Management

Thinh VO Truong

Department of Civil and
Environmental Engineering



TECHNISCHE
UNIVERSITÄT
DARMSTADT

Institute IWAR
Chair of Wastewater Technology

IWAR



Vietnamese - German University

Thinh VO Truong

21021001

Master thesis to achieve the academic title of Master of Science in Water Technology, Water Reuse and Water Management

Title: Impact of various filling fractions and diffuser densities in the MBBR process on the oxygen transfer rate of fine-bubble aeration systems - Oxygen Transfer Tests in a glass test tank

Working time: 08.05.2023 - 27.11.2023

Supervisor: M.Sc. Jana Trippel

Thesis supervisor: Prof. Dr.-Ing. habil. Martin Wagner

Technische Universität Darmstadt

Task Formulation

Preliminary theoretical considerations

- Fundamentals of the MBBR process
- Usual air flow rates and filling fractions in the MBBR process. Classification of dynamic wet pressures (DWP) with commonly used scales.
- Representation of mass transfer at the gas-liquid interface
- Bubble formation and rise
- Compilation of previous knowledge regarding oxygen transfer in the MBBR Process

Practical work

- Carrying out oxygen transfer and pressure loss tests of 2 different fine-bubble discs diffusers (2 slit lengths) in clean water with variation of the air flow rate, diffuser density as well as with different filling fractions of the carriers.

Presentation and evaluation of the results

- Evaluation and presentation of the test results obtained
- Determination of the dependency between the filling fraction, diffuser density and type of the disc diffusers on oxygen transfer
- Evaluation of the results regarding the variation of the different parameters of the experimental set-up on oxygen transfer
- Discussion of the results obtained in connection with the fundamentals of oxygen transfer in a MBBR reactor and conclusions with respect to oxygen transfer.

Abstract

Increasing demands on the treatment performance of municipal wastewater treatment plants have led to a continuous increase in space requirements and annual costs associated with the conventional activated sludge (CAS) process. Biofilm process, particularly Moving Bed Biofilm Reactor Process (MBBR), has emerged as a solution to address such challenges. In the MBBR process, very small, strongly structured plastic media are introduced to provide sites for biofilm growth. However, the main disadvantage of the MBBR process relates to the poor aeration energy efficiency while the oxygen requirement of at least double or even quintuple compared to the CAS process. Subsequently, it is an urgent need for research to optimize the oxygen transfer efficiency (OTE) in the MBBR process. The aim of this study is to investigate the impacts of various filling fractions and diffuser densities on the oxygen transfer rate of fine-bubble aeration systems. To achieve this objective, several experiments using two types of disc diffusers have been conducted in lab- and pilot-scale. The results revealed that the addition of carriers increased gas holdup yet decreased oxygen transfer efficiency in both scales. This could be attributed to two main factors: the vertical rotation of the carriers and the characteristics of the carrier media. The findings highlighted the OTE was affected not only by the filling fraction of the carriers and the diffuser density, but also governed by other aspects such as the properties of the aeration system, the properties of the carrier media, the reactor geometry, and the hydraulic pattern within the reactor.



Vietnamese - German University

Table of content

Task Formulation	iii
Abstract	iv
Table of content	v
List of Abbreviations	vii
List of Figures	viii
List of Tables	ix
1. Introduction	1
2. Preliminary theoretical considerations	2
2.1 Fundamentals of the MBBR process.....	2
2.1.1 Basic concepts of the MBBR technology.....	2
2.1.2 Performance of the MBBR technology	5
2.1.3 Advantages and Disadvantages of the MBBR technology.....	8
2.2 Air flow rates and filling fractions in the MBBR process.....	9
2.2.1 Filling fractions	9
2.2.2 Air flow rates.....	9
2.2.3 Classification of dynamic wet pressures with commonly used scales	11
2.3 Mass transfer at the gas-liquid interface.....	12
2.4 Bubble formation and rise	17
2.4.1 Coarse-bubble systems.....	17
2.4.2 Fine-bubble systems	19
2.4.3 Bubble formation and rise.....	20
2.5 Literature review on the oxygen transfer in the MBBR Process.....	26
3. Materials and methods	27
3.1 Experimental setup.....	27
3.1.1 Lab scale.....	27
3.1.2 Pilot scale	29
3.2 Determination of important parameters	31
4. Results	35
4.1 Lab scale.....	35
4.2 Pilot scale	38
5. Discussion and outlook	43
5.1 Effect of the carrier media on the oxygen transfer efficiency	43
5.2 Effect of the reactor geometry on the oxygen transfer efficiency	44
5.3 Effect of the diffuser density on the oxygen transfer efficiency	46
5.4 Effect of the effective water volume on the oxygen transfer efficiency	46

5.5	Limitation of the HPOD method	47
5.6	Future development of the carrier media	48
6.	Conclusion.....	50
7.	Appendix.....	52
7.1	Appendix A: Literature review.....	52
7.1.1	Bubble shape and rise velocity of a single bubble	52
7.1.2	Force balance at the bubble surface	54
7.1.3	MBBR systems configurations for different biological treatment goals	55
7.2	Appendix B: Experiment.....	57
7.2.1	Weekly schedules for lab- and pilot-scale experiments	57
7.2.2	Evaluating the test quality	59
7.2.3	Determination of the carrier's bulk volume and the effective water volume	60
7.2.4	Determination of the blower frequency for reaching the target airflow rate.....	63
7.2.5	Determination of the diffuser density.....	64
7.2.6	Determination of the carrier's voidage.....	67
	Bibliography	68
	Affidavit	74



Vietnamese - German University

List of Abbreviations

APX	:	Appendix
BOD	:	Biochemical Oxygen Demand
CAS	:	Conventional Activated Sludge
COD	:	Chemical Oxygen Demand
DD	:	Diffuser Density
DO	:	Dissolved Oxygen
DWP	:	Dynamic Wet Pressure
FF	:	Filling Fraction
HPOD	:	High Purity Oxygen Desorption
HRT	:	Hydraulic Retention Time
IFAS	:	Integrated Fixed-film Activated Sludge
MBBR	:	Moving Bed Bioreactor
OLR	:	Organic Loading Rate
PSA	:	Protected Surface Area
SALR	:	Surface Area Loading Rate
SARR	:	Surface Area Removal Rate
SGV	:	Superficial Gas Velocity

List of Figures

Figure 1. Working principle of moving bed biofilm reactor in aerobic and anoxic process.	3
Figure 2. Components of an oxygen transfer system of an aerobic MBBR system.	4
Figure 3. Drawing of a Standard DWP Measuring Setup.	12
Figure 4. Schematic representation of the gas–liquid interface according to two-film theory.	13
Figure 5. Comparison of the gas-liquid interface areas of large and small bubbles.	14
Figure 6. Typical changes of oxygen concentration with respect to time for the HPOD method.	16
Figure 7. Graph of natural logarithm of various DO concentrations versus experiment time to determine kLa.	17
Figure 8. Comparison of fine (left photograph) and coarse (right photograph) bubbles generated by two different aerators operating at the same airflow rate in the same surfactant solution.	19
Figure 9. Flow regimes for vertical channels, two-phase flow.	23
Figure 10. Schematic diagram of bubble coalescence mechanisms.	23
Figure 11. Schematic diagram of bubble breakup mechanisms.	24
Figure 12. Relative rise velocity of a bubble swarm.	25
Figure 13. Schematic drawing of the lab-scale MBBR.	28
Figure 14. Experimental setup of the lab-scale MBBR with the HXF25KLL carrier.	29
Figure 15. Schematic drawing of the pilot-scale MBBR.	30
Figure 16. Experimental setup of the pilot-scale MBBR.	31
Figure 17. Effects of carrier media on mass transfer coefficient and gas holdup in lab-scale experiments.	36
Figure 18. Effects of carrier media on the specific standard oxygen transfer efficiency in lab-scale.	37
Figure 19. Impact of airflow rates on the specific standard oxygen transfer efficiency in lab-scale.	37
Figure 20. Effects of carrier media on mass transfer coefficient.	39
Figure 21. Effects of carrier media on mass transfer coefficient, standard oxygen transfer efficiency and gas holdup	40
Figure 22. Impact of filling fraction on the specific standard oxygen transfer efficiency in pilot-scale.	41
Figure 23. Impact of airflow rates on the specific standard oxygen transfer efficiency in pilot-scale.	42
Figure 24. Comparison of the bubble plumes with different depths of submerge.	45
Figure APX 1. Grace Diagram for bubble shapes and bubble rise velocity.	52
Figure APX 2. Force balance at the bubble surface.	54
Figure APX 3. Course of the oxygen content (above) and the Residuals (below) over the measurement time. ..	59
Figure APX 4. Course of the residuals of the oxygen content in a good test (top) and in a failed test (bottom)..	60
Figure APX 5. The relationship between the mass and the solid volume of the carriers.	61
Figure APX 6. Comparison of operating airflow rate and standard airflow rate for setting blower frequency	63
Figure APX 7. Comparison of the effective areas for Disc 1 and Disc 2.	64
Figure APX 8. Comparison of the effective areas of Disc 1 and 2 with multiple air flow rates	65

List of Tables

Table 1 Investigated airflow rate ranges by different research	11
Table 2. DWP values for certain diffuser types.	12
Table 3. Characteristic bubble shapes, depending on the bubble diameters.	21
Table 4. Comparison of the SOTE in clean water with different research	45
Table 5. Comparison between SSOTE using effective water volume and total liquid volume.....	47
Table 6. Comparison of the SOTE development with various PSA from different research.	49
Table APX 1: MBBR systems configurations for different biological treatment goals.....	55
Table APX 2. Weekly schedule for lab-scale experiments.	57
Table APX 3. Weekly schedule for pilot-scale experiments.....	57
Table APX 4. Investigation of the relationship between the number of carriers, their mass and solid volume ...	60
Table APX 5. Relationship between the effective water volume and filling fraction	62
Table APX 6. Investigation of the relationship between the blower frequency and the target airflow rate	63
Table APX 7. Selected blower frequency for pilot-scale experiments.....	64
Table APX 8. Diffuser densities with different airflow rates for Disc 1 and 2 in lab-scale experiments.....	66
Table APX 9. Diffuser densities with different airflow rates for Disc 1 in pilot-scale experiments	66



Vietnamese - German University

1. Introduction

Increasing demands on the treatment performance of municipal wastewater treatment plants (WWTP) have led to the fact that the space requirements and the annual costs for the conventional activated sludge (CAS) process have continued to rise. Alternative wastewater treatment processes have therefore established over time. These include biofilm processes such as the Moving Bed Biofilm Reactor Process (MBBR). In this process, very small, strongly structured plastic media (diameter approx. 25 mm) with a density of just under 1.0 g/cm³ are introduced to provide sites for biofilm growth. In 2009, more than 600 MBBRs were operating in 50 different countries. The primary drawback of the MBBR process is the heightened oxygen demand, typically double or even quintuple in comparison with the CAS process, which poses challenges for energy consumption (Ødegaard, 2006; Metcalf & Eddy Inc. et al., 2013). It is of note that the aeration system always accounts for the largest energy consumer in a WWTP (up to 55.6%), making it an urgent need for research on optimizing the oxygen transfer efficiency in the MBBR process.

Some scientific publications on a laboratory scale have demonstrated that the addition of the carriers improves oxygen transfer efficiency. However, the impacts of filling fractions, diffuser densities and disc diffusers remain controversial or unknown. In this master thesis, oxygen transfer tests in clean water with a variation of the experimental set-up are to be conducted in order to better understand the oxygen transfer in an MBBR reactor and to be able to derive common aeration parameters for this process.



Vietnamese - German University

2. Preliminary theoretical considerations

This section encompasses a comprehensive analysis of various facets associated with the MBBR process. It begins with a thorough presentation of the fundamentals of the MBBR process, encompassing its principles, technological advancements, operational parameters, and design considerations. Subsequently, critical factors such as airflow rates, filling fractions, and dynamic wet pressure, which play critical roles in optimizing the performance and efficiency of MBBR systems, are presented. Additionally, this section delves into the theories and mechanisms underlying mass transfer and bubble formation in MBBR processes, shedding light on the intricacies of oxygen and substrate transfer within the biofilm and liquid phases. Finally, a review of the current literature will highlight the latest research findings on oxygen transfer within MBBR wastewater treatment. This comprehensive exploration serves as a valuable introduction, imparting initial insights and knowledge that contribute to the subsequent experimental section.

2.1 Fundamentals of the MBBR process

2.1.1 Basic concepts of the MBBR technology

In recent years, a great number of wastewater treatment plants (WWTPs) have been constructed or renovated to meet the increasing wastewater discharges and to comply with more stringent regulations. The main challenges lie in space availability and/or rising operating costs. Hence, the introduction of new technologies is essential to address such challenges. Biofilm processes, in particular, MBBRs are among the emerging technologies. First invented in 1989 by Prof. Hallvard Ødegaard and his co-workers from the Norwegian University of Science and Technology (NTNU), the MBBR process aimed to provide a compact biological nitrogen removal process to reduce point-source discharges of nitrogen to the North Sea (Metcalf & Eddy Inc. et al., 2013, p. 1016). Since then, the number of real-scale WWTPs adopting MBBR technology increased quickly worldwide to treat a wide range of wastewater such as municipal wastewater (di Biase et al., 2019), paper mill wastewater (Mayra et al., 2016), coal gasification wastewater (Zhuang et al., 2014), and pharmaceutical industry wastewater (Tang et al., 2017), etc. It is reported that there were 400 MBBR plants in 22 countries in 2006 (Rusten et al., 2006, p. 323) while by 2014, the number had tripled, reaching 1200 MBBR plants in 50 countries (Biswas et al., 2014, p. 1).

The MBBR process is defined as “a continuous flow process which uses small carrier elements to provide sites for active bacteria attachment in a suspended growth medium” (Collivignarelli et al., 2019, p. 10727). The addition of the carrier media promotes a higher biomass amount in the reactor, prevents biomass from washing out, and achieves higher sludge retention time and superior efficiency of nitrification and denitrification processes without increasing the reactor size and biomass recirculation (Englande et al., 2015; Dias et al., 2018; Liu et al., 2021). The excess biomass detaches from the carriers and then exits with the effluent. The reactors can be operated aerobically, anoxically or anaerobically (Madan et al., 2022, p. 2). In whichever application, the biofilm carriers inside must be maintained in suspension. This can be achieved by using air diffusers in aerobic processes or by mechanical agitators in anoxic/anaerobic processes (Safwat, 2019; Madan et al., 2022), which can be demonstrated in Figure 1.

The MBBR scheme comes in many variants that can be used for BOD/COD removal, biological nitrification and biological nitrogen removal (WEF, 2011; Metcalf & Eddy Inc. et al., 2013). Generally, preliminary treatment (e.g. screening, sieving and grit removal) is required upstream MBBR reactors to remove coarse and fine materials that can subsequently accumulate in the carrier media. The variants of the process can be found in Table APX 1. As shown in Table APX 1, the MBBR systems share a relatively similar design with the Integrated Fixed-film Activated Sludge (IFAS) method (Kawan et al., 2016). Aqeel and Liss (2022) defined the IFAS process as “a hybrid process that employs both attached biomass (biofilms developed carrier media) and suspended-biomass growth (flocs) for biological nutrient removal”. As revealed from the definition, the main difference between the two processes is that the MBBR processes do not require activated sludge recirculation. Further differences are a higher biofilm carrier density in the MBBR system (up to 70% filling fraction) and increased suspended mixed liquor or biomass concentration (Metcalf & Eddy Inc. et al., 2013).

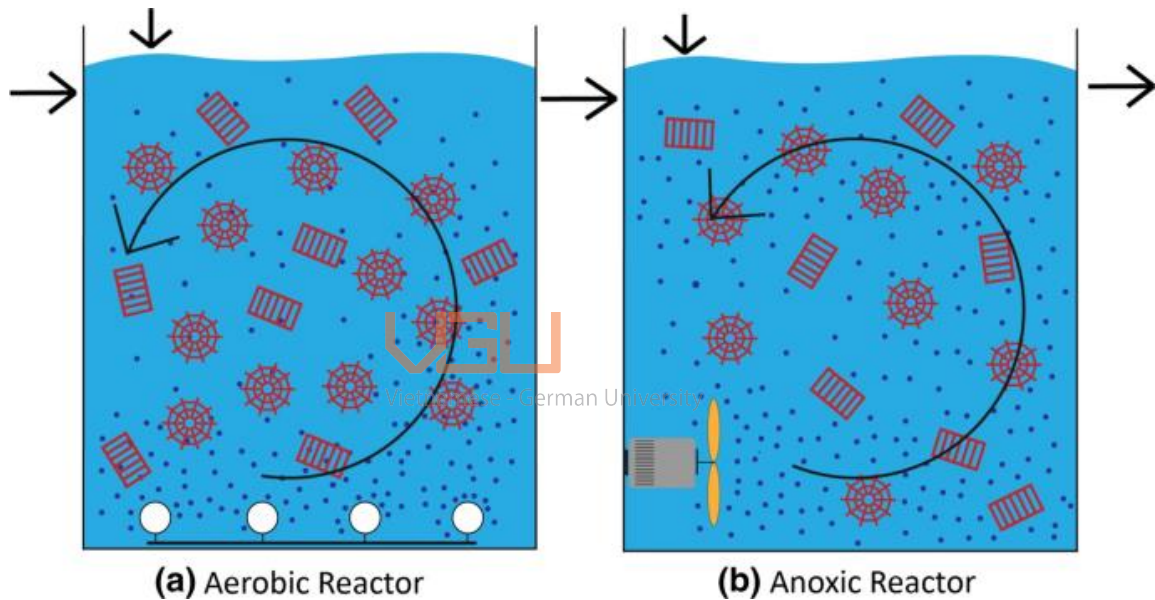


Figure 1. Working principle of moving bed biofilm reactor in aerobic and anoxic process.

Source: Madan et al. (2022)

In this study, only aerobic MBBR systems will be discussed. The first aspect of an MBBR system is the oxygen transfer system – an engineered system that employs a network of pipes and diffusers to serve two basic functions: (1) delivering sufficient airflow to meet the oxygen requirement and (2) providing a rolling water circulation pattern for the uniform distribution of the submerged plastic biofilm carriers. The components of the oxygen transfer system consist of manually operated airflow control valves, drop pipes, manifolds (or submerged air headers), and perforated pipe distributors (or diffusers), which can be found in Figure 2 (Daigger & Boltz, 2018). As shown in Figure 2, low-pressure air is initially introduced to drop pipes that connect to manifolds or air headers. Each drop pipe is equipped with manually modulated airflow control valves to control dissolved oxygen concentration and the number of drop pipes is determined based on the airflow rate requirements. Then, the air is released through orifices on diffusers, of which the size must be smaller than the smallest dimension of the plastic biofilm carrier to avoid orifice clogging. Typically, the diffusers are positioned approximately 0.30 m above the

tank bottom with spacing options of 0.30, 0.45, 0.60, or 0.90 m between each diffuser. A series of connected perforated pipes or diffusers is called a grid. The maximum distance between grids is generally limited to 1.83 m, while the minimum distance from the basin wall is 0.90 m (although 0.45 m is preferred). It is important to ensure that the installed aeration grids are leveled within 6.5 mm (0.25 in.) (Daigger & Boltz, 2018).

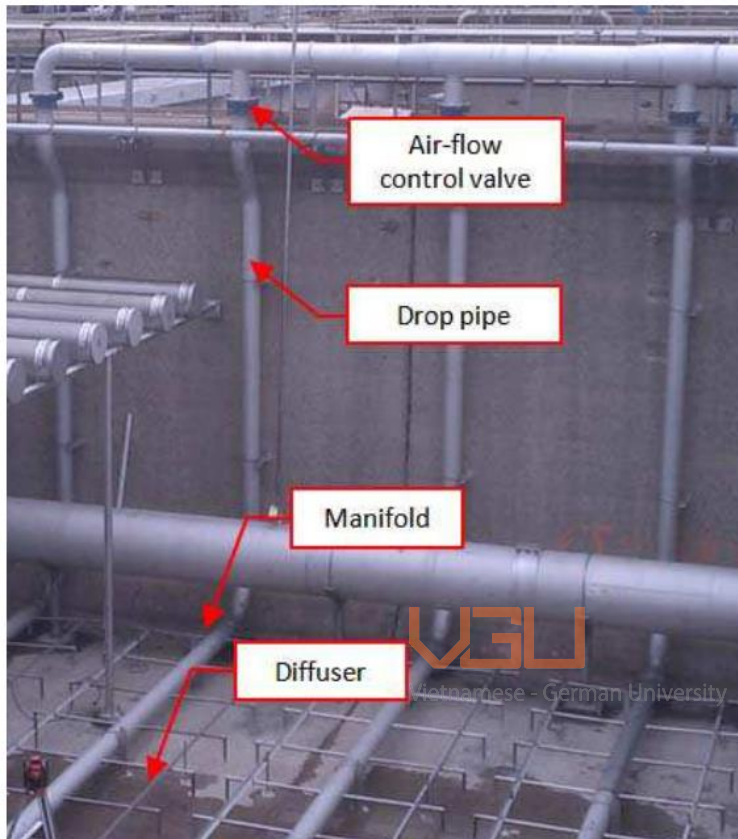


Figure 2. Components of an oxygen transfer system of an aerobic MBBR system.

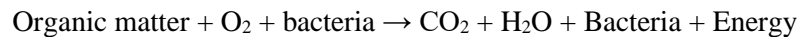
Source: Daigger and Boltz (2018)

Another important aspect contributing to a successful MBBR system is the carrier media (Kawan et al., 2016). The carrier media in the MBBR systems come in different configurations. They vary in shape (cylindrical and spherical), size, materials, voidage and protected surface area (WEF, 2011; Dias et al., 2018). Currently, the most widely used carrier media found carry cylindrical shapes with hollow inside and fins/ribs along the outside of the carrier (WEF, 2011; Safwat, 2019). Fins/ribs help minimize frictions between carriers with other carriers or with the reactor walls, as well as preserve the external biofilm (Safwat, 2019). The carrier media have a common size of 25 mm diameter and 5÷7mm height (Metcalf & Eddy Inc. et al., 2013). Additionally, it is suggested that the density of carriers should be close to the density of the containing liquid or water to allow their free movement in the liquid (Martínez-Huerta et al., 2009; Kawan et al., 2016) and less bound to the downstream screens (Metcalf & Eddy Inc. et al., 2013). Hence, the preferable material for the media is high density polyethylene (HDPE) due to its plasticity, durability, and close density to water ($0.95 - 0.98 \text{ g/cm}^3$) (WEF, 2011; Madan et al., 2022). In recent years, research for new materials is ongoing as plastic has been reported to cause a slow growth

and an easy detachment of biofilms due to its low hydrophilicity and poor biological affinity (Chen et al., 2012). Some notable suggested material modifications for the carriers are diatomaceous earth (Zhao et al., 2006), chemical oxidation-surface covering with ferric ion (CO-SCFe) or grafting with gelatin (CO-SGG) (Chen et al., 2012), activated carbon fiber felt and polymer fiber (Zhou, 2013), and calcium modified basalt fiber (Gao et al., 2021), etc. Last but not least, the protected surface area (PSA) of the biofilm carriers should not be neglected. The PSA is defined as “the surface area available for the biofilm to grow protected from carrier collision and shear force and is commonly used as a design and operational parameter in moving attached growth systems” (Dias et al., 2018). The PSA is estimated at the macroscopic scale with photography and is commonly in the range of 500-700 m²/m³ (Metcalf & Eddy Inc. et al., 2013). The selection of the PSA is based on which condition (aerobic or anoxic/anaerobic) the carriers operate (Madan et al., 2022). Aerobic systems, for instance, require a rapid growth of heterotrophic biofilm, thus carriers with wider openings (e.g. AnoxKaldnes K1 or K3) are selected to minimize protected surface area loss. By contrast, media with small openings and large protected surface area (e.g. Biofilm Chip M) will benefit the slow-growing autotrophic microbial biofilm in nitrification and anammox processes.

2.1.2 Performance of the MBBR technology

Carbonaceous BOD/COD Removal. The MBBR technology offers a high COD/BOD treatment capacity for diverse wastewater streams. It promotes fast degradation of biodegradable and soluble organic matter whereas particulate organic matter can be retained by the irregularities of the attached biomass before being hydrolyzed and subsequently degraded (WEF, 2011). The degradation of organic carbon compounds under aerobic, heterotrophic bacteria is depicted by the following equation (Von Sperling, 2007c, 2007b):



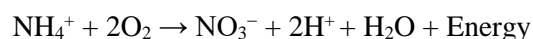
In fact, much research has reported on the outstanding COD removal rate of the MBBR technology, including municipal wastewater (around 90%) (Ødegaard, 2006), coking wastewater (89%) (Gu et al., 2014), tannery wastewater (90%) (Goswami & Mazumder, 2016), textile wastewater (98.5%) (Sari Erkan et al., 2020), coal gasification wastewater (74.6%) (Zhuang et al., 2014), etc. For the purpose of carbonaceous matter removal only, the dissolved oxygen (DO) concentration of 2 – 3 mgO₂/l and the hydraulic retention time (HRT) of 15 – 90 minutes are required (Ødegaard, 2006). Madan et al. (2022) found that the COD removal efficiency decreased by 13% once the DO level decreased from 2 to 1 mg/L while it increased by 5.8% when the DO level increased from 2 to 6 mg/L. This example demonstrates that DO concentration acts as a limiting factor, thus monitoring the DO levels and making necessary adjustments to the airflow rate can guarantee optimal performance.

Various biophysical design parameters are recommended for COD/BOD removal, including surface area loading rate (SALR), surface area removal rate (SARR) or organic loading rate (OLR) (WEF, 2011; Magdum & V, 2019). The SALR, for example, is selected based on both treatment objectives (whether only COD/BOD removal or with/without nitrification/denitrification) and methods selected for solids separation (Safwat, 2019). The SALR value can be estimated by dividing the removal flux by the

estimated treatment efficiency (Metcalf & Eddy Inc. et al., 2013), however, it should not exceed 30 g soluble COD/m²d, otherwise, there will be an inhibition of the biomass (Ødegaard, 2006). According to WEF (2011) and Safwat (2019), depending on the SALR value, the MBBR process for COD/BOD removal is classified into three designs: low-rate MBBR (< 5 g BOD₇/m²d), normal-rate MBBR (5-15 g BOD₇/m²d) and high-rate MBBR (> 20 g BOD₇/m²d) at 15°C. The low-rate MBBR design is adopted in case of downstream nitrogen removal is required. The most widely-used design is the normal rate MBBR (Metcalf & Eddy Inc. et al., 2013) that involves multiple MBBR reactors operating in series, which are possible followed by chemical additions and flocculation for phosphorus removal and solids separation (Magdum & V, 2019; Safwat, 2019). The use of multiple MBBR reactors in series aims to provide high rate BOD uptake and a low soluble BOD prior to nitrification, thus improving downstream ammonia removal efficiency and process stability, as well as minimizing reactor volume, media requirements, and the possibility of short-circuit flow (Metcalf & Eddy Inc. et al., 2013). The BOD removal efficiency of the normal rate design is expected to be over 80% (WEF, 2011). The high-rate MBBR design is typically applied for industrial wastewater treatment or biological pretreatment (Metcalf & Eddy Inc. et al., 2013) with the main objective of removing the soluble and easily biodegradable BOD (Safwat, 2019). Typically, the BOD removal efficiency of the high-rate design ranges between 75% and 80% (WEF, 2011). There is an issue with high-rate MBBR systems so-called “sloughed solids” (Ødegaard et al., 2000). Sloughing means the detachment of biomass from the media, which, in turn, causes the biomass suspended in the effluent and is later removed in the secondary clarifier as sludge. At a high SALR level, the sloughed solids from the media tend to be more dispersed and have poor settling characteristics in the secondary clarifier (Ødegaard et al., 2000). As a result, the addition of chemicals (e.g. coagulants and/or flocculants) before secondary clarifiers is necessary to remove solids, thus enhancing the settling capacity in the secondary clarifier (Ødegaard, 2006).

Nitrogen removal. In addition to carbonaceous matter removal, the addition of nitrification and denitrification processes to the process scheme is required to achieve discharge regulations. In practice, a high nitrification efficiency (ammonia concentration of less than 1.0 mg/L in the effluent) can be achieved by installing nitrification reactors in series (Metcalf & Eddy Inc. et al., 2013). The design of nitrification reactors in series also minimizes reactor volume and media addition (Metcalf & Eddy Inc. et al., 2013). At the pilot scale, average loading rates of up to 1.17g NH₄-N/m²d were observed to maintain an effluent concentration of < 1 mg NH₄-N/l (Ødegaard, 2006).

In the nitrification process, ammonium is oxidized by aerobic, autotrophic bacteria to form nitrate, which is depicted by the overall equation as follows (Von Sperling, 2007c, 2007b):



The nitrification rate is governed by numerous factors. These are:

(1) Organic matter loading rate. At a high C:N ratio, the growth of nitrifiers is inhibited due to insufficient oxygen supply caused by unexpected formations of heterotrophic microorganism layers covering the nitrifying biofilm (Nogueira et al., 2002). In fact, at the SALR value of 5 g BOD₇/m²d, nitrification hardly occurs (Hem et al., 1994). Therefore, the SALR value of < 5 g BOD₇/m²d is recommended for MBBR systems with downstream nitrification (Ødegaard, 2006).

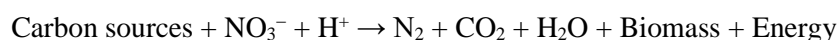
(2) Ammonium concentration. At low ammonium concentrations ($< 1 - 3 \text{ mg NH}_4\text{-N/l}$), the nitrification rate is limited. At concentrations of greater than $3 \text{ mg NH}_4\text{-N/l}$, the nitrification rate is governed by the DO and OLR (Ødegaard, 2006).

(3) Dissolved oxygen concentration. Nitrification rate and oxygen concentration reveal a linear relationship (Hem et al., 1994), indicating that a high efficiency of nitrification requires high oxygen concentration in the bulk liquid (Ødegaard, 2006). According to Ødegaard (2006), at an organic loading above approximately $4 \text{ g BOD}_7/\text{m}^2\text{d}$, the DO of $>6 \text{ mg O}_2/\text{l}$ is required for nitrification to occur.

(4) Temperature. Temperature disturbs the nitrification rate by different means: (a) affects intrinsic biological nitrification kinetics; (b) affects the diffusion rate of substrate into and out of the biomass; (c) affects the liquid viscosity that possibly influences the effect of shear energy on biofilm thickness; and (d) affects the solubility of oxygen in the liquid (WEF, 2011). Overall, despite a decreased activity of nitrifying microorganisms at colder temperatures, the nitrification rate in MBBR systems can be adequately maintained by the combined effect of higher attached biofilm concentrations and higher DO concentrations as a result of an increase in gas solubility (WEF, 2011; Safwat, 2019).

(5) pH/alkalinity. Low alkalinity levels will inhibit the nitrification rate, thus, maintaining a pH of at least 6.8 or a minimum alkalinity of 70 mg/L as CaCO_3 is recommended to prevent inhibited nitrification (Metcalf & Eddy Inc. et al., 2013).

With regards to the denitrification process in MBBR systems, nitrates are reduced to gaseous nitrogen by facultative heterotrophic microorganisms using organic carbon as the electron donor in anoxic milieu (Von Sperling, 2007a). The denitrification rate is influenced by the biodegradable organic matter concentration, the nitrate concentration, the wastewater temperature and the DO concentration in the bulk liquid (Ødegaard, 2006; WEF, 2011). The overall equation modified from Von Sperling (2007a) for the denitrification process is demonstrated as follows:



The MBBR systems have been used for denitrification come in pre-, post-, and combined configurations Table APX 1e, 1f and 1g (WEF, 2011). Pre-denitrification mode proposes a moderate nitrogen removal efficiency of between 50 and 70% (WEF, 2011). With the aim of further nitrate removal, this configuration acquires a nitrate recirculation, to which the recirculation ratio ($Q_{\text{recirculation}}:Q_{\text{inflow}}$) is recommended from 1:1 to 3:1 (WEF, 2011). A higher recirculation rate will lead to a decrease in denitrification efficiency as a result of elevated dissolved oxygen levels in the recirculation stream (WEF, 2011). Additionally, denitrification efficiency shall decrease in case of carbon depletion – a frequent event in wastewater treatment due to low carbon levels in the raw wastewater and/or extensive carbon removal by upstream processes. Consequently, heterotrophic microorganisms have insufficient substrate, which, in turn, results in a low denitrification rate (WEF, 2011). Meanwhile, the post-denitrification mode offers a high-level nitrogen removal of up to 80% (Ødegaard, 2006). Lower total bioreactor volumes (40–50%), better process control, and the maximum nitrate SARRs of over $2 \text{ g/m}^2\text{d}$ were reported for this configuration (Ødegaard, 2006). A major disadvantage of the post-denitrification

is the rise in operating costs. Due to the depletion of carbon by upstream processes, the addition of external carbon is required, thus leading to higher operating expenses.

Due to the limitations of the pre- and post-configurations, the combined configuration is referred to as the combination between economical pre-denitrification and high-performance post-denitrification (WEF, 2011). In the combined configuration, the MBBR reactors in series can operate in either aerobic or anoxic mode, thus offering operational flexibility to achieve treatment goals effectively and economically (WEF, 2011). A typical combined configuration can be found in Table APX 1g. As depicted in Table APX 1g, the first and fourth reactors operate anoxically with mixers and no aeration, while the second reactor operates in full aeration mode and the third reactor operates in either aerobic or anoxic mode. The first reactor is used for pre-denitrification, in which part of nitrate will be eliminated. After that, carbon degradation and nitrification processes occur in the second reactor to remove organic matter and ammonium from the wastewater stream. The third reactor is divided into two sections, one with diffusers running most length of the reactor and another small section without diffusers. The section without diffusers help lowers the DO level before a moderate flow is recirculated from there to the first reactor. The ratio of $Q_{\text{recirculation}}:Q_{\text{inflow}}$ is lower than that of pre-denitrification mode, ranging from 0.25:1 to 0.5:1 in order to prevent oxygen recirculation (WEF, 2011). The section covered with diffusers can operate with little or no aeration in case of low COD and ammonium levels or run at full aeration in events of high COD and ammonium levels. However, running at full aeration mode will then increase the demand for external carbon sources in the post-denitrification step. The fourth reactor is used for post-denitrification, in which the remaining nitrate is finally removed with the addition of external carbon sources. If stringent limits on effluent BOD/COD or nitrate concentrations are to be complied with, a small, aerated reactor can be installed for further removal of residual biodegradable matter (WEF, 2011).

2.1.3 Advantages and Disadvantages of the MBBR technology

The MBBR process offers many advantages: (1) MBBR systems eliminate the need for activated sludge recirculation, resulting in reduced footprint, minimal biomass loss, simplified operation and decreased operating costs. (2) a conventional activated sludge (CAS) process can simply be retrofitted to a MBBR process by adding carriers and installing a sieve system that prevents media loss at the reactor outlet. (3) promoting higher concentration of relevant organisms (e.g., nitrifying and denitrifying bacteria), thus enhancing the efficiency of $\text{NH}_4^+\text{-N}$ removal, (4) preventing sludge bulking issues in the secondary clarifier, (5) exhibiting improved resilience against organic shocks, and (6) ability to withstand peak wet weather flow variations (Metcalf & Eddy Inc. et al., 2013; Wei et al., 2016; Collivignarelli et al., 2019).

The disadvantages of the MBBR process include (1) poor aeration energy efficiency. The required oxygen concentration for the CAS process is 1-2 mgO_2/L while the MBBR process demands at least double or even quintuple that values, ranging from 4 to 10 mgO_2/L (Ødegaard, 2006; Metcalf & Eddy Inc. et al., 2013). (2) possibility of short-circuit flows due to the interaction of flow and media (Dias et al., 2018), (3) accumulation of lime in the reactors, (4) difficulties for diffuser maintenance, (5) limited capacity of phosphorus removal only by chemical addition (Metcalf & Eddy Inc. et al., 2013), (6) high operating costs and (7) high sludge production (Magdum & V, 2017).

2.2 Air flow rates and filling fractions in the MBBR process

2.2.1 Filling fractions

The efficiency of the MBBR process is conditioned by operational conditions such as Filling Fraction (FF), and Dissolved Oxygen (DO) (Santos et al., 2020). The filling fraction represents the bulk volume of the carriers that occupies in the mixture of carriers and water. The filling fraction can be calculated using the following formula:

$$FF = \frac{V_{bulk-carrier}}{V_{bulk-carrier} + V_{effective\ water}} \cdot 100 \quad (2-1)$$

where FF is the filling fraction [%]; $V_{carrier}$ is the bulk volume of the carriers [m³]; and $V_{effective\ water}$ is the effective water volume [m³];

The FF is an important operational parameter for MBBR systems as it reflects the amount of effective surface area for microbial growth, which in turn impacts the treatment efficiency of the system (Sonwani et al., 2022). The FF varies depending on the specific design and requirements of the MBBR process, but typically ranges from 50% to 70% (Leiknes et al., 2001). A high FF value is to decrease the mixing efficiency in the reactor (Ødegaard, 2006) and to inhibit biofilm development on the exterior surface of biofilm carriers as a result of constant collisions of carriers (Madan et al., 2022). Practical experience has shown that mixing is more effective at lower fill fractions (<55%) (WEF, 2011). The optimal FF value for nutrient removal was proposed to be from 30% to 40% while organic matter removal would demand a higher value of between 50% and 60% (Madan et al., 2022).

Vietnamese - German University

2.2.2 Air flow rates

It is of note that the airflow rate should not be confounded with the bubble rise velocity. The airflow rate refers to the volume of air passing through a specific point or device per unit of time, while the bubble rise velocity refers to the speed at which a bubble rises through a liquid medium. They are two different parameters used to describe different aspects of gas-liquid interactions.

The airflow rate can significantly impact the performance of the MBBR system by different means. To begin with, the airflow rate shall influence the growth of biofilm in the carrier media. A sufficient air flow rate is essential in providing enough oxygen for the growth and activity of microorganisms, thus yielding high treatment efficacy. On the other hand, high airflow rates can diminish biofilm thickness due to increased shear forces caused by the agitation of the media, while extremely high air flow rates may detach the biofilm from the media (Madan et al., 2022). Moreover, airflow rate shall influence aeration performance, including bubble size distributions, bubble shape, bubble rise velocity, surface renewal rates and system turbulence, etc. (Mueller et al., 2002). According to Mueller et al. (2002), the increase in total airflow rate will lead to the production of larger bubbles and higher bubble velocities, which subsequently decreases the gas-liquid interfacial surface area and oxygen transfer efficiency. Theories on bubble formation are to be discussed in Section 2.3 of this paper.

In process operating conditions, limited research has been conducted on determining the optimal airflow rate. McQuarrie and Boltz (2011) investigated the minimum airflow rate required to uniformly distribute

plastic biofilm carriers is in the range of 5 to 10 $\text{m}^3/\text{m}^2_{\text{basin floor}} \cdot \text{h}$, with a typical design value in the range of 6 to 8 $\text{m}^3/\text{m}^2_{\text{basin floor}} \cdot \text{h}$. Based on such values, the airflow rate is to be adjusted to meet the specific oxygen requirements of the process, whether it involves carbonaceous removal or combined carbonaceous removal with nitrification. The process airflow requirement is typically designed with 0.8-alpha (α) 0.95 beta (β) and 1.0 fouling (F) factors (McQuarrie & Boltz, 2011; Daigger & Boltz, 2018). During the design stage, the maximum and minimum airflow rates per orifice should not be neglected, about 1.75 m^3/h and 1.60 m^3/h , respectively, with a 50 percent turndown possible. Furthermore, the design air velocity in the manifold should be considered, which is around 13 m/s in 0.1 to 0.2 m diameter pipes and 20 m/s in pipes with a diameter larger than 0.2 m (Daigger & Boltz, 2018). Careful consideration of these factors contributes to the effective design and operation of the system.

In clean water tests, Pham et al. (2008) suggested that the minimum airflow rates required to establish a roll pattern in coarse-bubble diffusers at filling fractions of 25%, 50% and 65% are 5.69, 6.23, 7.32 m^3/h , respectively. Meanwhile, the minimum airflow to establish a roll pattern in fine-bubble diffusers in clean water test at filling fractions of 25%, 50% and 65% are 47.50, 54.44, 67.96 $\text{m}^3_{\text{air}}/(\text{m}^2_{\text{diffuser area}} \cdot \text{h})$, respectively. Sander et al. (2016) investigated the influence of airflow rates on oxygen transfer at different filling fractions. The airflow rate from Sander et al. (2016) was stated as the superficial gas velocity (SGV- [$\text{m}^3_{\text{air}}/(\text{m}^2_{\text{basin floor}} \cdot \text{h})$] or [m/h]). Three to four different SGVs were executed during their clean water tests with coarse- and fine-bubble aeration systems. The SGVs varied between 10 and 14 m/h for the former system and ranged between 7 and 9 m/h for the latter system. At such SGVs, the researchers observed a complete mixing of the carrier media at all investigated filling fractions. Dias et al. (2018) conducted a study to investigate the correlation between various SGVs with k_{LA} and SSOTE. This study suggested the dispersion number as a mixing indicator. A dispersion number ≤ 0.02 indicates a low degree of mixing, while a value ≥ 0.2 indicates a high degree of mixing (Tomlinson and Chambers (1979), cited as Dias et al., 2018). In their research, Dias et al. (2018) observed a moderate to high degree of mixing with different carriers at an airflow velocity of 2.2 $\text{m}^3_{\text{air}}/(\text{m}^2_{\text{basin floor}} \cdot \text{h})$.

The aforementioned research has suggested on the airflow rate for establishing a good mixing pattern. However, there is no consensus regarding a standardized unit for airflow rate measurement. Some studies solely consider the airflow rate while others may consider the airflow rate per diffuser area or per basin floor area. It is of note that a high airflow rate in a small reactor would be insignificant in a large reactor. Here, in this study, it is proposed to use the unit of air volume per unit of effective water volume per unit of time [$\text{m}^3_{\text{air}}/(\text{m}^3_{\text{water}} \cdot \text{h})$] to summarize the findings from previous research.

It is crucial to distinct the effective water volume (V_{eff}) and the total water volume within the reactor (V_{total}). The total water volume comprises three components: the volume of effective water, the volume occupied by the solid (plastic) fraction of the carriers, and the volume occupied by relevant submerged equipment:

$$V_{\text{total}} = V_{\text{eff}} + V_{\text{solid-carrier}} + V_{\text{submerged equipment}} \quad (2-2)$$

Assume the volume of the submerged equipment is not considerable, Eq. (2-2) becomes:

$$V_{eff.} = V_{total} - V_{solid-carrier} \quad (2-3)$$

The volume occupied by the solid (plastic) fraction of the carriers in the reactor can be determined by establishing the relationship between the number of carriers, their mass and their bulk volume, which will be demonstrated in detail in Section 7.2.2.

The summary of various airflow rates to establish mixing from different research can be found in Table 1. As shown in Table 1, the airflow rate of $1.15 \text{ m}^3_{\text{air}}/(\text{m}^3_{\text{water}}*\text{h})$ can ensure good mixing for the clean water tests in fine-bubble systems.

Table 1 Investigated airflow rate ranges by different research

No.	Research	Investigated airflow rates [Nm ³ _{air} /(m ³ _{water} *h)]		Effective water volume [m ³]	Investigated filling fractions [%]
		Coarse-bubble system	Fine-bubble system		
I. Clean water tests					
1	Pham et al. (2008)	1.93–5.01 (1.93–2.48) (*)	1.96–5.09 (1.99–2.85)	2.95	25–65
2	Sander et al., (2016)	0.56–3.25 (1.69–2.37)	0.56–1.84 (1.18–1.52)	8.5	0–50
3	Dias et al., (2018)	1.69–12.46 (1.69)	-	1.95	60
4	Collivignarelli et al., (2019)	1.15–2.88	1.15–2.88	52	40
5	Sun et al., (2015)	21.43	21.43	0.07	0-50
II. Process water tests					
1	Wei et al., (2016)	6.93	-	0.09	40-60
2	Barwal and Chaudhary (2015)	7.0–14.0	-	0.03	0-70

(*) Airflow rate range to exhibit a good mixing pattern

2.2.3 Classification of dynamic wet pressures with commonly used scales

Dynamic wet pressure (DWP), which is also referred to as diffuser headloss or pressure drop, is an important parameter in the evaluation and monitoring of fine bubble diffusers (Rosso & Shaw, 2015). It represents the pressure difference in the air pipe near the submerged diffuser and the hydrostatic pressure (Schwarz et al., 2021). In other words, high DWP results in higher energy consumption. It is measured in the laboratory or in the field and expressed in centimeters or inches of water at a specific airflow rate (Mueller et al., 2002). The drawing of a Standard DWP Measuring Setup is illustrated in Figure 3

It is of note that the DWP is not constant. The DWP increases with higher airflow rates, which, in turn, results in the generation of smaller bubbles. Although smaller bubbles may lead to higher oxygen transfer efficiencies, the extra power required to overcome the higher head loss may offset any potential savings (Mueller et al., 2002). Moreover, the DWP increases over time due to clogging of pores in ceramic and membrane diffusers, which leads to a decrease in overall process efficiency and power wastage. Table 2 provides reference values for DWP associated with certain diffuser types.

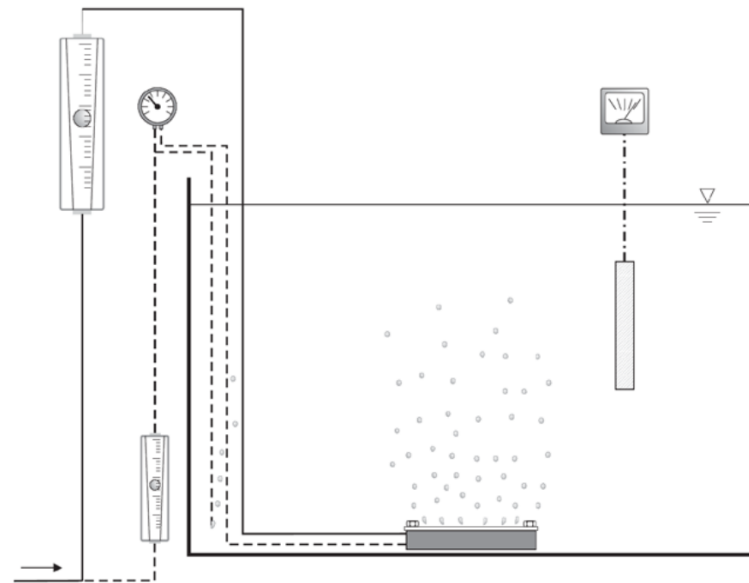


Figure 3. Drawing of a Standard DWP Measuring Setup. The DWP is measured with the differential manometer between the inside of the diffuser and the auxiliary line. Source: Rosso and Shaw (2015)

Table 2. DWP values for certain diffuser types. Adapted from Rosso and Shaw (2015)

Process Parameter	50 mm EPDM Tube	50 mm Silicone Tube	228 mm EPDM Disc	228 mm Ceramic Disc	76 mm EPDM Tube	76 mm PU Tube	1 m ² PU Panels
DWP_{initial} (meter of water)	0.48±0.05	0.68±0.08	0.97±0.13	0.20±0.02	0.56±0.08	0.48±0.02	0.99±0.08
Expected power increase	20%	25%	45%	35%	50%	70%	35%
Ratio of DWP_{initial}/ DWP_{after cleaning}	2.5	1.2	1	1.5	1.2	1	1.3

2.3 Mass transfer at the gas-liquid interface

Mass transfer refers to the movement of a substance from one place to another due to a driving force, either within a single phase or between two phases (Mueller et al., 2002). One of the most common examples of mass transfer in wastewater treatment is the transfer of oxygen molecules between a gas and a liquid. This process occurs in three stages, beginning with the transfer of oxygen molecules from the gas phase to the surface of a liquid. Once at the surface, an equilibrium is established between the gas and liquid phases, and finally, the oxygen molecules diffuse into the bulk of the liquid. (Mueller et al., 2002).

Gaining insights on oxygen mass transfer rate is key to sustaining aerobic biological processes from both operational and economic perspectives (Amaral et al., 2019). The two-film theory is the most commonly used theory for describing the gas-liquid mass transfer rate (Amaral et al., 2019). According to this theory, the gas-liquid interface provides resistance to the transfer of gas molecules from the bulk of the gas phase to the liquid phase (Mueller et al., 2002; Collivignarelli et al., 2019). The oxygen flux

through each film as the product of the driving force by the mass transfer coefficient is determined by using Eq. (2-4) (Garcia-Ochoa & Gomez, 2009).

$$J^0 = k_G \times (p_G - p_i) = k_L \times (C_i - C_L) \quad (2-4)$$

where J^0 is the molar flux of oxygen through the gas–liquid interface [$\text{mol} \cdot \text{m}^{-2} \cdot \text{s}^{-1}$]; k_G [$\text{mol} \cdot \text{m}^{-2} \cdot \text{s}^{-1} \cdot \text{Pa}$] and k_L [$\text{m} \cdot \text{s}^{-1}$] are the local mass transfer coefficients; p_G is the oxygen partial pressure in the gas bubble [Pa]; and C_L is the dissolved oxygen concentration in the bulk liquid [$\text{mol} \cdot \text{L}^{-1}$]; index i refers to values at the gas–liquid interface.

Given that the interfacial concentrations are difficult to measure, the oxygen flux through each film can be rewritten by considering the overall mass transfer coefficients (Garcia-Ochoa & Gomez, 2009):

$$J^0 = K_G \times (p_G - p^*) = K_L \times (C^* - C_L) \quad (2-5)$$

where p^* is the oxygen pressure in equilibrium with liquid phase; C^* is the oxygen saturation concentration in the bulk liquid in equilibrium with the bulk gas phase; and K_G and K_L are the overall mass transfer coefficients.

According to Henry's law, the relationship between the oxygen partial pressure and the oxygen saturation concentration in equilibrium is expressed by the following equation:

$$p_G = H \times C^* \quad (2-6)$$

where p_G is the oxygen partial pressure in the gas bubble; C^* is the oxygen saturation concentration in the bulk liquid in equilibrium to the bulk gas phase; and H is Henry's constant.

Combining Eqs. (2-4), (2-5) and (2-6), the following relationship is obtained:

$$\frac{1}{K_L} = \frac{1}{H \times k_G} + \frac{1}{k_L} \quad (2-7)$$

The two-film theory and the relationship between the concentrations and mass transfer coefficients at gas–liquid interface can be found in Figure 4.

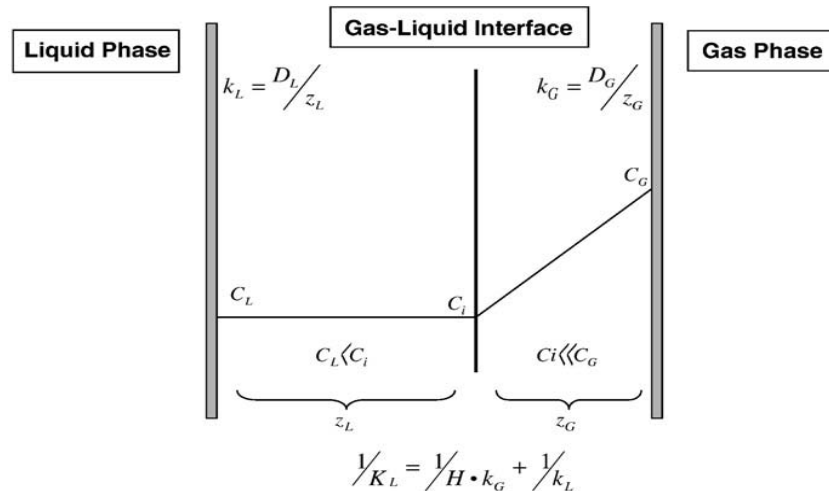


Figure 4. Schematic representation of the gas–liquid interface according to two-film theory. Source: Garcia-Ochoa and Gomez (2009)

Due to the low solubility of oxygen in water that results in a very high H value, the gas phase resistance can be neglected, thus, the overall mass transfer coefficient is considered to be equal to the local mass transfer coefficient $K_L=k_L$. Hence, the oxygen mass transfer rate per unit of reactor volume N_{O_2} is calculated by multiplying the molar flux of oxygen through the gas–liquid interface J^0 with the gas–liquid interfacial area per unit of liquid volume a (Garcia-Ochoa & Gomez, 2009).

$$N_{O_2} = a \times J^0 = k_L a (C^* - C_L) \quad (2-8)$$

The gas-liquid interfacial area per unit of liquid volume (a) refers to the area at which gas molecules can interact with liquid molecules, expressed in the unit of square meters per cubic meter (m^2/m^3). Smaller bubbles offer two advantages over larger bubbles in terms of oxygen transport. Firstly, they provide a larger gas-liquid interface per unit of liquid volume (a), as illustrated in Figure 5. This increased interface allows for enhanced interaction and exchange between the gas and liquid phases. Secondly, smaller bubbles have a longer residence time in the medium, allowing for a greater transfer of oxygen into the liquid (higher k_L) (Rosso, 2018). However, smaller bubbles also pose a negative effect on oxygen mass transfer. When bubbles become sufficiently small, they exhibit like rigid spheres with limited internal recirculation, thus preventing oxygen gas molecules from reaching the surface and subsequently contributing to a reduced amount of oxygen transferred to the liquid phase (Vanags & Suleiko, 2022). Literature suggests that the ideal bubble size falls within the range of 2–3mm (Rao, 2010), and this value should be carefully considered when choosing an appropriate diffuser.

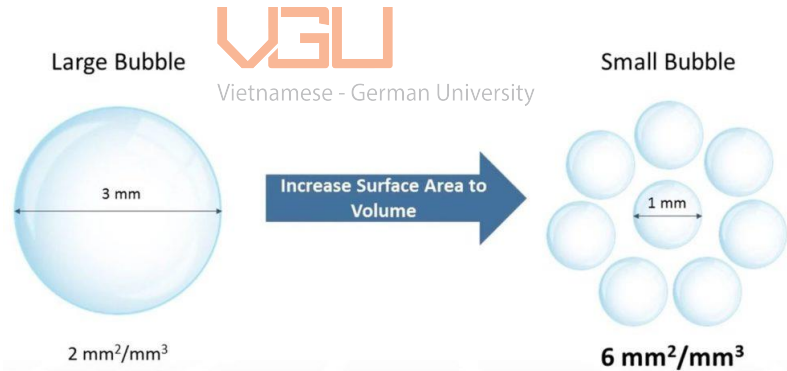


Figure 5 Comparison of the gas-liquid interface areas of large and small bubbles. Source: Düppe (2020)

Measuring k_L and a separately is challenging, therefore, $k_L a$ is measured as a combined value and is known as the volumetric mass transfer coefficient. The $k_L a$ is a key parameter that characterizes to which extent oxygen is efficiently transported and dispersed from the gas phase to the liquid phase. This is crucial in establishing oxygen transfer rate and transfer efficiency and quantifying effects of the operating variables on the provision of dissolved oxygen (Garcia-Ochoa & Gomez, 2009; Rosso, 2018). Moreover, the volumetric mass transfer coefficient is the key value for the scale-up of bioreactors. Scale-up involves the design and construction of larger scale systems based on experiments conducted on smaller-scale equipment. Typically, this process ranges from small-scale equipment of 1 to 25 L to larger-scale systems of 30 to 1000 m³. The scale-up process is divided into three main scales: (i) laboratory scale for preliminary studies, (ii) pilot scale for bioprocess optimization, and (iii) production

scale for economic implementation (Ju & Chase, 1992). Several criteria such as power input per unit volume (P/V), volumetric mass transfer coefficient (k_La), impeller tip speed of the agitator or shear, and dissolved oxygen concentration (C_{O_2}) are used to determine the scale-up of a bioprocess. Among these criteria, the volumetric mass transfer coefficient plays a vital role in the scale-up of aerobic fermentation. By focusing on the constant value of the volumetric mass transfer coefficient, the successful scale-up of bioreactors can be achieved, enabling optimal performance and economic viability of larger scales (Garcia-Ochoa & Gomez, 2009).

Various methods are available for measuring k_La in both clean water and process water. Basically, these methods can be divided into chemical and physical methods. Chemical methods were the first to be widely used that involve the addition of chemicals, such as sulfite, cobalt or nitrogen in order to deoxygenate water before being re-aerated until saturation (Collivignarelli et al., 2019; ASCE, 2022). However, these methods are not recommended for sparged bioreactors due to the changes in physicochemical properties of liquids (Garcia-Ochoa & Gomez, 2009). The absorption rate, for example, can be boosted by fast chemical reactions in the liquid phase once adding chemicals, thus leading to higher k_La than the actual values. Meanwhile, physical methods are currently of widespread use due to advantages of not introducing residual dissolved solids to the test water, providing more accurate k_La , and not requiring the tank to be refreshed and equilibrated with clean water after a series of tests (Garcia-Ochoa & Gomez, 2009; ASCE, 2022).

Physical methods involve the direct measurement of gas concentration in the liquid phase that employs oxygen probes to measure concentration changes in the dispersed gas in the medium under non-stationary conditions. One physical method that has been recognized as an alternative to sulfite deoxygenation is High Purity Oxygen Desorption (HPOD) (ASCE, 2022). According to Wagner et al. (1998), the method involves the raise of the DO level to an oxygen-supersaturated level by injecting pure oxygen. Once the supersaturated level is reached, the oxygen feed is shut off and the subsequent decrease in DO concentration is analyzed until the tank DO level reaches its air saturation value. The steps to execute the HPOD method will be discussed in detail in Section 3 of this paper.

In the HPOD method, the change of oxygen concentration with respect to time is described by Eq. (2-8) (Garcia-Ochoa & Gomez, 2009; Vanags & Suleiko, 2022).

$$\frac{dC}{dt} = OTR - OUR \quad (2-9)$$

where dC/dt is the accumulation oxygen rate in the liquid phase; OTR is the oxygen transfer rate from the gas to the liquid; and OUR is the oxygen uptake rate by the microorganisms.

In clean water tests, due to an absence of microorganisms ($OUR = 0$), Eq. (2-9) can be rewritten:

$$\frac{dC}{dt} = k_La (C^* - C_L) \quad (2-10)$$

Integration of Eq. (2-10) with two different times t and t_0 yields:

$$\ln\left(\frac{C^* - C_t}{C^* - C_0}\right) = -k_L a (t - t_0) \quad (2-11)$$

where t_0 is the time when the desorption process begins [h]; C_t and C_0 are the DO concentrations in the bulk liquid at time t and t_0 , respectively [mg L^{-1}]; C^* is the DO saturation concentration [mg L^{-1}]; and $k_L a$ is the volumetric mass transfer coefficient [h^{-1}].

Figure 6 illustrates the decrease of the DO concentration with respect to time. As shown in Figure 6, t_0 is also the time when the DO supersaturation concentration C_{en}^* is reached. Thus $t_0 = 0$ and $C_0 = C_{en}^*$, Eq. (2-11) can then be expressed as:

$$\ln\left(\frac{C^* - C_t}{C^* - C_{en}^*}\right) = -k_L a \cdot t \quad (2-12)$$

or

$$C_t = C^* - (C^* - C_{en}^*) \cdot e^{-k_L a \cdot t} \quad (2-13)$$

According to Eq. (2-12), a linear relationship can be established by plotting $\ln\left(\frac{C^* - C_t}{C^* - C_{en}^*}\right)$ with respect to experiment time. The slope of this plot against time, as depicted in Figure 7, can be used to determine the volumetric mass transfer coefficient $k_L a$.

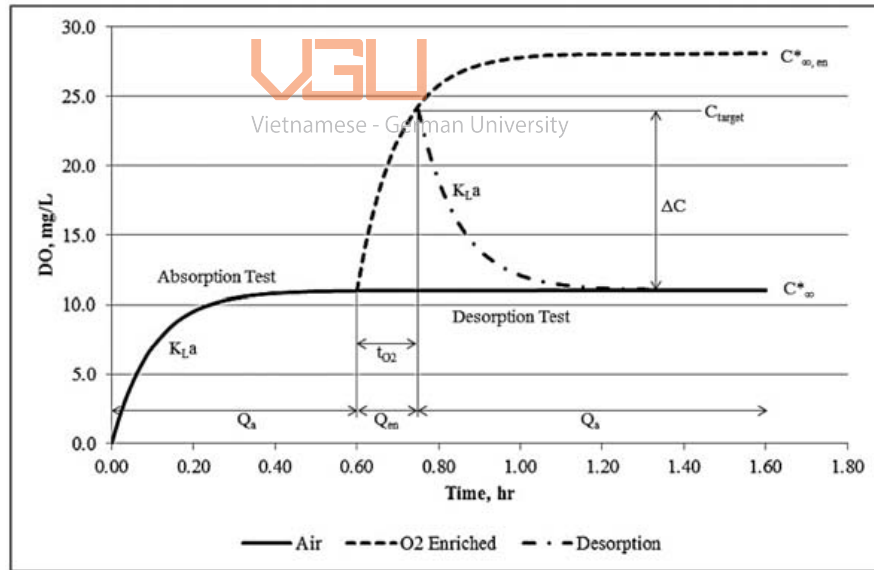


Figure 6. Typical changes of oxygen concentration with respect to time for the HPOD method. Source: (ASCE, 2022)

Within this study, physical methods are selected to assess the oxygen transfer coefficient, which will be discussed in detail in Section 3.2.

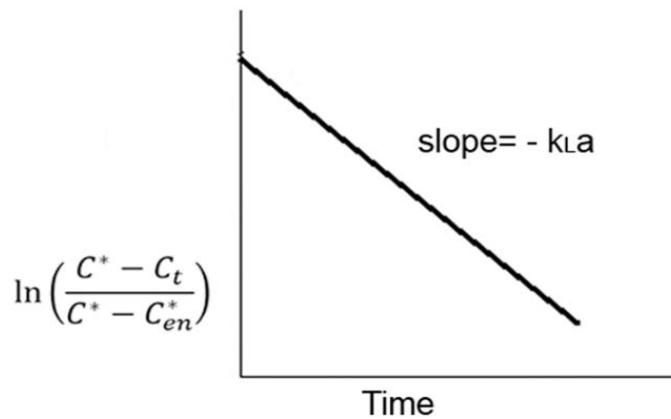


Figure 7. Graph of natural logarithm of various DO concentrations versus experiment time to determine k_La . Modified according to Vanags and Suleiko (2022)

2.4 Bubble formation and rise

The primary objective of aeration is to introduce oxygen into a MBBR system to facilitate the growth of aerobic microorganisms that degrade organic matter. This is achieved by the continuous injection of compressed air or oxygen enriched air through a piping system to submerged diffusers at the floor of the reactor. As a result of that, bubbles rise through the bulk liquid and transfer oxygen into it (Mueller et al., 2002; Rosso, 2018). Apart from that objective, bubbles also induce liquid movement that contributes to mixing. It is claimed that only 20% of the energy invested in aeration is for oxygen supply while the remaining 80% contributes to mixing (Rosso, 2018). This stems from the fact that four-fifths of the air is nitrogen. Therefore, bubble formation is a crucial aspect that affects the performance of an aeration system in terms of oxygen transfer efficiency, mixing performance, as well as energy consumption (Rosso, 2018).

Some dispute exists in the literature regarding bubble size classification. Coarse bubbles are considered to those with a diameter of ≤ 50 mm (Sander et al., 2016; Rosso, 2018), while fine bubbles are less than 5 mm (Rosso, 2018) or 2–5mm (Sander et al., 2016). In some cases, medium bubbles are also sometimes referred to as having a size distribution between 5 and 50 mm in diameter, (Rosso et al., 2011). In this paper, bubble size is conventionally classified into coarse bubbles and fine bubbles, with diameters in the range of 5–20mm and of <5 mm, respectively. Bubble size depends on several factors such as flow rate, inlet pressure, contact angle with the rubber membrane, wastewater characteristics and submergence (Rosso, 2018). Out of these factors, the flow rate has the most significant impact on the bubble size, followed by membrane material and contact angle (Rosso, 2018).

2.4.1 Coarse-bubble systems

Coarse-bubble systems employ larger openings or orifices (approximately 5mm in diameter) to introduce larger bubbles, sizing from 20 mm and can reach 50 mm (Henkel, 2010; Rosso, 2018, p. 43). These systems are characterized by a relatively low number of openings (around 100 orifices/ $m^2_{diffuser}$) and a high specific air flow rate (roughly 100 cm^3 air/(orifice·s)) (Henkel, 2010). Coarse-bubble systems can be installed in different configurations, including full-floor, single row on the sides of plug flow tanks (spiral roll), or two or more rows (cross roll, ridge and furrow). However, the full-floor

configuration is commonly used to facilitate even air distribution throughout the tank, which is essential for effective treatment (Rosso, 2018). The bubbles produced by coarse-bubble systems are not spherical but shaped like spherical caps, similar to the shape of jellyfish (Figure 8). These bubbles are turbulent in nature, therefore, coarse-bubble aeration systems are currently of widespread use in MBBR systems that require a stronger grade of turbulence to maintain the carriers suspended (Sander et al., 2016). Furthermore, due to their high rate of surface renewal, coarse bubbles have a less severe surfactant interfacial accumulation, thus they have a higher α factor (ratio of process water to clean water mass transfer coefficients) when compared to fine-bubble systems (Rosso & Stenstrom, 2006).

Currently, various types of diffusers are employed for wastewater treatment. These diffusers can be classified into porous diffusers, non-porous diffusers, and other diffuser devices such as jet diffusers, perforate hoses, and U-tube diffusers (Mueller et al., 2002). In the case of MBBR aeration systems, non-porous diffusers generating coarse bubbles are of the most widespread use. As depicted in Section 2.1.1 and illustrated in Figure 2, coarse bubbles are typically produced through small orifices drilled into pipes positioned at the bottom of the biological basins. The perforated pipe distributors (diffusers) are made of stainless-steel and typically possess a diameter of 25 mm. Along the diffusers, orifices are drilled with diameters ranging from 1 to 4 mm and spaced at intervals of 38 to 102 mm (Moga et al., 2018).

Coarse-bubble diffusers bring several advantages over surface aerators or fine-bubble diffusers. To begin with, they require fewer diffusers, which results in reduced capital costs. Secondly, coarse-bubble diffusers are less subject to fouling or scaling due to the large dimension and high turbulence of the discharge orifices. Thirdly, coarse-bubble systems offer significantly higher OTR than fine-pore or surface aerators due to their capacity of accommodating high airflow rates. The maximum OTR of coarse-bubble diffusers is only limited by blower capacity and not the tank bottom surface area as in the case of fine-pore diffusers. Therefore, coarse-bubble systems are normally selected for high-strength industrial wastewater treatment that requires high OTR (Rosso, 2018).

Nevertheless, coarse-bubble systems have a major drawback: they offer poor energy efficiency. As a rule of thumb, SAE and OTR are inversely proportional. The characteristic of accommodating high airflow rates means that bubbles move upward rapidly within the coarse-bubble systems. This, combined with a relatively low surface-to-volume ratio lead to a low SAE, ranging between 0.6-1.5 kg O₂ kWh⁻¹ (Rosso, 2018). This is an important consideration for wastewater treatment plants that aim to optimize their energy usage and reduce operating costs. In fact, many municipal wastewater treatment plants replaced their coarse-bubble systems due to the rapid rise in energy prices in the early 1970s (Rosso, 2018). Coarse-bubble systems may have several advantages; however, their poor energy efficiency should be considered when deciding whether to use them for the WWTPs.

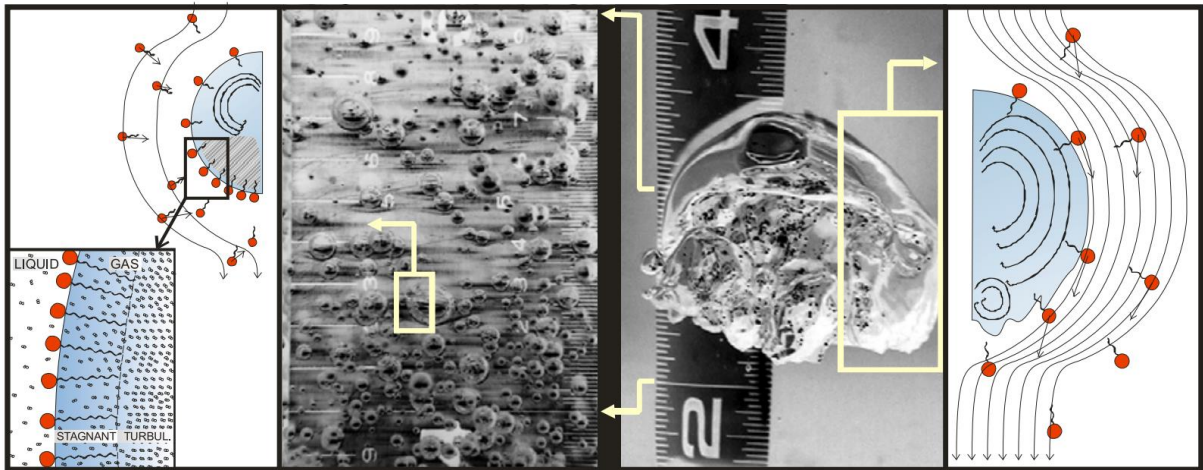


Figure 8. Comparison of fine (left photograph) and coarse (right photograph) bubbles generated by two different aerators operating at the same airflow rate in the same surfactant solution. The measuring scale is in inches (1 inch = 25.4 mm), and each scale sub-division is 1/10 in (= 2.54 mm). Source: Rosso (2018)

2.4.2 Fine-bubble systems

Fine bubbles can be generated by various technologies, either by releasing air through porous diffusers or punched membranes with small orifices (Suriasni et al., 2023), or by mechanically shearing large bubbles into small ones (Rosso, 2018). The small size of these fine bubbles, typically under 5 mm, is achieved through the presence of a large number of small orifices (around 0.2 mm in diameter) per unit of surface area, with densities of up to 100,000 orifices per square meter of diffuser. Additionally, maintaining a low specific air flow rate, generally $< 0.15 \text{ cm}^3$ air per orifice per second, contributes to the formation of fine bubbles (Henkel, 2010; Rosso, 2018).

In wastewater treatment, the use of porous diffusers with small orifices is the prevalent technology in the United States and Europe, particularly in the form of full-floor configurations (Rosso, 2018). This technology offers advantages such as lower airflow rates, reduced heat losses, limited stripping of volatile organic compounds, and a high SAE of up to $3.6\text{--}4.8 \text{ kg O}_2 \text{ kWh}^{-1}$. On the other hand, the mechanical shearing method utilizes energy from submerged turbines or jet diffusers to break large bubbles into fine ones without relying on small orifices. However, this approach has limitations, including uneven DO distribution and lower SAE than fine bubbles from fine-pore diffusers (in the range of $1.2\text{--}1.8 \text{ kg O}_2 \text{ kWh}^{-1}$) (Rosso, 2018). These considerations are crucial when selecting a technology for generating fine bubbles in various applications.

There are two major disadvantages for fine-pore diffusers. The first disadvantage is the risk of frequent fouling or scaling. Inorganic scaling and material degradation (i.e., aging) are inevitable over time, which in turn increases back pressure (often called dynamic wet pressure or headloss). This results in a decrease in overall oxygen transfer efficiency and an increase in power wastage. Therefore, fine-pore diffusers require routine cleaning, which can be done by various methods. Tank top hosing is the simplest method that uses plant effluent to wash the diffusers from the tank top while the aeration tank is empty. This technique can remove partially or completely biological slime accumulation (Rosso, 2018). Acid cleaning is another method to eliminate scaling by inorganic precipitates (silica, calcium

carbonate, gypsum, etc.). Due to the incompatibility between polymeric membranes and strong inorganic acids, this technique is limited to ceramic diffusers. Manual washing with low-strength hydrochloric acid (10 to 15% w/w) and injecting hydrochloric acid gas or acetic acid into air distribution lines are notable examples of the acid gas cleaning technique. (Rosso, 2018). For membrane diffusers, pneumatic cleaning techniques like flexing or reverse flexing are applied. Flexing involves the increase of airflow to an excess level for a short period of time (Rosso, 2018), while reverse flexing involves the interruption of air feed and release of pressure from the air feeding line through a constructed vent channel, causing the rapid collapse of the membrane onto the diffuser frame under the action of hydrostatic pressure (Odize et al., 2017).

The second disadvantage for both porous diffusers and turbines/jet diffusers is their lower α factor compared to coarse-bubble diffusers or surface aerators. According to Rosso (2018), a lower α factor corresponds to a decrease in mean cell retention time (MCRT) and OTR. It is believed that the lower α factor in fine-pore diffusers derives from many factors. Fouling or scaling can lead to a decrease in the α factor over time in operation, however, the effect of surfactants is considered to be the most influential factor (Rosso, 2018). Fine bubbles have lower interfacial velocity, resulting in a longer retention time of bubbles in the reactor. Since surfactant molecules have a longer time available for surface migration, the accumulation of surfactant at the fine-bubble interface occurs to a larger extent than for coarse bubbles. Once the surfactants have attached to the surface, their hydrophobic tails inside the bubble and turn bubbles into solid spheres, as depicted in Figure 8 (Rosso, 2018). Consequently, the internal gas circulation and interfacial renewal rates are severely reduced, which, in turn, causes gas transfer depression (Rosso & Stenstrom, 2006).



2.4.3 Bubble formation and rise

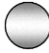


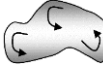

Previous investigations on coarse- and fine-diffuser systems have proven that the bubble formation process and the bubble rise behavior at the orifice are governed by the design and operating conditions of these diffuser systems. Nevertheless, there remains a significant knowledge gap in understanding the dynamics associated with bubble formation and rise phenomena. Thus, a further investigation into this field is essential for comprehending key features, mechanisms, and influential factors governing bubble formation, shape, rise velocity, and behavior. Since single bubbles and bubble swarms exhibit distinct dynamics and properties, these phenomena shall be assessed separately.

a. Single bubble behavior

Single bubble refers to the assessment of an isolated gas bubble within a liquid medium, focusing on its dynamic behaviors such as bubble shape, bubble wake, bubble size, and rise velocity (Yang et al., 2007). The assessment of bubble behavior at a single orifice consists of two stages: (1) the expansion of a gas bubble while still connected to the orifice and (2) the subsequent free rising before the bubble starts oscillating (Martín et al., 2006). The bubble expansion can be estimated using the Rayleigh-Plesset equation, which considers inertial, capillary, and viscous terms (Henkel, 2010). The rising of the bubble while still attached to the orifice is determined by the balance of various forces acting on the bubble (Yang et al., 2007), which is demonstrated in detail in Section 7.1.2. The rise characteristics of a single

bubble can be described in terms of its shape, rise velocity and motion (Yang et al., 2007; Henkel, 2010). The bubble shape and rise velocity can be graphically deduced from the Grace diagram (see APX 7.1.1). Further research by Henkel (2010) has expanded on the shape classification and identified additional subgroups. These are (1) spherical bubbles with rigid interfaces, (2) spherical bubbles with mobile interfaces, (3) ellipsoidal bubbles, (4) irregular bubbles, and (5) shield bubbles. Each subgroup is associated with specific bubble shapes and corresponding diameters, which are summarized in Table 3.

Table 3. Characteristic bubble shapes, depending on the bubble diameters. Source: Henkel (2010)

	Bubble shape	Reynolds number	Bubble size (mm)
1	Spherical bubble with rigid interface 	$Re_B < 1.4$	$d_B < 0.1$
2	Spherical bubble with mobile interface 	$1.4 < Re_B < 600$	$0.1 < d_B < 1.5$
3	Ellipsoid bubble 	$600 < Re_B < 1600$	$1.5 < d_B < 8.0$
4	Irregular bubble 	$1600 < Re_B < 4700$	$8.0 < d_B < 17$
5	Shield bubble 	$Re_B > 4700$	$d_B > 17$

At small bubble sizes ($d_B < 0.1$), surface tension forces (F_σ) dominate, and the bubble maintains a spherical shape with a rigid interface while rising in a linear trajectory. The bubble wake exhibits laminar flow behavior. For intermediate-sized bubbles ($0.1 < d_B < 8$ mm), both surface tension (F_σ) and drag forces influence (F_D) the shape and motion of the bubble. The bubble changes from spherical to ellipsoid with a mobile interface and follows a zig-zag motion. The wake flow transitions from laminar to turbulent behavior. It is worth noting that changes in surface tension and viscosity have a significant effect on the bubble's rise behavior in this range. These characteristics are commonly observed in fine bubble aeration systems used to meet the biological oxygen demand in wastewater plants. For large bubbles ($d_B > 8$ mm), liquid inertia forces (F_{IL}) start to dominate while the effects of surface tension and drag forces diminish with increasing bubble size (Yang et al., 2007). The rising of large bubbles returns to a linear trajectory, and the bubble wake flow remains turbulent. Changes in surface tension, liquid density, and viscosity have minimal impact on the rise behavior of these bubbles. These characteristics are commonly observed in coarse bubble aeration systems, which are specifically designed to facilitate crossflow aeration in membrane bioreactors.

b. Bubble swarm:

Bubble swarm phenomena refers to a group of bubbles existing within a specific region or volume of liquid as a result of a simultaneous release of bubbles through air diffusers (Henkel, 2010). Compared to a single bubble, bubbles within a swarm exhibit distinct behaviors. They interact with other bubbles, leading to various collective phenomena such as bubble coalescence (merging of bubbles) or bubble breakup (splitting of bubbles). These interactions not only change the overall properties of the swarm but also the individual bubbles within it (Henkel, 2010). The breakup and coalescence of bubbles play

a crucial role in the dynamics of two-phase flows, impacting overall fluid motions and the transfer of heat and mass through changes in the volume fraction and size distribution of the bubbles (Clift et al. (1978), cited as Zhang & Thoroddsen, 2008).

Nevertheless, the modeling of bubble coalescence and breakup still faces challenges due to limitations in existing models, including (a) the assumption that bubbles are part of the liquid phase, (b) no change in bubble size during their rise, and (c) the absence of bubble interaction between others (Rosso, 2018). The complexity of modeling bubble coalescence and breakup phenomena also varies depending on the specific gas-liquid flow pattern (Chen et al., 2021). Chen et al. (2021) addressed this complexity by employing the Interfacial Area Transport Equation to simulate these phenomena in different flow patterns, considering two groups of bubbles: spherical/distorted and cap/slug bubbles. The flow patterns are commonly observed in vertical flow channels, including bubble, slug, churn, and annular flows, characterized by increasing airflow rates in order. Figure 9 provides a visual representation of these flow patterns. As shown in Figure 9, spherical/distorted bubbles are attributed to the bubble flow pattern while the cap/slug bubbles are associated with slug, churn, and annular flow patterns.

In the context of bubble coalescence, this process involves the merging of two individual bubbles after a collision. This process can be divided into three distinct stages: (1) the initial contact between the bubbles controlled by the hydrodynamics of the liquid, resulting in the formation of a thin film separating the two bubbles; (2) the drainage of the liquid film under external forces (e.g. gravity, inertia, and flow) and surface forces of molecular origin; (3) the film ruptures at a critical thickness due to attractive surface forces and mechanical disturbances, ultimately leading to bubble coalescence (Nguyen et al., 2012; Chen et al., 2021). The key factor determining whether coalescence occurs is the rate of drainage and thinning of the liquid film during the second stage. If the time required for drainage and rupture is longer than the duration of the initial contact between the bubbles, bubble separation will occur instead of coalescence (Chen et al., 2021). Moreover, other factors such as bubble size, velocity, and collision frequency govern the occurrence of bubble coalescence. Bubble coalescence is formed by two mechanisms: random collision (RC) or wake entrainment (WE) (Chen et al., 2021).

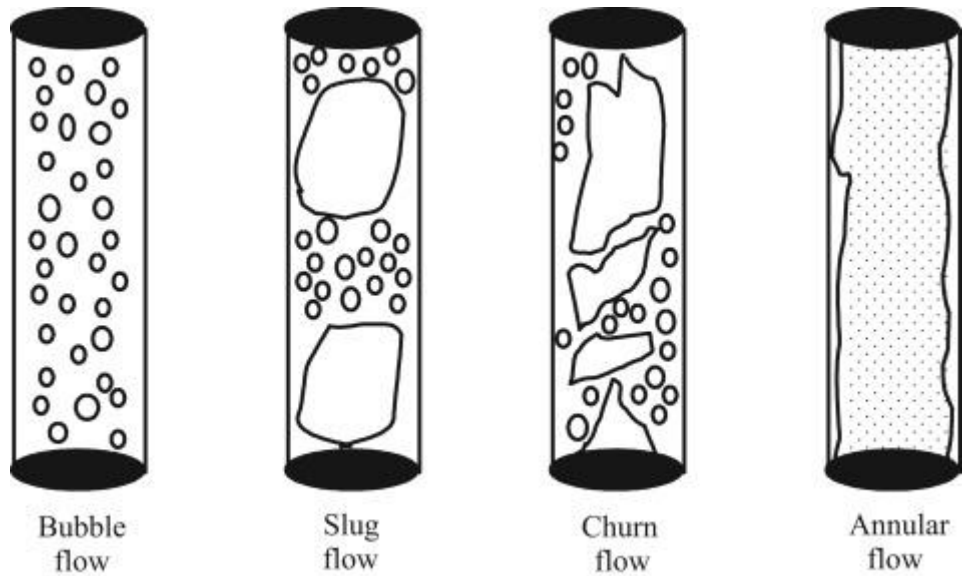


Figure 9. Flow regimes for vertical channels, two-phase flow. Source: Fanchi (2018)

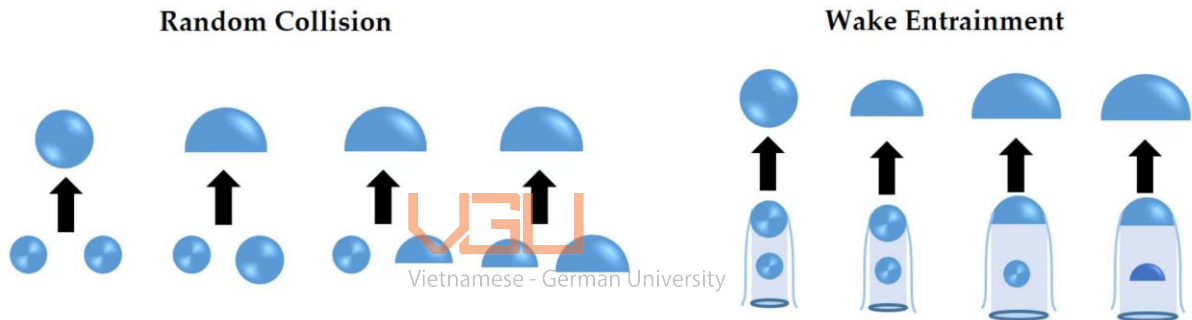


Figure 10. Schematic diagram of bubble coalescence mechanisms. Source: Chen et al. (2021)

Bubble breakup refers to a bubble disintegrating into two or more new bubbles. As a result of this, the gas-liquid interfacial area (a) as well as the volumetric mass transfer coefficient ($k_L a$) increase. According to Chen et al. (2021), there are three distinct mechanisms involved in bubble breakup:

(1) *Breakup due to turbulent impact.* This mechanism occurs when bubbles experience pressure fluctuations on their surface or collide with turbulent eddies or the surrounding fluid. As the amplitude of oscillation reaches a critical point, the bubble surface becomes destabilized, causing it to deform and stretch in a specific direction. Subsequently, the neck connecting it to the main body contracts and eventually causing the bubble to split into multiple smaller bubbles.

(2) *Breakup due to shearing-off.* As the size of the bubble increases, the mechanisms responsible for bubble breakup become more complex. In the shear-off mechanism, the instability of the bubble skirt occurs when the relative velocity is high enough to detach the skirt from the main bubble, resulting in the generation of smaller bubbles at the edge. The shearing-off process is influenced by factors such as gas distribution within the cap bubble or the viscous shear force. In the air-water flow, the interfacial viscous shear force can be neglected due to the low viscosity of water, thus the shearing-off process is mainly caused by the gas distribution inside the cap bubble.

(3) *Breakup due to surface instability*. This mechanism involves the formation of smaller bubbles from cap bubbles with unstable surface properties. The instability can be caused by various factors, including irregularities along the gas-liquid interface, density differences between two fluids, or shear forces at the interface between the gas and liquid phases.

The bubble breakup mechanisms are described in Figure 11.

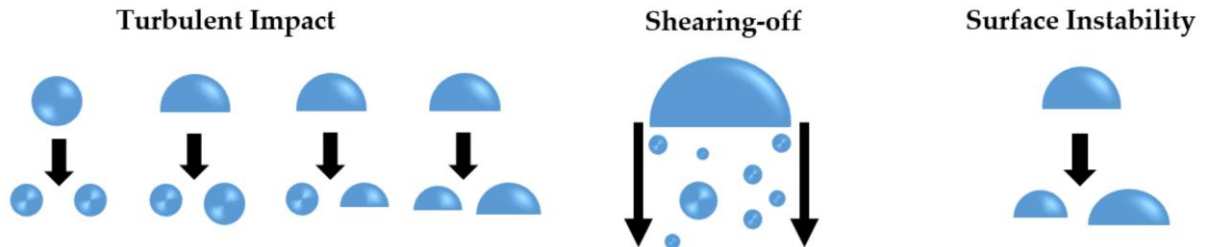


Figure 11. Schematic diagram of bubble breakup mechanisms. Source: Chen et al. (2021)

In contrast to a single bubble, a bubble swarm induces a liquid velocity field that influences the bubble rise velocity. In other words, the rise velocity of bubbles within a swarm will be not constant for a specific bubble diameter, as observed in the case of single bubbles. The rise velocity of the bubble swarm depends on the gas holdup, which represents the volume fraction of gas in the total volume of gas-liquid phase in the bubble column (Tao et al., 2019). Gas holdup is one of the most important parameters to characterize the hydrodynamic characteristics and mass transfer in submerged aeration systems (Tao et al., 2019). Specifically, in a two-phase system, gas holdup gives the volume fraction of the phases present in the reactor, allowing for the determination of residence time. Furthermore, gas holdup, in conjunction with the mean bubble diameter, governs the interfacial area. Submerged aeration systems employed in wastewater engineering typically operate within a gas holdup range of 0.002 to 0.08 (Thiersch (2001), cited as Henkel, 2010).

Figure 12 illustrates the relationship between the relative bubble rise velocity and the gas holdup in a fine bubble aeration system, specifically considering bubble diameters ranging from 2 to 4 mm. As depicted in Figure 12, the bubble swarm velocity can be categorized into three segments:

- a) At gas holdups below 0.005, the bubbles rise in a helical trajectory with minimal interactions. This behavior gives rise to isolated bubble clusters, in which one bubble enters the wake region of another, consequently yielding an increased bubble rise velocity.
- b) In the gas holdup range of 0.005 to 0.048 (as denoted by the dashed frame), which is typically observed in fine bubble aeration systems used for meeting biological oxygen demand, the turbulence in the bubble wake increases and radial movement is reduced. This leads to higher bubble rise velocities compared to single bubbles.
- c) With gas holdups higher than 0.05, which are typically achieved in intensive coarse bubble aeration systems, high turbulence is observed. Here, drag forces become dominant in determining the bubble rise behavior, resulting in a decrease in the bubble rise velocity.

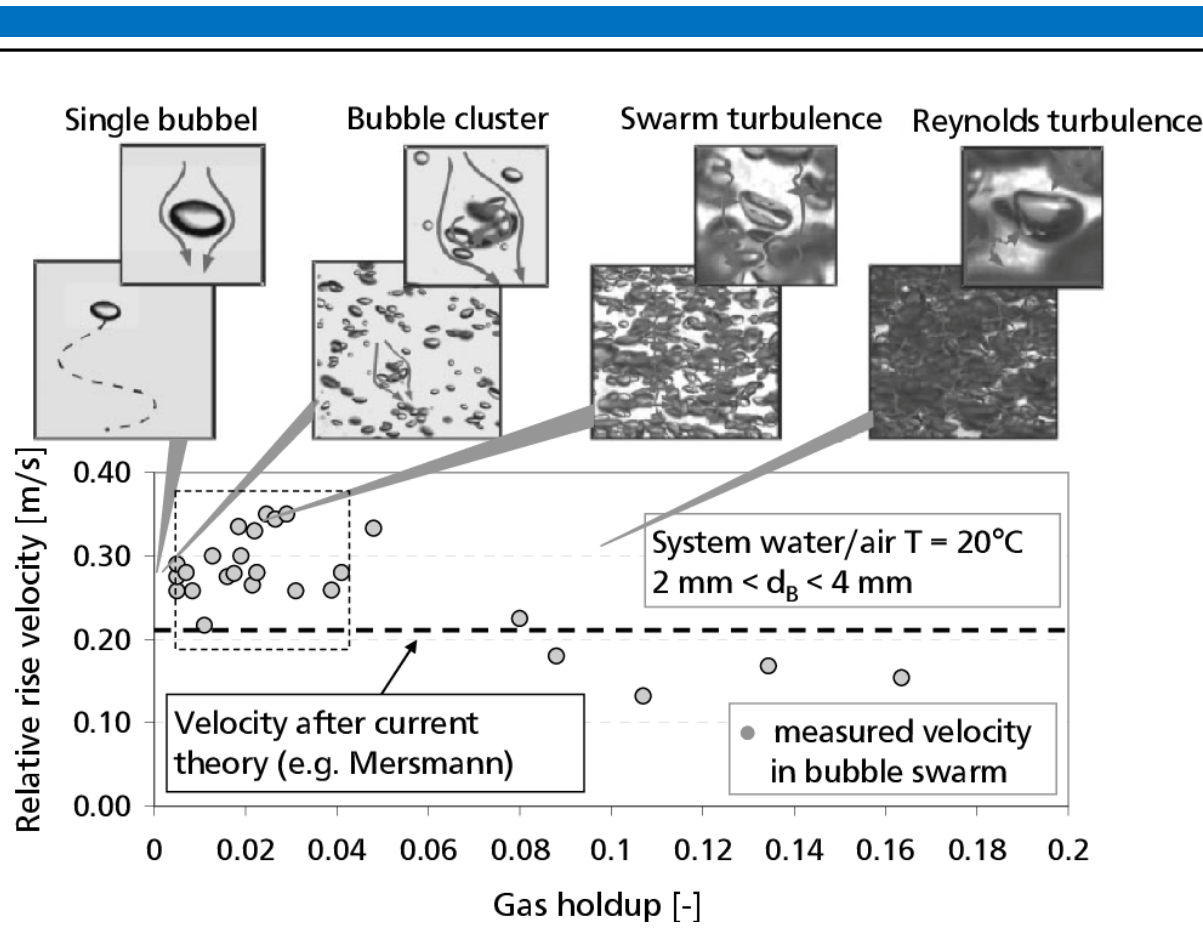


Figure 12. Relative rise velocity of a bubble swarm. Source: Henkel (2010, adapted from Schlüter (2002))



Vietnamese - German University

2.5 Literature review on the oxygen transfer in the MBBR Process

Numerous research studies have examined oxygen transfer in MBBR systems, with a particular focus on aeration aspects. These investigations have explored various factors, including the comparison of the coarse and fine bubble side aeration systems (Sander et al., 2016; Collivignarelli et al., 2019), the impacts of carrier media (Pham et al., 2008; Wei et al., 2016; Dias et al., 2018) and the filling fraction (Sun et al., 2015) on OTE, and effects of bubble plume (Li et al., 2011; Cheng et al., 2014). However, aspects related to filling fractions and diffuser densities have not been fully explored and have led to conflicting findings.

With respect to the impact of carriers on oxygen transfer, limited literature has been investigated in clean water tests. In coarse-bubble systems, a common agreement between existing studies is that the addition of carriers enhances OTE. Pham et al. (2008) evaluated 2 filling fractions of 25% and 50% and observed a marginal 1-2% enhancement in the SOTE. Similarly, Dias et al. (2018) found a significant increase in kLa and SSOTE at a filling fraction of 60%. Furthermore, Sander et al. (2016) suggested that the SSOTE increased from 2.9 %/m without carriers to 5.6 %/m at a 50% fill fraction. However, there is a dispute regarding the impact of airflow rate on the SOTE and SSOTE in coarse-bubble systems. While Pham et al. (2008); Sander et al. (2016); Collivignarelli et al. (2019) observed an increase in SOTE with higher airflow rates, Dias et al. (2018) reported the opposite trend.

In fine-bubble systems, the impacts of carriers on OTE were more controversial. Sander et al. (2016) found that an increase in the filling fraction led to a slight increase in the SOTE. Likewise, Sun et al. (2015) investigated filling fractions ranging from 0 to 50% and observed higher kLa values with carriers compared to no carriers. Interestingly, the kLa value of this study peaked at 30% filling fraction and then decreased gradually to 50% filling fraction. In contrast, Pham et al. (2008) reported a significant decrease in SOTE of 4-6% with the addition of carriers. Similar to coarse-bubble systems, the impact of airflow rate on the SOTE and SSOTE in fine-bubble systems remains a subject of dispute. Pham et al. (2008); Collivignarelli et al. (2019) found that the SOTE decreased with increasing airflow rates while Sander et al. (2016) reported the opposite trend.

In terms of the influence of the diffuser densities, limited literature has discovered the influence of diffuser density (DD), which refers to the area covered by the diffusers in relation to the total area of the tank floor (Rosso, 2018). Rosso (2018) suggested that an increase in DD could improve the OTE to a certain threshold. Excessive diffusers, however, can increase energy consumption and the risk of insufficient airflow per diffuser.

3. Materials and methods

This section aims to express the materials and methods to conduct oxygen transfer tests for both laboratory and pilot scales. It begins with an overview of the experimental setup, including details of the equipment and materials used, as well as selected operating parameters. Following that, critical parameters governing oxygen transfer mechanisms will also be demonstrated. Clear procedures shall ensure accurate results, which will pave the way for reliable inputs for subsequent discussions.

3.1 Experimental setup

3.1.1 Lab scale

The lab-scale experimentation employed a circular reactor with dimensions $H \times D = 1.2 \text{ m} \times 0.437 \text{ m}$. The water level was controlled at 1.0 m during oxygen transfer tests to maintain an effective water volume of 0.15 m^3 . Prior to each phase of diffuser run, the reactor was drained, cleaned with Citric acid monohydrate, and filled with clean water with pH in the range of 7.4-8.2 and conductivity in the range of $450\text{-}680 \text{ }\mu\text{S/cm}$. The reactor was then filled with plastic carriers (HXF25KLL, Christian Stöhr GmbH & Co., Germany) with a diameter of 25mm, a height of 25mm, a protected surface area of $342 \text{ m}^2/\text{m}^3$, a density of 0.95 kg/m^3 . The void volume of the HXF25KLL carrier was roughly 83%, calculated by using a 3D model to simulate the carrier's shape (see Section 7.2.6). A filling fraction ranging from 10% to 50% was chosen. Higher filling fractions were not considered, as complete mixing of the carriers within the reactor could not be guaranteed. Prior to each change of filling fraction, new carriers were added and soaked for around 12 hours in the reactor to remove any charge that might create a buoyancy effect affecting mixing negatively. Based on the time needed to remove buoyancy forces, the experimental plan was established. Overall, the experimental plan spanned a duration of three weeks, with the weekly schedule detailed in Section 7.2.1.

Two types of disc diffusers were sequentially investigated. Both discs were Model JetFlex HD 270 from Jäger Umwelt-Technik GmbH, Germany. The distance from the disc's membrane surface to the bottom of the reactor was 0.1 m. Disc 1 was a fine-bubble disc diffuser and featured the following specifications: a diameter of 268 mm, 3210 slits with each slit measuring 1.25 mm in length, a theoretical effective area of 0.031 m^2 , and a bubble size of 1-3mm. Disc 2 was also a fine-bubble disc diffuser with an increased slit length of 2 mm and a reduced theoretical effective area of 0.031 m^2 . The diffuser densities for Disc 1 varied from 17% to 21%, while those for Disc 2 ranged from 4% to 8%, depending on the airflow rates applied. The determination of the diffuser density and the theoretical effective area can be found in Section 7.2.5.

The DO concentrations and the water temperature were measured by four probes (Oxymax COS51D Endress & Hauser, Germany) located inside the tank, at the depth of 0.25, 0.4, 0.55, 0.7 m, respectively. Throughout the three-week experiment, all probes were maintained and calibrated on two occasions, each time before the disc replacement in order to guarantee reliable results. The DO concentration within the reactor was maintained at above 8 mg/L. The signals were recorded on a programmable logic controller (PLC) every 3 seconds. Atmospheric pressure, relative humidity, and air temperature were

measured by a hand-held device (Model GFTB 100, Greisinger Electronic, Germany). The experimental setup is outlined in Figure 13.

At each investigated filling rate, five values of specific air flow rates were examined, specifically 10, 15, 20, 25, and 30 $\text{Nm}^3_{\text{air}}/(\text{m}^3_{\text{water}} \cdot \text{h})$, which were corresponded to 1.5, 2.25, 3, 3.75, and 4.5 $\text{Nm}^3_{\text{air}}/\text{h}$. Such values were established based on reference studies conducted at the laboratory scale (see Table 1). The airflow rate was measured with a thermal flow sensor (Model U372, Hoentzsch, Germany), the air pressure was measured by a differential pressure transmitter (Model Delta P, Halstrup Walcher, Germany) and the air temperature was measured by a digital thermometer (Model Ad 15th, Amarell GmbH, Germany). The airflow was introduced by a rotary blower (Model DLT 01, Gardner Denver, Germany). The mixing condition in the reactor was observed visually from side views of the reactors.

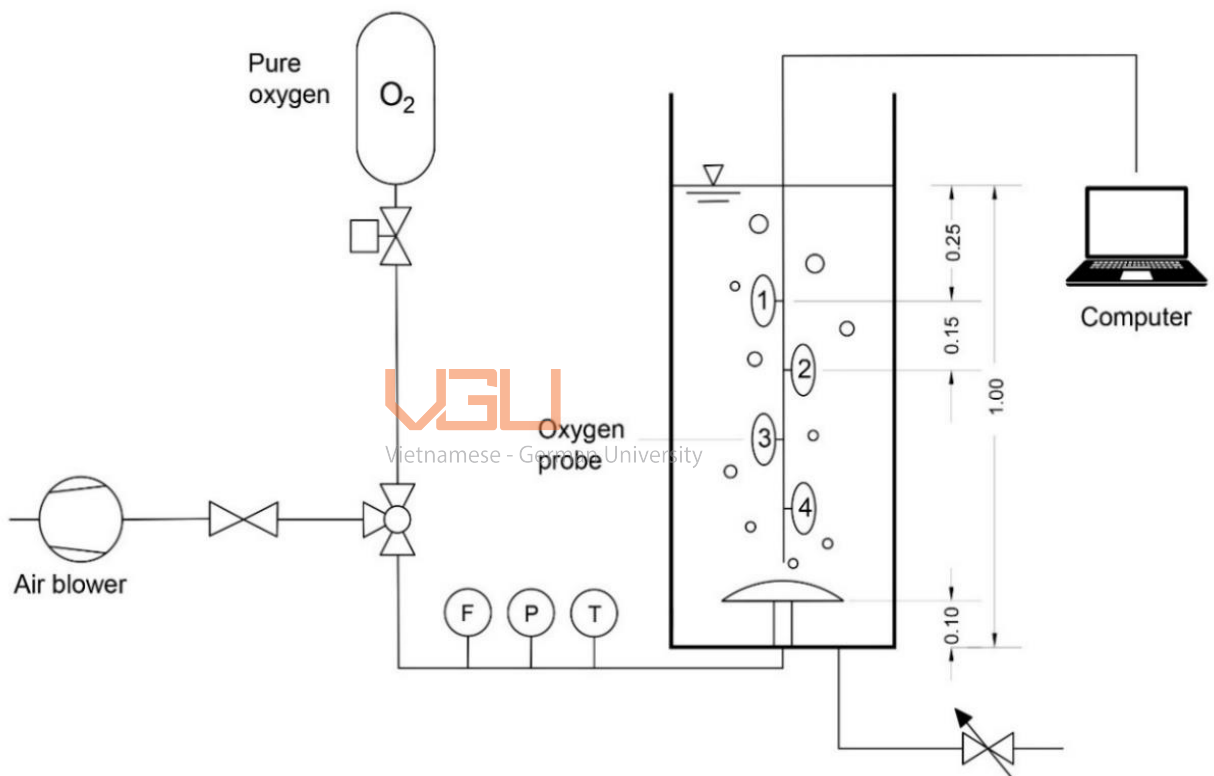


Figure 13. Schematic drawing of the lab-scale MBBR

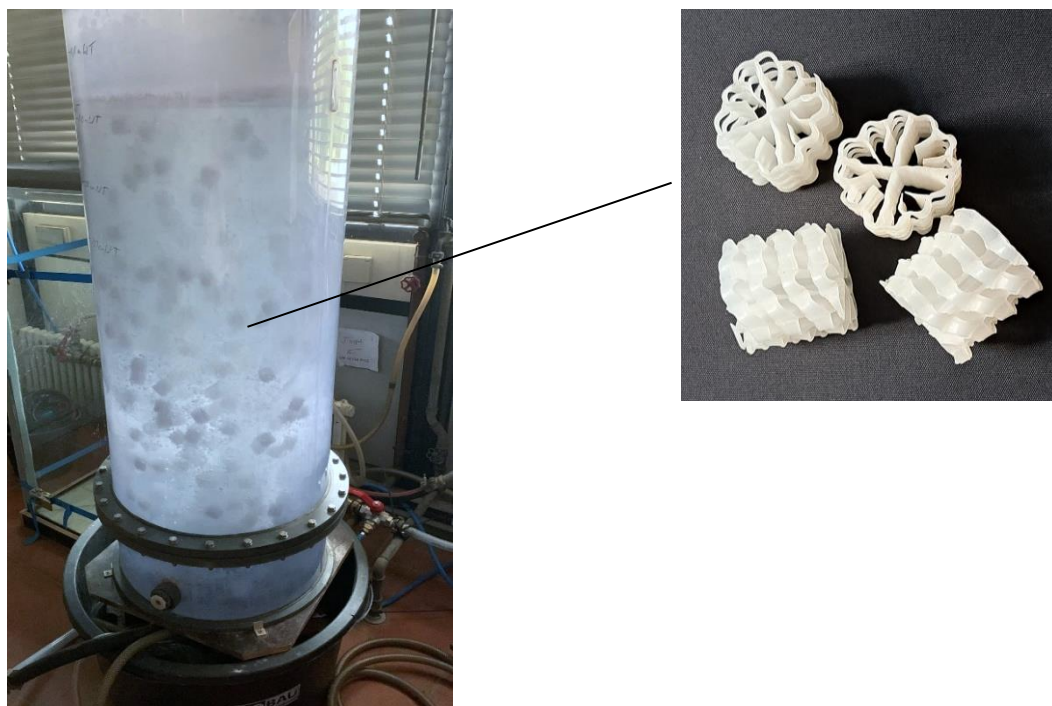


Figure 14. Experimental setup of the lab-scale MBBR with the HXF25KLL carrier

3.1.2 Pilot scale

In the pilot-scale setup, a rectangular reactor with 3.0 meters in length and 1.5 meters in width was employed. Clean water (pH in the range of 8.35-8.90 and conductivity in the range of 470-630 $\mu\text{S}/\text{cm}$), was introduced and the water depth is controlled at 3.8 m to maintain the effective water volume of roughly 17.1 m^3 . The reactor was equipped with sieves at the inlets and outlets to retain the carriers inside. Plastic HXF25KLL carriers were subsequently introduced, with the filling fraction ranging from 0 to 40% in 5% increments. Similar to lab-scale, prior to each change in filling fraction, new carriers were added and soaked to remove buoyancy forces. The time to achieve a complete mixing condition in pilot scale ranged from 1-2 days and based on this, the experimental plan was established. Overall, the experimental plan spanned a duration of seven weeks, with the weekly schedule detailed in in Section 7.2.1.

For the pilot scale, only disc diffuser 1 were utilized. There were 15 discs in total and the distance from the bottom of 0.165 m. The diffuser densities varied from 8.4% to 10.4%, depending on the airflow rates. The DO concentrations and the water temperature were measured with four probes (Oxymax COS51D Endress & Hauser, Germany) at the depth of 0.8, 1.3, 1.8, and 2.3 m. The DO concentration within the reactor was maintained at above 8 mg/L. The signals were recorded on a programmable logic controller (PLC) every 3 seconds. The schematic drawing and the experimental setup can be found in Figure 15 and Figure 16.

The airflow was introduced by a rotary blower (Model GM3S) from Aerzener Maschinenfabrik GmbH, Germany while the air flow rate was controlled by a gas meter (Model G65) from the same manufacturer. Atmospheric pressure, relativity humidity, atmospheric and line temperature were measured by a thermal meter (Model Almemo 2490, Ahlborn GmbH, Germany). The airflow rates were established

based on (a) reference studies (see Table 1, Section 2.2.2), which revealed that the minimum specific air flow rate for establishing a good mixing pattern was $1.18 \text{ Nm}^3_{\text{air}}/(\text{m}^3_{\text{water}}\cdot\text{h})$ and (b) typical MBBR design values of $6\text{--}8 \text{ m}^3/\text{m}^2_{\text{basin floor}}\cdot\text{h}$ from McQuarrie and Boltz (2011), equivalent to $1.58\text{--}2.11 \text{ Nm}^3_{\text{air}}/(\text{m}^3_{\text{water}}\cdot\text{h})$ for the pilot scale of this study. Consequently, at each investigated filling rate, five specific air flow rates of 1.3, 2.5, 3.7, 4.9, and $6.1 \text{ Nm}^3_{\text{air}}/(\text{m}^3_{\text{water}}\cdot\text{h})$ were investigated, which correspond to 22, 43, 63, 84, and $104 \text{ Nm}^3_{\text{air}}/\text{h}$. Some tests were completed in duplicate to assess reproducibility. The mixing condition was observed visually from side views of the reactor.

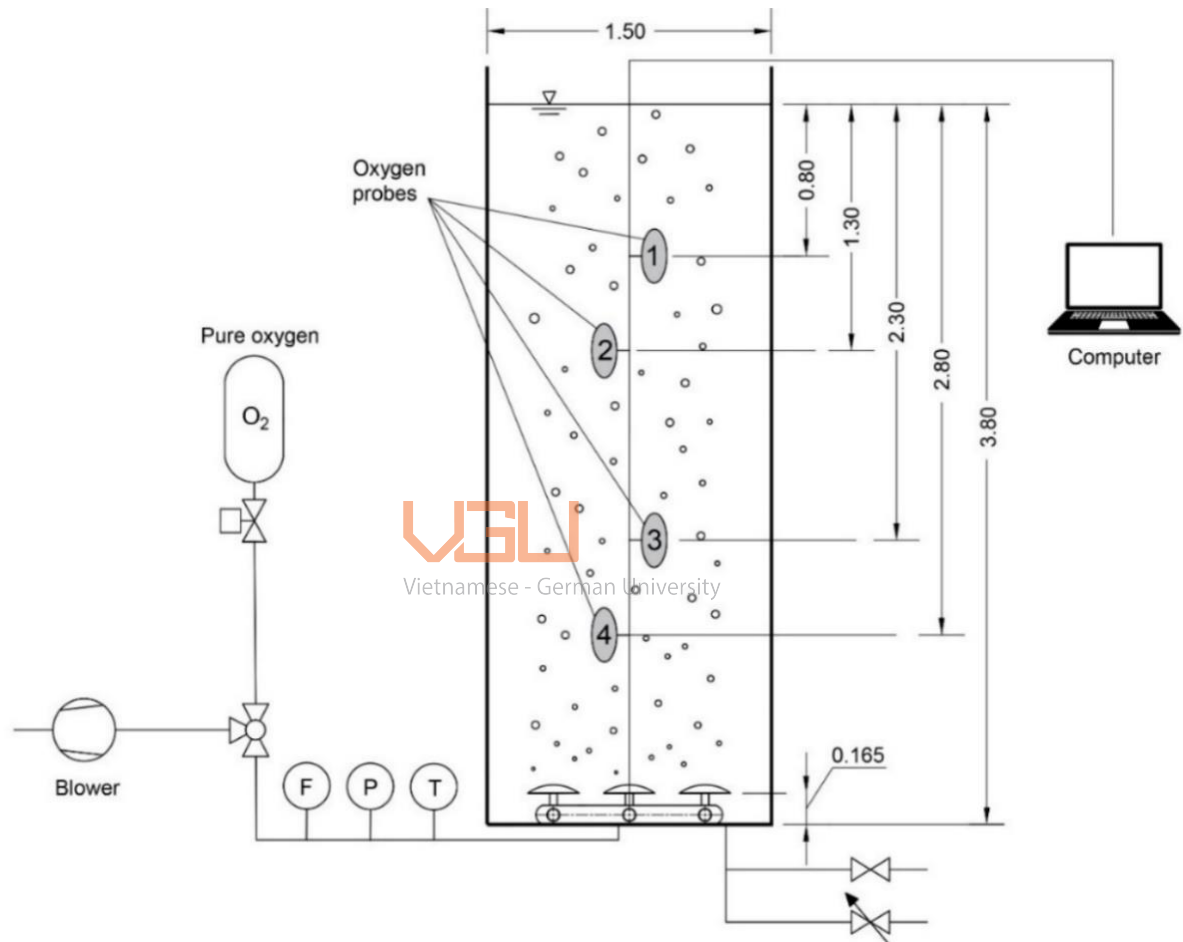


Figure 15. Schematic drawing of the pilot-scale MBBR



Figure 16. Experimental setup of the pilot-scale MBBR

3.2 Determination of important parameters

The first aspect to investigate is the operating air volume flow required to reach the selected standard airflow rate. In the laboratory setting, the operating air volume flow was indicated by the device. In the pilot-scale experiments, it was more complicated since the operating air volume flow was controlled by the frequency of the blower. A detailed explanation of the methodology employed to obtain the desired standard airflow rate in the pilot-scale experiments will be presented in Section 7.2.4.

Then, the operating airflow rate was converted into the standard airflow rate by using Eq. (3-1), which was modified from DWA-M 229-1 (2017):

$$Q_{L,N} = Q_{L,o} \cdot \frac{1013}{P_{atm} + P_{line} - P_{water\ vapor}} \cdot \frac{273 + T_p}{273} \quad (3-1)$$

where $Q_{L,N}$ is the airflow rate at standard conditions [m^3h^{-1}], $Q_{L,o}$ is the airflow rate at operating conditions [m^3h^{-1}]; P_{atm} is the atmospheric air pressure [mbar]; P_{line} is the air pressure in the pipeline; [mbar]; $P_{water\ vapor}$ is the water vapor pressure [mbar]; and T_p is the temperature in the pipeline [$^{\circ}C$].

The atmospheric air pressure and the air pressure in the pipeline were measured by measuring devices while the water vapor pressure was determined by Eq. (3-3):

$$P_{water\ vapor} = \frac{P_s \cdot \phi}{100} \quad (3-2)$$

where P_s is the saturated vapor pressure [mbar] and ϕ is the relative humidity [%]

The saturated vapor pressure was derived from DWA-M 229-1 (2017):

$$P_s = 6.112 \cdot EXP\left(\frac{17.62 \cdot T_{air}}{243.12 + T_{air}}\right) \quad (3-3)$$

where P_s is the saturated vapor pressure [mbar] and T_{air} is the atmospheric temperature [%]

The second aspect to examine is the mass transfer coefficient (k_{La}). The k_{La} was calculated for each DO probe by nonlinear regression using the software OCAW (Fröse & Olderdisen, Germany). The individual probe parameters such as k_{La} and C^* were controlled to remain within $\pm 5\%$ deviation from the mean values. The test quality was evaluated through the course of the residuals over time (see Section 7.2.1).

Following that, the mean values of C^* and k_{LaT} were converted to standard conditions (water temperature at 20 °C and pressure at 1 atm) by using Eqs. (3-4) and (3-5):

$$k_{La20} = k_{La} \cdot \theta^{20-T} \quad (3-4)$$

$$C_{20}^* = C^* \cdot \left(\frac{1}{\tau \cdot \Omega} \right) \quad (3-5)$$

where k_{La} is the volumetric mass transfer coefficient [h^{-1}]; θ is the empirical temperature correction factor ($= 1.024$); C^* is the DO saturation concentration in water at test conditions [$mg L^{-1}$]; C_{20}^* is the DO saturation concentration in water at standard conditions [$mg L^{-1}$]; τ is the temperature correction factor, described by Eq. (3-6); Ω is the pressure correction factor, described by Eq. (3-7); and T is the water temperature during test [$^{\circ}C$].

$$\tau = \frac{C_{st}^*}{C_{s20}^*} \quad (3-6)$$

where C_{st}^* is the tabular value of DO surface saturation concentration [$mg L^{-1}$], at test temperature, standard pressure ($= 1013$ hPa and 100% relative humidity); and C_{s20}^* is the tabular value of DO surface saturation concentration [$mg L^{-1}$], at 20 °C, 1013 hPa, and 100% relative humidity.

$$\Omega = \frac{p_b}{p_s} \quad (3-7)$$

where p_b is the barometric pressure during test [hPa]; and p_s is the standard barometric pressure ($= 1$ [atm] or 1013 [hPa]).

The target for aeration design is to provide oxygen to the water to meet the oxygen requirements. Thus, there is a need to develop a parameter that reflects to which extent oxygen is transferred in clean water conditions. The amount of oxygen supplied to the water per unit time can be demonstrated by the descriptor known as oxygen transfer rate (OTR) (Rosso, 2018). The OTR [$kgO_2 h^{-1}$] can be evaluated by the overall volumetric mass transfer coefficient, k_{La} by the following equation:

$$OTR = k_{La} \cdot (C^* - C_L) \cdot V_{eff}. \quad (3-8)$$

where OTR is the oxygen transfer rate [$kgO_2 h^{-1}$]; k_{La} is the volumetric mass transfer coefficient [h^{-1}]; C^* is dissolved oxygen in water at saturation [$kgO_2 m^{-3}$]; C_L is dissolved oxygen in water [$kgO_2 m^{-3}$]; and V is effective water volume [m^3].

The mass of oxygen transferred per unit of time into water under standard conditions (clean water; no fouling factor $F = 1$; DO concentration in water = 0 mg/L; water temperature = 20°C; and standard

atmospheric pressure: 1,013 hPa) can be expressed as the standard oxygen transfer rate (SOTR) (Mueller et al., 2002)

$$SOTR = \frac{k_L a_{20} \cdot C_{20}^* \cdot V_{eff.}}{1000} \quad (3-9)$$

where SOTR is the standard oxygen transfer rate [kgO₂ h⁻¹]; $k_L a_{20}$ is the volumetric mass transfer coefficient at 20°C and 1,013 hPa [h⁻¹], C_{20}^* is the DO saturation concentration at 20°C [mg L⁻¹]; and V is the effective water volume [m³].

However, the OTR solely represents the capacity of the aeration system without considering the efficiency of oxygen transfer. Therefore, it is necessary to define additional parameters. For subsurface aeration devices (such as fine- or coarse-bubble diffusers), the oxygen transfer efficiency (OTE, %) can be used, defined as the fraction of oxygen supply that is actually transferred or dissolved into the liquid (Rosso, 2018). The OTE is a useful parameter to compare different technologies, as well as to monitor aeration systems over an extended time in operation (Rosso, 2018). The OTE value is calculated by the following equation:

$$OTE = \frac{OTR}{W_{O_2}} \sim \frac{(O_{2,in} - O_{2,out})}{O_{2,in}} \quad (3-10)$$

where OTE is the oxygen transfer efficiency [%]; OTR is the oxygen transfer rate [kgO₂ h⁻¹]; W_{O_2} is the mass flow of oxygen fed to the aeration tank [kgO₂ h⁻¹]; and $O_{2,in}$ and $O_{2,out}$ represent mass fluxes of oxygen in and out of the clean water volume.

Under standard conditions, the standard oxygen transfer rate can be expressed as (Mueller et al., 2002):

$$SOTE = \frac{SOTR}{0.3 \cdot Q_{L,N}} \cdot 100 \quad (3-11)$$

where SOTE is the standard oxygen transfer efficiency [%]; SOTR is the standard oxygen transfer rate [kgO₂ h⁻¹]; $Q_{L,N}$ is the airflow rate at standard conditions [Nm³/h]; and 0.3 represents the mass of oxygen in kilogram per cubic meter air at standard conditions ($p_{atm} = 1,013$ hPa; $T_{air} = 0^\circ\text{C}$)

Another important parameter for comparing diffused aeration systems is the specific standard oxygen transfer efficiency (SSOTE), considering more on the depth of submergence (DWA-M 229-1, 2017):

$$SSOTE = \frac{SOTR}{h_D \cdot Q_{L,N} \cdot 0.3} \cdot 100 \quad (3-12)$$

where SSOTE is the specific standard oxygen transfer efficiency [%/m]; SOTR is the standard oxygen transfer rate [kgO₂ h⁻¹]; $Q_{L,N}$ is the airflow rate at standard conditions [Nm³/h]; 0.3 represents the mass of oxygen in kilogram per cubic meter air at standard conditions ($p_{atm} = 1,013$ hPa; $T_{air} = 0^\circ\text{C}$); and h_D is the depth of submergence, which is the distance between the disc membrane and the water level without aeration [m].

Finally, it is important to determine to which extent the carriers shall added, described as the term filling fraction. The filling fraction in general can be described using Eq. (2-1):

$$FF = \frac{V_{bulk-carrier}}{V_{bulk-carrier} + V_{effective\ water}} \cdot 100$$

where FF is the filling fraction [%]; $V_{carrier}$ is the bulk volume of the carriers [m^3]; and $V_{effective\ water}$ is the effective water volume [m^3];

The selection of the filling fraction is typically predetermined according to specific design and requirements. To achieve the target filling fraction, the combined volume between the bulk volume of the carriers and the effective water volume is maintained at a specific value. Based on the combined volume and the target filling fraction, the bulk volume of the carriers can be calculated using Eq. (2-1). Subsequently, carriers can be introduced to reach this calculated bulk volume. The determination of the bulk volume of the carriers and the effective water volume will be further discussed in Section 7.2.3.



Vietnamese - German University

4. Results

In this section, the results related to the experiments in both lab- and pilot- scales are highlighted. The main objective is to demonstrate the influence of carriers on the performance and behavior of each system under various conditions. These results are crucial for gaining a comprehensive understanding of each system and can serve as a basis for further discussions and recommendations.

4.1 Lab scale

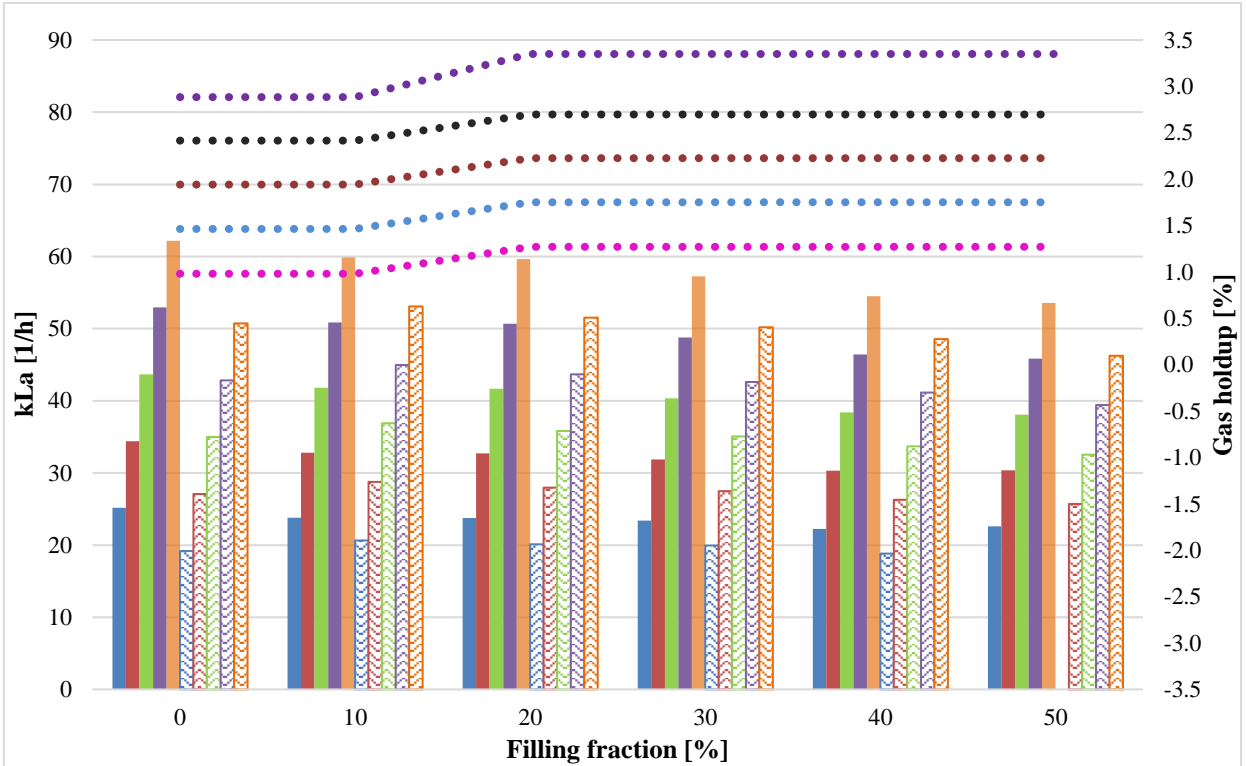
In the lab-scale experiments, two types of disc diffusers were sequentially investigated with the filling fractions varied from 0% (without any carriers) to 50%. The mixing condition observed visually from side views of the reactors revealed that all tests fulfilled the required condition of establishing a roll pattern except for the filling fraction of 50% at 1.5 Nm³/h for Disc 2. The results of the oxygen transfer test for the pilot scale are demonstrated in Figure 17–19.

With respect to Disc 1, the k_{La} decreased with increasing filling fraction. Comparing the results by statistical analysis using the paired t-tests, it was shown that the k_{La} values in all the filling fractions were significantly different for those in clean water without carriers ($p < 0.05$). Similarly, the SSOTE shared the same trend with the k_{La}, revealing that the introduction of carriers resulted in lower SSOTE values compared to clean water without any carriers (see Figure 18). It was noticeable that the SSOTE decreased with an increase in AFR. As shown in Figure 19, the SSOTE demonstrated a significant decline of 0.9-1.1 %/m between 1.5 and 3.0 Nm³/h while from 3.0 to 4.5 Nm³/h, the SSOTE slightly decreased by roughly 0.3%/m.

VGU
Vietnamese - German University

Moving on to Disc 2, it was observed both the k_{La} and SSOTE values were lower than Disc 1. However, there was no clear trend for the k_{La} and SSOTE through increasing the filling fraction. Initially, at the lowest filling fraction (10%), the SSOTE values increased significantly for all airflow rates ($p < 0.05$). However, the SSOTE values dropped gradually at 20% and 30% filling fractions, showing values that were not statistically different from 0% clean water without carriers ($p > 0.05$). Subsequently, the SSOTE decreased gradually thereafter until 50% filling fraction. Similar to Disc 1, the SSOTE decreased with an increase in AFR. The SSOTE recorded a significant fall of 0.54-0.75 %/m between 1.5 and 3.0 Nm³/h and a slight decrease of around 0.2%/m from 3.0 to 4.5 Nm³/h.

Meanwhile, the gas holdup values ranged from 1% to 3%, which fall between the typical range of fine bubble aeration systems (0.5% to 4.8%). Despite that, the impact of carriers on the gas holdup remained uncertain for both Discs. This could be explained that small-scale observations have not provided conclusive evidence. To gain a better understanding of the effects of carriers, further experiments in the pilot-scale would be required. However, there was a sense that gas holdup may increase with higher gas velocity and filling fraction.



Airflow rate

Disc 1 ■ 1.5 Nm³/h ■ 2.25 Nm³/h ■ 3.0 Nm³/h ■ 3.75 Nm³/h ■ 4.5 Nm³/h
 Disc 2 ■ 1.5 Nm³/h ■ 2.25 Nm³/h ■ 3.0 Nm³/h ■ 3.75 Nm³/h ■ 4.5 Nm³/h

Gas holdup

● 1.5 Nm³/h ● 2.25 Nm³/h ● 3.0 Nm³/h ● 3.75 Nm³/h ● 4.5 Nm³/h

Figure 17. Effects of carrier media on mass transfer coefficient and gas holdup in lab-scale experiments

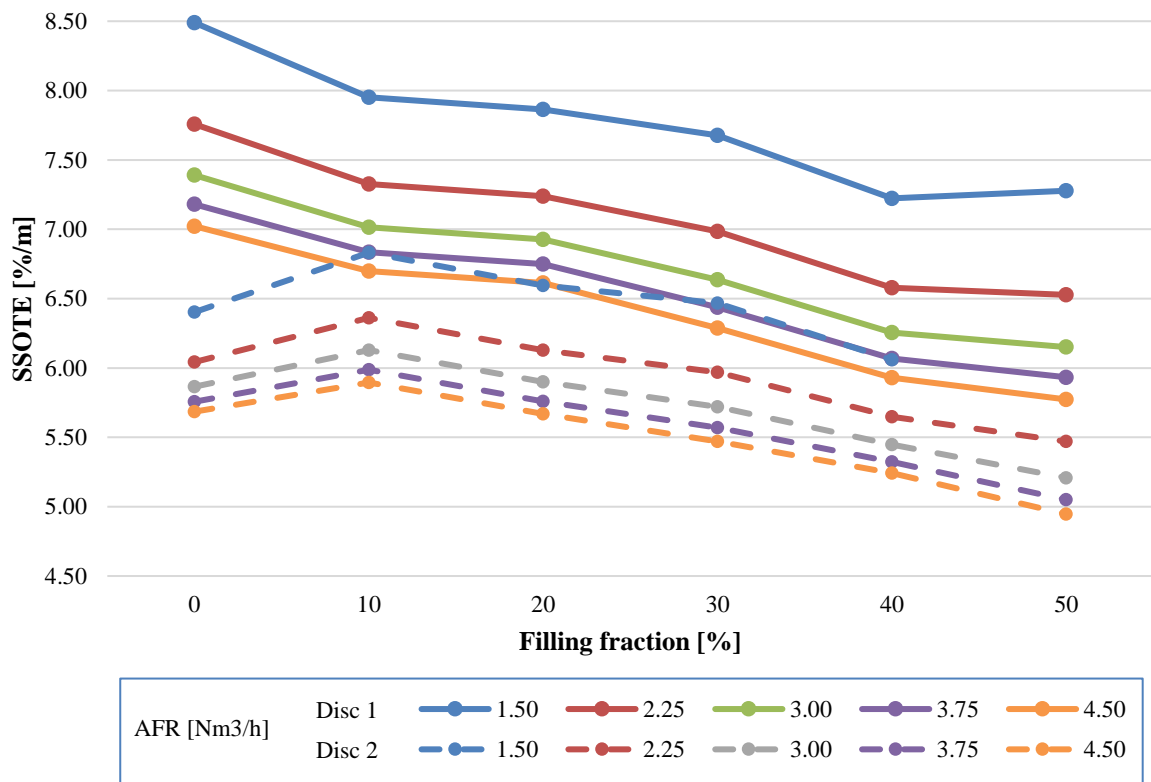


Figure 18. Effects of carrier media on the specific standard oxygen transfer efficiency in lab-scale.

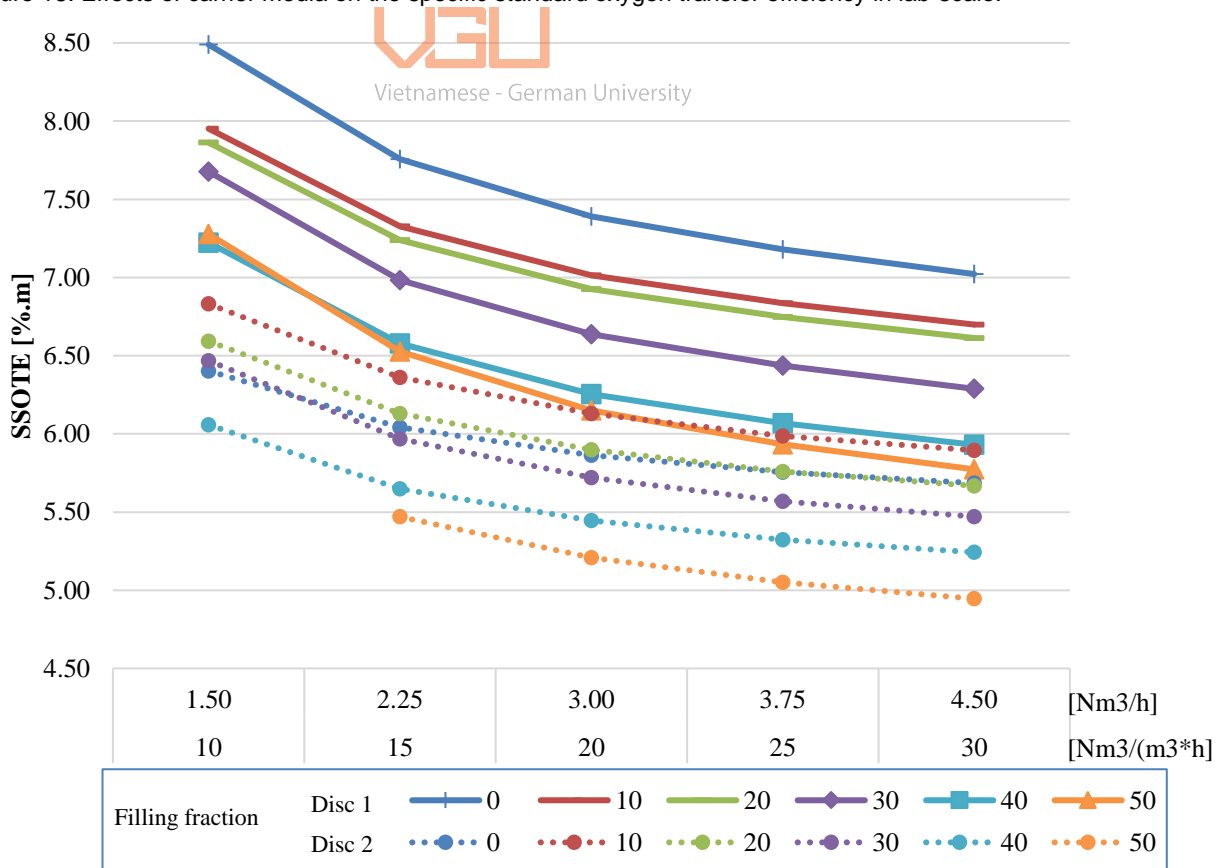


Figure 19. Impact of airflow rates on the specific standard oxygen transfer efficiency in lab-scale.

4.2 Pilot scale

In the pilot-scale experiments, the filling fractions varied from 0% (without any carriers) to 40% while the (specific) airflow rates ranged from 22 to 104 Nm³/h (1.3 to 6.1 Nm³/m³*h). Compared to the lab-scale, mixing conditions posed challenges and affected the reliability of results. Visual observation revealed that only the highest airflow rate (104 Nm³/h or 6.1 Nm³/m³*h) provided sufficient mixing to all filling fractions while the maximum capacity for the airflow rates of 22, 43, 63, and 84 was at 25%, 25%, 30% and 35% filling fraction, respectively. Thus, tests with insufficient mixing were not documented due to the accumulation of unmixable carriers as thick layers on top of the reactors.

Additionally, at high filling fractions, slow mixing during start-up became an issue. The HPOD method involved introducing pure oxygen to the system while the blower operated at a low frequency. Once reaching the DO concentration of around 25 mg/L, the blower could start at the target frequency. However, the initial operation at low frequency with high filling fractions facilitated the carriers to accumulate and form a thick layer on top of the reactor. This layer did not dissipate instantly once the blower started at the target frequency. Consequently, the top region displayed different hydraulic patterns, causing the top probe to show different kLa results compared to other probes. Specifically, the kLa values obtained from the top probe were 5% higher than the mean values from other probes. Consequently, the readings from this probe were neglected, meaning that only 3 out of 4 probes were adopted to measure the DO concentrations.

Figure 20 summarizes the kLa results in the pilot scale. Overall, the presence of carriers negatively affected the kLa at all airflow rates. Comparing the results by statistical analysis using the paired t-tests, it was shown that the kLa values in all the filling fractions were significantly different for those in clean water without carriers ($p < 0.05$). Only at 20 and 25% from 43 to 104 Nm³/h (from 2.5 to 6.1 m³_{air}/(m³_{water}*h)), no significant difference was observed ($p > 0.05$). Compared to the lab scale, the kLa values in the pilot scale were significantly lower at the same airflow rate applied per disc. The ratio between the kLa values in the lab scale and in the pilot scale was roughly 2.6, which interestingly aligned with the ratio between the Height/Width dimensions of the pilot-scale reactor. This finding highlights the importance of considering scale effects when transitioning from lab-scale experiments to pilot-scale operations. Additionally, it was notable that the carriers improved the linear relationship between the kLa and airflow rate. As shown in Figure 20, increasing the filling fraction gradually increased the R-squared values from 0.9962 at 0% to 0.9998 at 30% filling fraction.

To facilitate result comparison, kLa values at selected airflow rates were calculated using linear equations derived from real values. Figure 21 demonstrates the kLa values obtained at 5 specific airflow rates. Statistical analysis using the paired t-tests confirmed the reliability of kLa values obtained by linear equations, showing no significant difference from real values ($p > 0.05$). It can be seen from Figure 21 that there was no clear trend for the kLa with the increase of filling fraction. Initially, at the lowest filling fraction (5%), the kLa values dropped significantly for all airflow rates. Then, the kLa values increased gradually to peak at 25% filling fraction before dropping gradually thereafter.

Figure 21 also presents gas holdup results. The gas holdup values ranged from 0.3% to 2.5%, which was slightly lower than the typical range of fine bubble aeration systems (0.5% to 4.8%). In comparison to

the lab scale, the effect of carriers on the gas holdup was more obvious in pilot scale. It can be seen from Figure 21 that the gas holdup increased with increasing gas velocity and filling fraction.

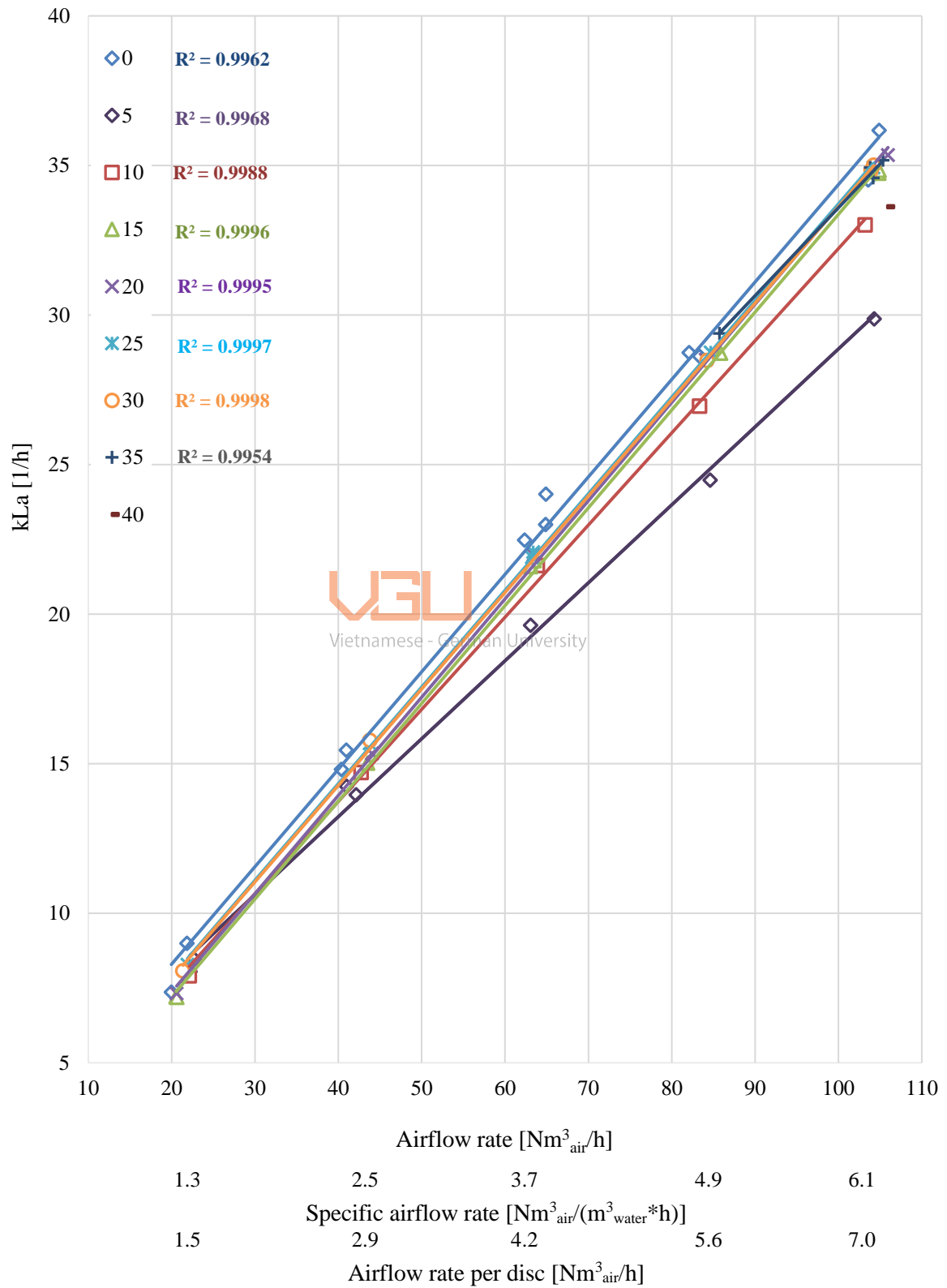


Figure 20. Effects of carrier media on mass transfer coefficient.

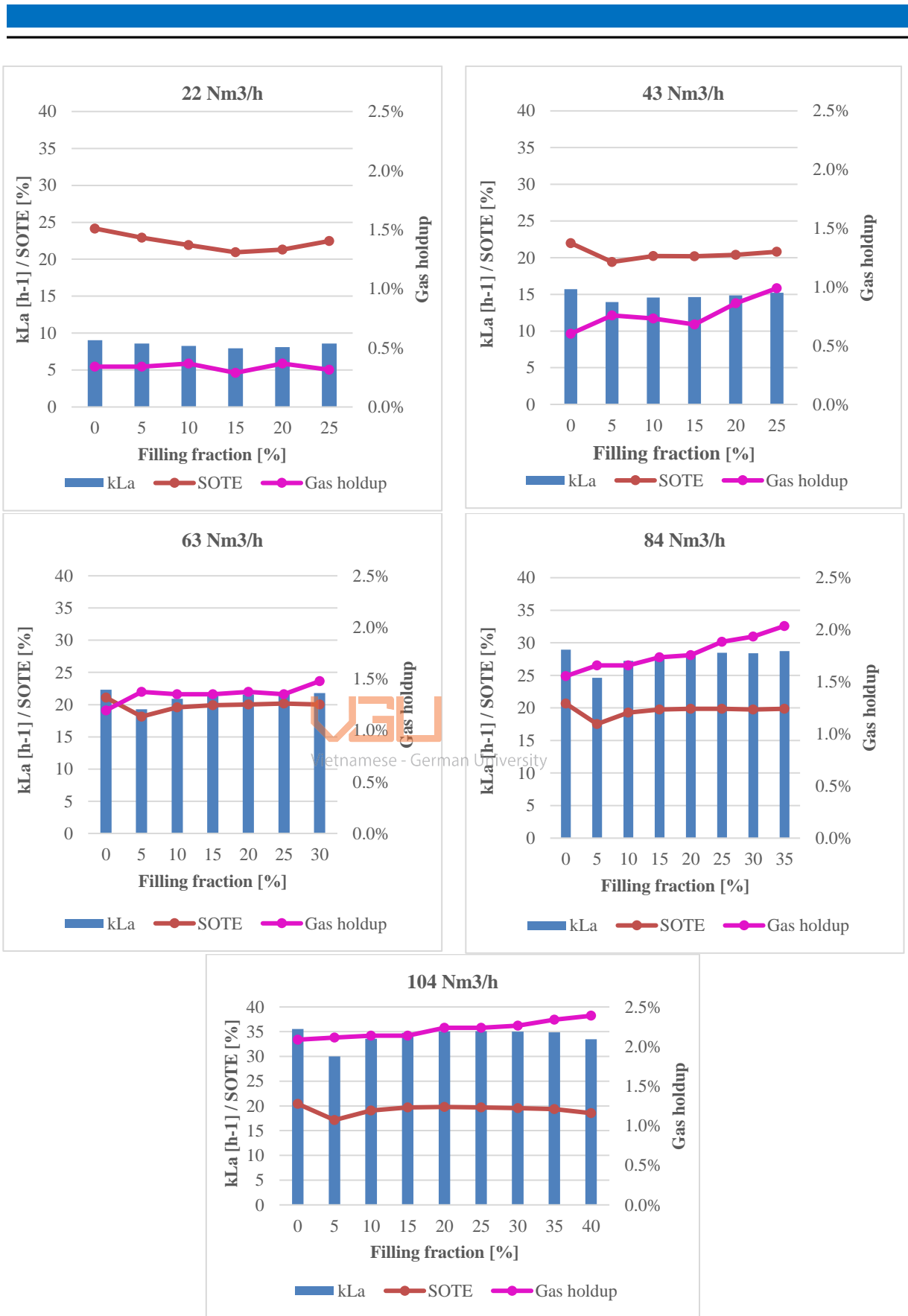


Figure 21. Effects of carrier media on mass transfer coefficient, standard oxygen transfer efficiency and gas holdup

The impact of filling fraction on the SSOTE results was also considered (see Figure 22–23). Similar to the kLa , the introduction of carriers resulted in lower SSOTE values compared to clean water without any carriers. Statistical analysis using the paired t tests revealed that the SSOTE values in all the filling fractions were significantly different for those in clean water without carriers ($p < 0.05$). The SSOTE values ranged from 6.65 %/m to 5.6 %/m, which was lower than values supplied by the manufacturer ranging from 7%/m to 6%/m and values yielded in lab-scale ranging from 8.5%/m to 7.22%/m. Despite this, there was a common trend between lab- and pilot-scale: the SSOTE decreased with an increase in AFR. As shown in Figure 23, the SSOTE dropped significantly between 1.3 and 3.7 Nm³/h per disc while above 3.7 Nm³/h per disc, the SSOTE decreased slightly for all filling fractions.

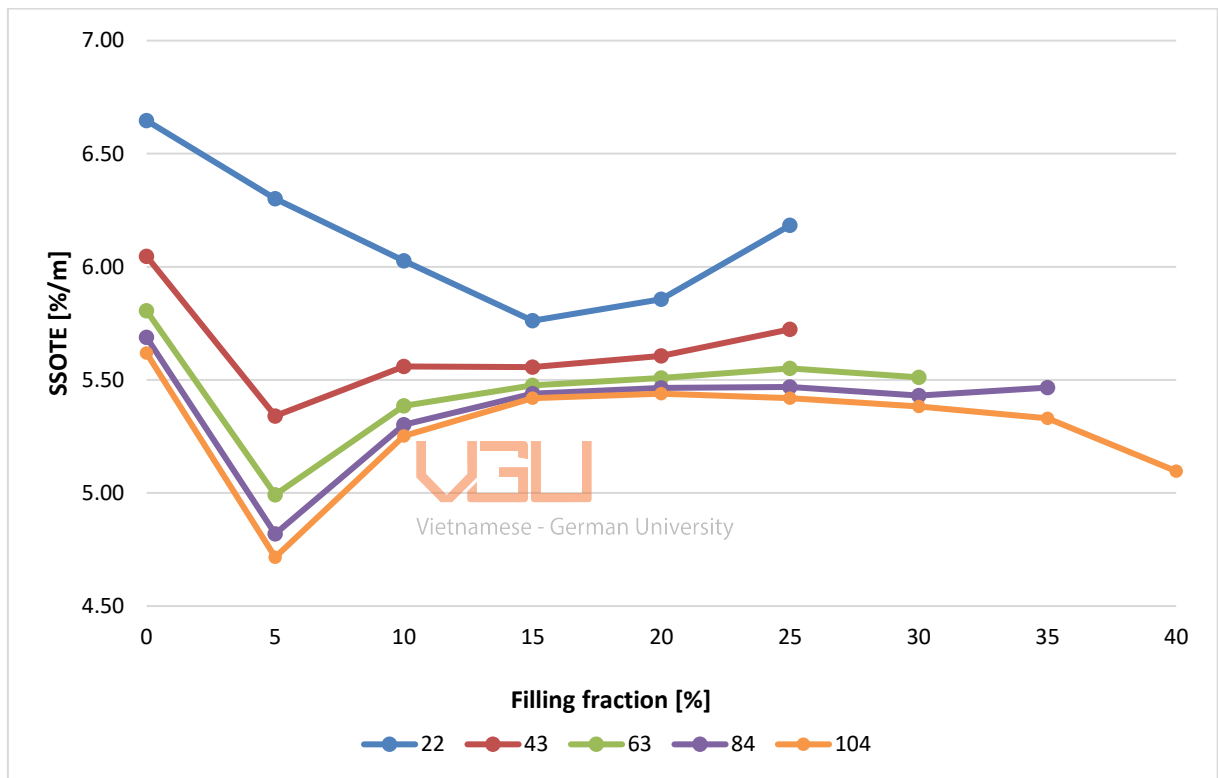


Figure 22. Impact of filling fraction on the specific standard oxygen transfer efficiency in pilot-scale

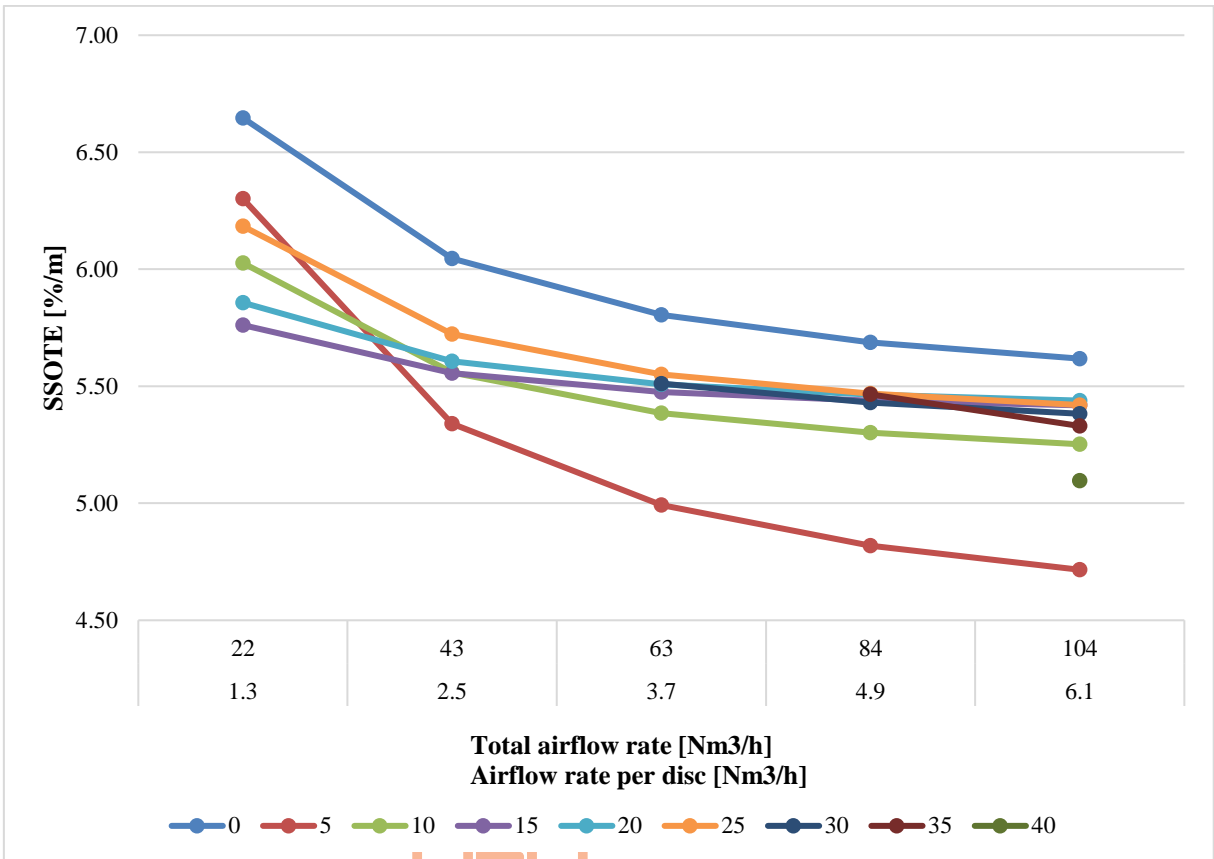


Figure 23. Impact of airflow rates on the specific standard oxygen transfer efficiency in pilot-scale.

Vietnamese - German University

5. Discussion and outlook

5.1 Effect of the carrier media on the oxygen transfer efficiency

The first impression from the results is that the presence of carriers negatively affected the oxygen transfer efficiency for fine-bubble diffusers, both in lab- and pilot-scale experiments. This finding aligns with previous studies by Pham et al. (2008) and Collivignarelli et al. (2019), which also reported a decrease in the SOTE with increasing filling fraction and airflow rate for fine-bubble diffusers. The second impression is that the gas holdup increases with increasing filling fraction and gas velocity. The gas holdup values obtained in the lab scale ranged from 1% to 3.5%, which fall within the typical range of fine bubble aeration systems of 0.5% to 4.8%. Meanwhile, the value obtained in the pilot scale (0.3% to 2.5%) was slightly lower than the typical range of fine bubble aeration systems. The decrease in $kLa/SOTE$ and the increase in gas holdup compared to clean water without carriers could be attributed to the two main factors:

(a) Vertical rotation of the carriers. The vertical rotation of the carriers exerted additional downward forces on growing bubbles, which was also observed by Collivignarelli et al. (2019). These forces delayed the bubble motion and reduced liquid velocity, leading to a higher gas holdup in the reactor. Simultaneously, these forces also promoted bubble coalescence that subsequently lowered the $kLa/SOTE$.

(b) Characteristics of HXF25KLL carrier media. It has been proven that the physical properties of the carrier media have a significant impact on the hydraulic characteristics of moving attached growth systems (Herrling et al., 2015; Dias et al., 2018). In the study on the flow regime within a carrier media, Herrling et al. (2015) reported an increase in gas velocity within a cylindrical carrier media (AnoxKaldnes K1), which shares the same cylindrical shape of the HXF25KLL carrier used in this study. Here, in this study, increased gas velocity was observed in the pilot scale at low filling fractions. Thus, increased gas velocity led to less contact time between gas and liquid phases, subsequently decreasing the $kLa/SOTE$.

Applying these concepts, the effect of filling fractions on the SOTE could be elucidated as follows:

In pilot-scale experiments, at the lowest filling fraction (5%), the combined effects of the vertical rotation and the characteristics of the carriers significantly reduced the oxygen transfer by promoting bubble coalescence and increased gas velocity. Next, from 10% to 25% filling fraction, the increase in filling fraction facilitated enhanced bubble shearing effects caused by the mesh structure and outer fins of the carriers, as reported by Sun et al. (2015) and Sander et al. (2016). As a result, this effect promoted bubbles to break up into smaller bubbles, thereby enhancing the kLa . Concurrently, the addition of more carriers also inhibited the increase in gas velocity by blocking mechanisms, thereby enhancing the kLa . However, the kLa only increased to a certain extent before dropping due to the decreased fluidization capacity of the carriers once introducing more carriers. This reduction in fluidization is believed to weaken the turbulent flow state of the water. On the one hand, the reduced fluidization led to fewer interactions and collisions among bubbles, suppressing bubble breakup and causing a drop in the kLa

(Sun et al., 2015). On the other hand, the reduced turbulence degree of water provided higher transfer resistance from the liquid film, subsequently lowering the k_L as well as the kLa (Yang et al., 2001).

In lab-scale experiments, similar behavior was observed as the vertical rotation of the carriers and increased gas velocity led to a decline in the OTE. Disc 2 also exhibited this behavior, with a slight difference at low filling fractions (10-20%) where the SOTE actually increased. At such filling fractions, a noticeable increase in gas hold-up was observed, leading to an enhancement in bubble breakup. However, the SOTE increased only to a certain extent before the reduced effect of carrier fluidization occurred, resulting in a decrease in SOTE thereafter.

Considering more on the kLa , observations at 0% filling fraction in the pilot scale revealed that the kLa did not follow in a simple linear relationship with the airflow rate. At higher airflow rates, the kLa values tend to deviate below the regression line. This finding is consistent with Cheng et al. (2014), who claimed that the increase in the aeration rate shall influence the regular distribution of the bubble plume movement and the velocity distribution, leading to a nonlinear change of kLa . Interestingly, the introduction of carriers in this study appeared to counteract this effect. Throughout the pilot-scale experiments, the increase in filling fraction demonstrated a gradual rise in R-squared values, reaching from 0.9962 at 0% to 0.9998 at 30% filling fraction.

5.2 Effect of the reactor geometry on the oxygen transfer efficiency

Table 4 summarizes the SOTE values in clean water without carriers obtained in this study compared to other research conducted at the same pilot scale. It can be seen that the SOTE values are higher than those reported by Collivignarelli et al. (2019), Pham et al. (2008) and Dias et al. (2018), but lower than values reported by Sander et al. (2016). Of interest is that the ratios of height to width (or diameter) of such studies were 1.54, 1.75, 1.3 and 4.92, respectively. This suggests that the SOTE is influenced by the geometry of the reactor. This idea is supported by the studies of Wagner (1998), cited as Mueller et al. (2002); Cheng et al. (2014), which revealed that a higher ratio of H/W would lead to higher SOTE. The increase in SOTE with increasing depth could be explained by Eq. (3-9), where an increase in height boosts 2 out of 3 components in this equation. Despite a decrease in the kLa , a higher height would increase the static pressure over water depth, thereby increasing the saturation concentration of oxygen (C_s). Furthermore, a higher height would also enhance the effective water volume within the reactor. As a result, this finding suggested that the MBBR systems could operate with deep tanks to maximize the SOTE.

However, the MBBR systems should not be operated with extensively high depth. The study of Cheng et al. (2014) revealed that a higher ratio of H/W could reduce the oxygen transfer performance, which is also supported by the observation from this study. It is explained by the effect of bubble plume on different depths of submerge (h_D), as illustrated in Figure 24. When h_D was lower than 2m (left photograph), the swing amplitude was small. The opposite behavior was observed for a h_D of higher than 2.5m. Once the swing amplitude is high, the bubble plume overlaps others, leading to increased bubble velocity and promoted bubble coalescence effects – factors decreasing the kLa . Operating with extensively high depth also poses potential problems like decreased CO₂ stripping from wastewater, lowered pH values that impairs the nitrification processes, and floating sludge in the secondary clarifiers. (Mueller et al., 2002)

Furthermore, the reactor shape also plays a critical role. As shown in Table 4, Collivignarelli et al. (2019) yielded a SOTE value of 16.13% while Pham et al. (2008) achieved around 15.8 % at 2.88 $\text{Nm}^3_{\text{air}}/(\text{m}^3_{\text{water}}*\text{h})$ whereas the H/W ratios 1.54 vs 1.75, respectively. Thus, it indicates that circular reactors tend to yield higher SOTE in comparison with rectangular reactors because circular reactors have better mixing conditions in the corners compared to rectangular reactors

Table 4. Comparison of the SOTE in clean water with different research

No.	References	Type of diffusers	SOTE range (%)	SAFR range $\text{Nm}^3_{\text{air}}/(\text{m}^3_{\text{water}}*\text{h})$	Reactor shape	H/W or H/D
1	This study	fine-bubble disc diffuser	24.1 – 20.4	1.3 – 6.1	Rectangular	2.53
2	Collivignarelli et al. (2019)	fine-bubble side aeration	19.71 – 16.93	1.15 – 2.88	Circular	1.54
3	Pham et al. (2008)	fine-bubble disc diffuser	16.2 – 14.13	1.96 – 5.09	Rectangular	1.75
4	Dias et al. (2018)	medium-bubble grid	4.2 – 3.0	1.69 – 12.46	Rectangular	1.3
5	Sander et al. (2016)	fine-bubble disc diffuser	30 – 31	0.67 – 2.20	Rectangular	4.92



Figure 24. Comparison of the bubble plumes with different depths of submerge. The left photograph captures at 2-meter water height while the right photograph captures at 2.5-meter water height.

In addition, changes in reactor geometry highlighted certain considerable points for engineers in designing MBBR systems. One remarkable point is the minimum airflow rate to exhibit a good mixing pattern. As previously mentioned, the specific airflow rates for the pilot scale were selected based on reference studies and typical MBBR design values. The specific airflow rate to exhibit a good mixing pattern in the studies of Sander et al., (2016) and Collivignarelli et al., (2019) were 1.18 and 1.15 $\text{Nm}^3_{\text{air}}/(\text{m}^3_{\text{water}}*\text{h})$, respectively. Besides, McQuarrie and Boltz (2011) recommended the typical MBBR

design values of $6-8 \text{ m}^3/\text{m}^2_{\text{basin floor}} \cdot \text{h}$, equivalent to $1.58-2.11 \text{ Nm}^3_{\text{air}}/(\text{m}^3_{\text{water}} \cdot \text{h})$ in the pilot scale. However, in this study, none of the specific airflow rates above provided good mixing for higher filling fractions. Only the specific airflow rate of $6.1 \text{ Nm}^3_{\text{air}}/(\text{m}^3_{\text{water}} \cdot \text{h})$ exhibited a good mixing pattern for all filling fractions whereas specific airflow rates below $2.5 \text{ Nm}^3_{\text{air}}/(\text{m}^3_{\text{water}} \cdot \text{h})$ provided good mixing for filling fractions under 25%. Therefore, the specific airflow rate appeared to be not a good indicator for mixing design of the MBBR system.

Another considerable point related to reactor geometry was the SSOTE. The SSOTE values yielded in the lab scale for Disc 1 were from 8.5%/m to 7.22%/m, which were higher than values supplied by the manufacturer ranging from 7 to 6%/m. However, in the pilot scale, the SSOTE significantly decreased, ranging from 6.65 %/m to 5.6 %/m. Consequently, engineers should place more emphasis on these variations and inquire about the working depth provided by the manufacturer when selecting an appropriate SSOTE value.

5.3 Effect of the diffuser density on the oxygen transfer efficiency

With respect to the diffuser density (DD), although experiments on different DDs have yet to be conducted, it can be projected that the increase of DD will enhance the OTE. This projection is based on the idea that a higher DD implies a greater number of disc diffusers, leading to a reduction in the airflow rate for each individual disc. This reduced airflow rate, in turn, allows each disc to generate bubbles with decreased velocity, potentially facilitating more contact time between gas and liquid phases, thereby enhancing the OTE. Additionally, in alignment with the findings in this study and the values provided by the manufacturer, it was observed that the optimal SSOTE range for a single disc diffuser falls between 1.5 to 3.5 Nm³/h. A greater number of disc diffusers would bring the airflow rate applied for each disc diffuser within this range, thus improving the SSOTE for the entire system. Rosso (2018) suggested that an increase in DD could improve the OTE to a certain threshold while excessive diffusers can increase energy consumption and the risk of insufficient airflow per diffuser.

5.4 Effect of the effective water volume on the oxygen transfer efficiency

Comparing the SOTR/SOTE between different literature was challenging due to the presence of an ambiguous component, denoted as "V". Presently, many research papers determine the SOTR based on the ASCE Standard (2007):

$$SOTR = \frac{k_L a_{20} \cdot C_{20}^* \cdot V}{1000} \quad (5-1)$$

where SOTR is the standard oxygen transfer rate [$\text{kgO}_2 \text{ h}^{-1}$]; $k_L a_{20}$ is the volumetric mass transfer coefficient at 20°C and 1,013 hPa [h^{-1}], C_{20}^* is the DO saturation concentration at 20°C [mg L^{-1}]; and V is the tank liquid volume [m^3].

The ambiguity arises in whether researchers determine this volume considering only the liquid phase or include the solid phase. In this study, the liquid volume without the solid phase was referred to as "effective water volume" (V_{eff}) while the liquid volume with the solid phase was referred to as "total

water volume” (V_{total}). The selection between V_{eff} and V_{total} for calculating the SSOTE can yield significantly different results.

Table 5 presents a comparison of SSOTE values using effective water volume and total liquid volume. Statistical analysis using paired t-tests reveals that SSOTE values calculated with V_{eff} are significantly different from those with V_{total} ($p < 0.05$). Thus, misusing the total water volume instead of the effective water volume can lead to different results, with the error values increasing with higher filling fractions. As demonstrated in Table 5, at 40%, a misuse of the total water volume can result in an error of 0.19%/m – 3.5% higher than the actual value.

In fact, it is more reasonable to consider only the liquid phase when conducting oxygen transfer tests. Consequently, the effective water volume (V_{eff}) was used to calculate the SOTR/SOTE in this study. Extending this concept, Dias et al. (2018) delved even further by defining their effective water volume as the volume without any dead zones. This approach introduces more complexity due to the necessity of tracer tests for determining hydraulic efficiency. In an effort to provide a practical solution, this study introduced a method for determining the effective water volume, as detailed in Section 7.2.3.

Table 5. Comparison between SSOTE using effective water volume and total liquid volume

		SSOTE (%/m)								
		FF (%)	0	5	10	15	20	25	30	35
	Q									
	(Nm ³ /h)									
$V_{effective}$	22	6.65	6.30	6.03	5.76	5.86	6.18			
	43	6.05	5.34	5.56	5.56	5.61	5.72			
	63	5.81	4.99	5.38	5.48	5.51	5.55	5.51		
	84	5.69	4.82	5.30	5.44	5.46	5.47	5.43	5.47	
	104	5.62	4.72	5.25	5.42	5.44	5.42	5.38	5.33	5.10
V_{total}	22	6.65	6.33	6.08	5.84	5.97	6.33			
	43	6.05	5.36	5.61	5.63	5.71	5.86			
	63	5.81	5.02	5.43	5.55	5.61	5.68	5.67		
	84	5.69	4.84	5.35	5.51	5.57	5.60	5.58	5.65	
	104	5.62	4.74	5.30	5.49	5.54	5.55	5.53	5.51	5.29
Average SSOTE differences (%/m)		0.00	-0.02	-0.05	-0.07	-0.10	-0.13	-0.15	-0.18	-0.19

5.5 Limitation of the HPOD method

A drawback of the HPOD method is also exhibited in this study. The HPOD method involved introducing pure oxygen to the system while the blower operated at a low frequency. Once reaching the DO concentration of around 25 mg/L, pure oxygen was turned off and the blower could start operating at the target frequency. Oxygen transfer tests could subsequently start afterward, with the requirement of good mixing patterns already established within the tank.

At low filling fractions, the combination of oxygen and ambient air injection at low-frequency operation could provide sufficient mixing conditions within the reactor, allowing for immediate oxygen transfer

tests. However, at high filling fractions, carriers would accumulate in corners and form a thick layer on top of the reactor. This layer could not be immediately dispersed once the blower started at the target frequency, requiring time to achieve a good mixing condition. Immediate measurement initiation in such cases may yield DO probe readings in stagnant regions with kLa values 5% higher than the mean values from other regions. This discrepancy is due to the stagnant regions having higher gas holdup and displaying different hydraulic patterns.

Several solutions can be employed to address this challenge. One approach is to adjust the blower to higher frequencies while injecting oxygen to enhance mixing. Another solution involves increasing the DO concentration up to the supersaturation level and waiting for the mixing condition to be established before commencing measurements. Both of these solutions, however, come with the drawback of increased operating costs due to the additional oxygen required. A third solution, applied in this study, is to neglect the probe located in stagnant regions, resulting in slightly less reliable results as only 3 out of 4 probes are used to measure DO concentrations. An alternative solution is to consider changing the probe's position to improve measurement accuracy.

5.6 Future development of the carrier media

As previously discussed, the properties of the carrier media could impact the hydraulic characteristics of MBBR systems. In addition to the work of material modification to maximize biofilm adhesion, current literature knowledge and commercial strategies are focusing more on increasing the protected surface area (PSA), considering the PSA as a design and operational parameter in moving attached growth systems. To their consideration, a higher PSA increases biofilm concentration, thereby improving treatment capacity. Meanwhile, physical carrier properties (e.g., voidage, size and shape) are of less interest despite the fact that these properties could influence flow pathways and hydraulic velocities – factors governing the oxygen and substrate mass transfer efficiency.

Table 6 compares the SOTE development with various types of carrier media from different research. As shown in Table 6, the PSA does not exhibit a clear correlation with the SOTE, indicating that the PSA is not a good indicator for the future design of carrier media in terms of optimal aeration system. Supporting this observation, Dias et al. (2018) reported that carriers with low PSA could still achieve enhanced biofilm concentration, improved treatment performance, and better hydraulic efficiency. This further consolidates that the PSA is not a suitable parameter in future carrier media design. Instead, commercial strategies should emphasize oxygen transfer efficiency, together with biofilm growth and treatment performances, as design and operational parameters.

Since only one carrier type was investigated in this study, the impacts of the physical properties of the carriers on the oxygen transfer were not thoroughly examined. To the best of the author's knowledge, the following physical properties should be further explored in future research to improve oxygen efficiency.

(a) Voidage. Larger voidage, as suggested by Dias et al. (2018), may enhance air and wastewater distribution, increase mass transfer and encourage bacteria to attach and form biofilm.

(b) Dimension. An increase in height will result in a tube-like structure that subsequently increases the inner gas velocity, as observed in this study. By contrast, flat-shaped media with low height causes bubbles to coalesce, thus reducing oxygen mass transfer (Dias et al., 2018; Collivignarelli et al., 2019).

(c) Shape. The installation of honeycomb apertures or the arrangement of walls in a radial pattern can effectively promote the bubble-shearing effect. However, the size of the openings should not be excessively small, as this can potentially inhibit free flow and mass transfer and substrate penetration.

Table 6. Comparison of the SOTE development with various PSA from different research.

No.	References	Media type	PSA (*) (m ² /m ³)	Density (kg/m ³)	Dimension (mm)		Void (%)	Shape	FF (% (**))	Diffuser system	Effect on SOTE
					H	D					
					1	Dias et al. (2018)					
2	This study	HXF25 KLL	342	0.95	25	25	83	Cylindrical	40	Fine- bubble	Decrease
3	Dias et al. (2018)	Bio- pipe	348	0.92	13	21.5	82.5	Cylindrical	60	Medium- bubble	Increase
4	Sander et al. (2016)	SPR-1	500	0.96	10	20	-	Cylindrical	50	Fine- bubble	Increase
5	Collivignarelli et al. (2019)	Chip M	1200	1.02	2.2	48	-	Cylindrical	40	Fine- bubble	Decrease

(*) PSA: Protected surface area; (**) Maximum investigated filling fraction

6. Conclusion

Increasing demands on the treatment performance of municipal wastewater treatment plants have led to a continuous increase in space requirements and annual costs associated with the CAS process. Biofilm process, particularly MBBR, has emerged as a solution to address such challenges. In the MBBR process, very small, strongly structured plastic media are introduced to provide sites for biofilm growth. However, the main disadvantage of the MBBR process relates to the poor aeration energy efficiency while the oxygen requirement of at least double or even quintuple compared to the CAS process. This increased oxygen demand translates into higher energy consumption and associated costs. Subsequently, there is an urgent need for research to optimize the OTE in the MBBR process.

In recent years, much research has discussed factors that impact the OTE of aeration systems. Among these factors, the filling fraction of carriers and the diffuser density have been identified as significant contributors to the OTE. While it has been established that a higher filling fraction positively affects the OTE in coarse-bubble systems, the impact of filling fraction on fine-bubble systems remains a topic of debate. As a result, this study aimed to investigate the impacts of various filling fractions and diffuser densities on the oxygen transfer rate of fine-bubble aeration systems in clean water tests. Prior to this investigation, literature reviews on the fundamentals of the MBBR process were examined, covering the basic principles, technological advancements, operational parameters, and design considerations of MBBR processes. Following that, theories and mechanisms underlying mass transfer and bubble formation were assessed before the recent literature on oxygen transfer in the MBBR processes was summarized.

The results indicated that the presence of the carrier media had a positive impact on the gas holdup, but conversely had a negative effect on the SOTE in both lab- and pilot-scale settings. This could be attributed to two main factors: the vertical rotation of the carriers and the characteristics of the carrier media. The vertical rotation of the carriers exerted additional downward forces on the growing bubbles, which in turn delayed the motion of the bubbles and reduced the velocity of the liquid. As a result, this led to a higher gas holdup within the reactor. Furthermore, the vertical rotation also promoted bubble coalescence, which subsequently lowered the SOTE. Meanwhile, the characteristics of the HXF25KLL carrier media further contributed to the increased gas velocity within the carrier media. This higher gas velocity resulted in a lower contact time between the gas and liquid phases, ultimately leading to a reduced SOTE.

During the process of data collection and analysis, further notable points were discovered. In the data collection phase, it was observed that the kLa values exhibited a deviation below the regression line at higher airflow rates in the two-phase system, which, in turn, revealed that the relationship between the kLa and airflow rates did not follow in a simple linear relationship with the airflow rate. Interestingly, in a three-phase system, the presence of carrier media facilitated overcoming this deviation and establishing an enhanced linear relationship, as evidenced by increased R-squared values. Another point during the data collection was the difficulties in measuring the oxygen transfer test with the HPOD method at high filling fractions. At such filling fractions, a thick carrier layer formed on top of the reactor and could not be immediately separated once the blower started at the target frequency. Immediate measurement initiation in such cases led to DO probes in stagnant regions generating higher kLa values than the mean values observed in other regions. This discrepancy is due to the stagnant regions having higher gas holdup and

displaying different hydraulic patterns. The further work on data analysis was also challenging due to inconsistent definitions of liquid volume in order to calculate the SOTR. Thus, the effective water volume emerged as a suggested solution, shedding light and building a foundation for future studies.

Some limitations were also shown in this study. One limitation was that only one type of carrier was investigated, leading to a potential gap in understanding the diverse impact of carrier media on OTE. Despite that, the author considered that PSA would not be a suitable parameter in future carrier media design. Instead, physical properties like voidage, dimension and shape should be placed more emphasis in future studies and commercial strategies. Another limitation was that experiments on different DDs have yet to be conducted. Nevertheless, it can be projected that the increase in DD will enhance the OTE due to a reduced airflow rate applied for each disc diffuser. A reduced airflow rate applied for each disc diffuser will lead to (a) a reduced bubble velocity, which, in turn, enhances the OTE and (b) alignment of airflow rates within the optimal SSOTE range. Furthermore, the reasons behind the decrease in the OTE were not supported by evidence like hydraulic profiles, mixing indicators and bubble visualization. Hydraulic dispersion number, turbulence degree, and computational fluid dynamics (CFD) can be employed in further research to comprehensively study the complex fluid flow and mass transfer mechanisms occurring in reactors. This will not only enhance the knowledge of reactor behavior but also contribute to the successful scale-up of reactor designs.

In conclusion, the findings highlighted the complex interplay between carrier media and the OTE. The OTE was affected not only by the filling fraction of the carriers and the diffuser density, but also governed by other aspects such as the properties of the aeration system, the properties of the carrier media, the reactor geometry, and the hydraulic pattern within the reactor.

7. Appendix

7.1 Appendix A: Literature review

7.1.1 Bubble shape and rise velocity of a single bubble

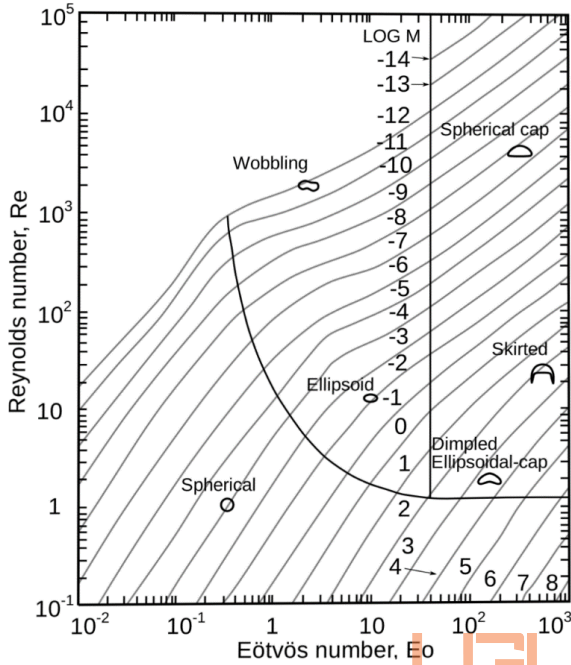


Figure APX 1. Grace Diagram for bubble shapes and bubble rise velocity.

The Morton number is denoted as 'M' in the diagram. Source: Grace et al. (1976)

The Grace diagram demonstrates the relation among three dimensionless numbers:

1. Reynolds number (Re) is the ratio between inertial forces and viscous forces. It also reflects the bubble velocity since Re is the only number of the three groups that contains the terminal velocity (Park et al., 2017):

$$Re = \frac{\rho_L \cdot v_b \cdot d_B}{\mu_L} \quad (7-1)$$

2. Eötvös number (Eo), which represents the bubble size, relates the body forces to surface tension forces (Park et al., 2017):

$$E_o = \frac{g \cdot \rho_L \cdot d_B^2}{\sigma_L} \quad (7-2)$$

3. Morton number (M), which describes the fluid properties. Generally speaking, Morton number increases with increasing viscous forces and decreasing surface tension forces (Park et al., 2017):

$$M = \frac{g \cdot \mu_L^4}{\rho_L \cdot \sigma_L^3} \quad (7-3)$$

where g is the gravitational acceleration [$\text{m}\cdot\text{s}^{-2}$]; ρ_L is the density of the liquid medium [$\text{kg}\cdot\text{m}^{-3}$]; d_B is the volume-equivalent diameter of the bubble [m]; σ_L is the surface tension of the liquid medium [$\text{N}\cdot\text{m}^{-1}$]; v_b is the terminal rising velocity of the bubble [$\text{m}\cdot\text{s}^{-1}$], and μ_L is the viscosity of the liquid medium [$\text{kg}\cdot\text{m}^{-1}\cdot\text{s}^{-1}$].

According to the Grace diagram, bubble shapes have been classified into three main groups: spherical, ellipsoidal, and spherical cap bubbles (Clift et al., 1978). Based on the bubble shapes, the bubble rise velocity can be determined by the following equations:

For spherical bubble, considering the inertial force is negligible compared to the viscous force $\text{Re} < \sim 1$:

$$v_{b,vis} = \frac{g \cdot \rho_L \cdot d_B^2}{12\mu_L} \quad (7-4)$$

For spherical bubbles with non-negligible inertial force in a Re range of $1 < \text{Re} < 100$:

$$v_{b,in} = 0.14425 \cdot g^{\frac{5}{6}} \cdot \left(\frac{\rho_L}{\mu_L}\right)^{\frac{2}{3}} \cdot d_B^2 \quad (7-5)$$

For ellipsoidal bubbles

$$v_{b,ellip} = \sqrt{\frac{2.14 \cdot \sigma_L}{\rho_L \cdot d_B} + 0.005 \cdot g \cdot d_B} \quad (7-6)$$

For spherical-cap bubbles



Vietnamese - German University

$$v_{cap} = 0.721 \cdot \sqrt{g \cdot d_B} \quad (7-7)$$

7.1.2 Force balance at the bubble surface

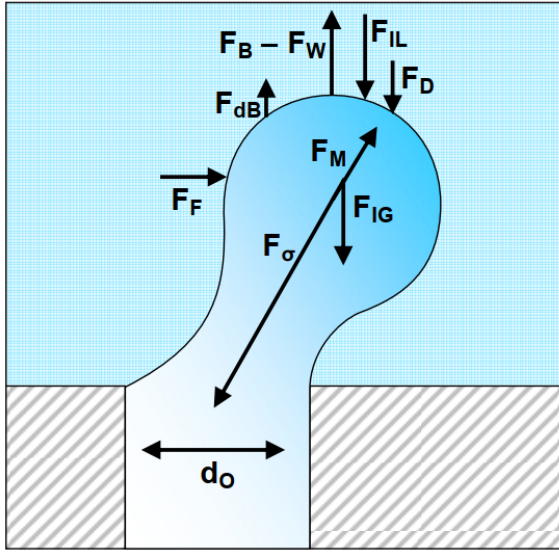


Figure APX 2. Force balance at the bubble surface. Source: (Henkel, 2010, adapted from Bals (2002)),

According to Henkel (2010), the force balance equation based on the works of Bals (2002) and Yang et al. (2007) can be expressed as follows:

$$F_{\sigma} + F_D = (F_B - F_W) + F_{IL} + F_{IG} + F_F + F_{dB} + F_M \quad (7-8)$$

where:

- F_{σ} is the Surface Tension Force at the orifice [$m \cdot \frac{N}{m}$];

- F_D is the Drag Force [$\frac{m^2}{s^2} \cdot \frac{kg}{m^3} \cdot m^2$];

- $(F_B - F_W)$ represents the Effective Buoyancy Forces [$\frac{kg}{m^3} \cdot \frac{m}{s^2} \cdot m^3$], which describes the difference between the Buoyant Force F_B and the Weight Force F_W ;

- F_F is the Fluid Flow Force [$\frac{m^2}{s^2} \cdot \frac{kg}{m^3} \cdot m^2$];

- F_{dB} is the Dynamic Buoyant Forces [$(Pa^3 \cdot m^6 \cdot \frac{kg}{m^3} \cdot \frac{1}{Pa^2 \cdot s^2})^{0.5}$];

- F_{IL} is the Liquid Inertial Force [$\frac{kg}{m^3} \cdot m^3 \cdot \frac{m}{s^2}$];

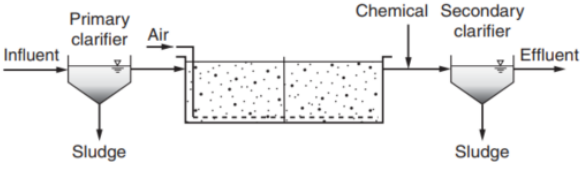
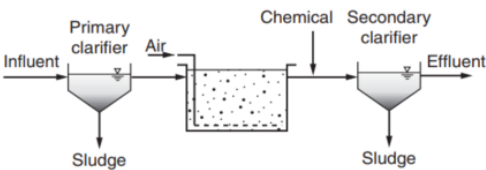
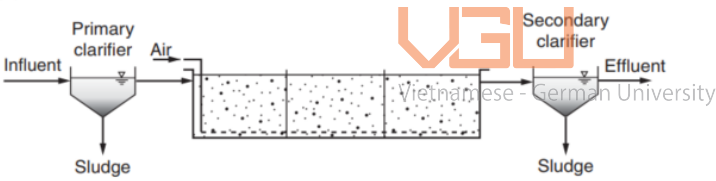
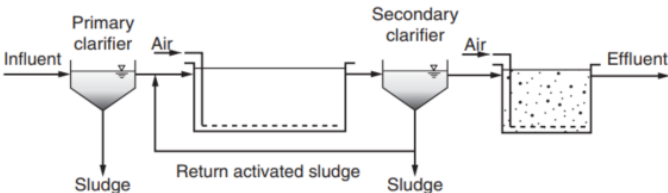
- F_{IG} is the Gas Inertial Force [$\frac{kg}{m^3} \cdot m^3 \cdot \frac{m}{s^2}$];

- F_M is the Gas Momentum Force [$\frac{1}{m^2} \cdot \frac{m^6}{s^2} \cdot \frac{kg}{m^3}$];

The detailed calculation of each force can be found in the study conducted by Henkel (2010).

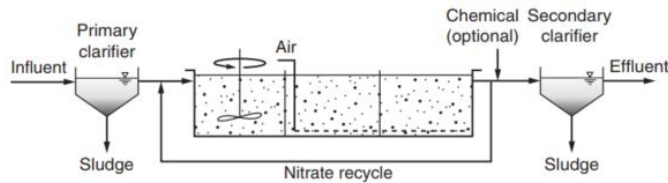
7.1.3 MBBR systems configurations for different biological treatment goals

Table APX 1: MBBR systems configurations for different biological treatment goals

Process	Description
<p>BOD removal</p> <p>(a)</p>  <p>(b)</p> 	<p>MBBR system for BOD removal and phosphorus removal by chemical precipitation. The aerobic tank may be a single or two-stage design.</p> <p>MBBR system for high rate BOD removal. Chemicals are added to provide sufficient suspended solids removal and also for phosphorus removal if needed.</p>
<p>BOD removal and nitrification</p> <p>(c)</p>  <p>(d)</p> 	<p>MBBR system for BOD removal and nitrification. Most of the BOD removal occurs in the first stage before subsequent single or multiple stage reactors for nitrification.</p> <p>MBBR system used as a tertiary nitrification process after secondary treatment for BOD removal.</p>

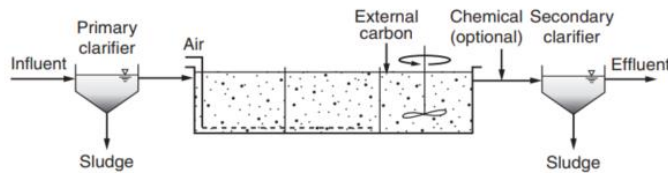
Nitrogen removal

(e)



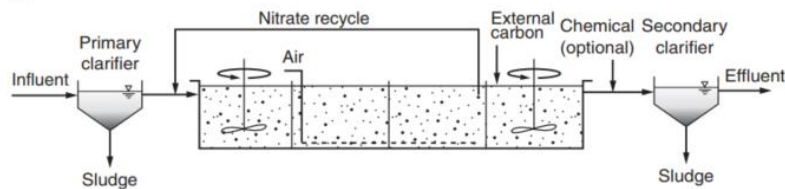
MBBR system used for MLE process with preanoxic zone and nitrate recirculation. Chemical addition before the secondary clarifier may be used for phosphorus removal (total nitrogen <math>< 10 \text{ mg/L}</math>).

(f)



MBBR system used for postanoxic biological denitrification following BOD removal and nitrification. External carbon must be added to the postanoxic reactor (total nitrogen <math>< 3 \text{ mg/L}</math>).

(g)

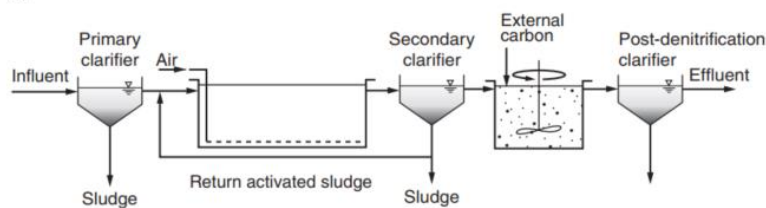


MBBR Bardenpho system for biological nitrogen removal with preanoxic and postanoxic reactors. External carbon must be added to the postanoxic reactor. Chemical addition may be used for effluent phosphorus removal and improved suspended solids removal (total nitrogen <math>< 3 \text{ mg/L}</math>).



Vietnamese - German University

(h)



MBBR system for biological denitrification after activated sludge for BOD removal and nitrification and possibly EBPR. External carbon must be added (total nitrogen <math>< 3 \text{ mg/L}</math>).

7.2 Appendix B: Experiment

7.2.1 Weekly schedules for lab- and pilot-scale experiments

Table APX 2. Weekly schedule for lab-scale experiments.

Week 1		Monday	Tuesday	Wednesday	Thursday	Friday
		17-Jul-23	18-Jul-23	19-Jul-23	20-Jul-23	21-Jul-23
Task	Morning Afternoon	Probe maintenance & calibration	Reactor cleaning	-	-	10% FF measurement (*)
	Evening					Adding carriers and allowing for complete mixing
Week 2		Monday	Tuesday	Wednesday	Thursday	Friday
		24-Jul-23	25-Jul-23	26-Jul-23	27-Jul-23	28-Jul-23
Task	Morning Afternoon	20% and then 0% FF measurement (*)	30% FF measurement (*)	40% FF measurement (*)	50% FF measurement (*)	- Reactor cleaning - Probe maintenance & calibration
	Evening	Adding carriers and allowing for complete mixing	Adding carriers and allowing for complete mixing	Adding carriers and allowing for complete mixing		
Week 3		Monday	Tuesday	Wednesday	Thursday	Friday
		31-Jul-23	1-Aug-23	2-Aug-23	3-Aug-23	4-Aug-23
Task	Morning Afternoon	0% and 10% FF measurement (**)	20% FF measurement (**)	30% FF measurement (**)	40% FF measurement (**)	50% FF measurement (**)
	Evening	Adding carriers and allowing for complete mixing	Adding carriers and allowing for complete mixing	Adding carriers and allowing for complete mixing	Adding carriers and allowing for complete mixing	

Note: (*) Measurements with Disc Diffuser type I; (**) Measurements with Disc Diffuser type II

Table APX 3. Weekly schedule for pilot-scale experiments.

Week 1		Monday	Tuesday	Wednesday	Thursday	Friday
		14-Aug-23	15-Aug-23	16-Aug-23	17-Aug-23	18-Aug-23
Task	Morning Afternoon	Probe maintenance & calibration	-	-	0% FF measurement	- Adding carriers - Probe calibration
	Evening	-	-	-	-	-
Week 2		Monday	Tuesday	Wednesday	Thursday	Friday
		21-Aug-23	22-Aug-23	23-Aug-23	24-Aug-23	25-Aug-23
Task	Morning Afternoon	10% FF measurement	10% FF measurement	Adding carriers	Waiting for complete mixing	Adding carriers
	Evening	-	-	-	-	Waiting for complete mixing

Week 3	Monday	Tuesday	Wednesday	Thursday	Friday	
	28-Aug-23	29-Aug-23	30-Aug-23	31-Aug-23	1-Sep-23	
Task	Morning Afternoon	15% FF measurement	15% FF measurement	Adding carriers	20% FF measurement	- Adding carriers - Probe calibration
	Evening	-	Adding carriers	Waiting for complete mixing	-	Waiting for complete mixing
Week 4	Monday	Tuesday	Wednesday	Thursday	Friday	
	4-Sep-23	5-Sep-23	6-Sep-23	7-Sep-23	8-Sep-23	
Task	Morning Afternoon	25% FF measurement	25% FF measurement	Adding carriers	- Probe calibration - 30% FF measurement	30% FF measurement
	Evening	-	Adding carriers	Waiting for complete mixing	-	-
Week 5	Monday	Tuesday	Wednesday	Thursday	Friday	
	11-Sep-23	12-Sep-23	13-Sep-23	14-Sep-23	15-Sep-23	
Task	Morning Afternoon	Adding carriers	- Probe calibration - Adding carriers	35% FF measurement	35% FF measurement	- Adding carriers - Regular probe maintenance + calibration
	Evening	Waiting for complete mixing	Waiting for complete mixing	-	-	Waiting for complete mixing
Week 6	Monday	Tuesday	Wednesday	Thursday	Friday	
	18-Sep-23	19-Sep-23	20-Sep-23	21-Sep-23	22-Sep-23	
Task	Morning Afternoon	40% FF measurement	40% FF measurement	Emptying the reactor	Cleaning the reactor	Repeat 0% FF measurement
	Evening	-	-	-	-	-
Week 7	Monday	Tuesday	Wednesday	Thursday	Friday	
	25-Sep-23	26-Sep-23	27-Sep-23	28-Sep-23	29-Sep-23	
Task	Morning Afternoon	Repeat 0% FF measurement	5% FF measurement	- Probe calibration	5% FF measurement	-
	Evening	- Adding carriers - Waiting for complete mixing	-	-	-	-

7.2.2 Evaluating the test quality

The test quality of each test can be evaluated by assessing the course of the residuals over time (DWA-M 209, 2007). The residuals indicate the differences between measured oxygen concentration values measured oxygen concentration values at time t and the values derived from the calculated curve which is shown in Figure APX 3. A test is considered acceptable if the residuals display a random dispersion throughout time, as illustrated at the top of Figure APX 4. Conversely, a test is unsatisfactory if the residuals trace a curved trajectory over time, indicating inadequate basin mixing, as depicted in the bottom of Figure APX 4.

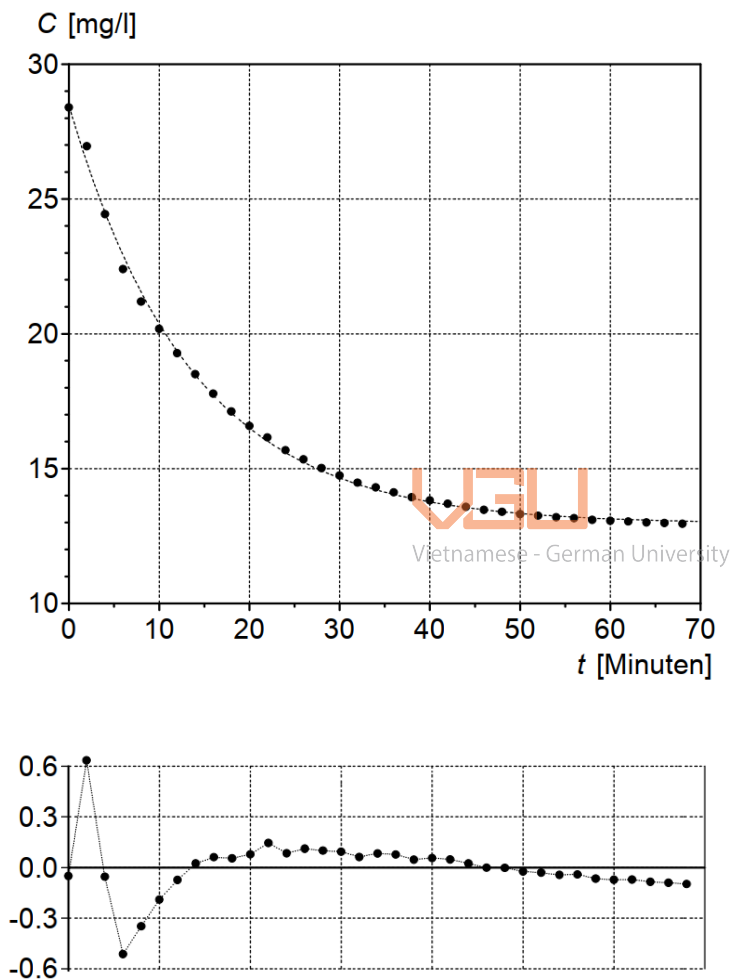


Figure APX 3. Course of the oxygen content (above) and the Residuals (below) over the measurement time.

Source: DWA-M 209 (2007)

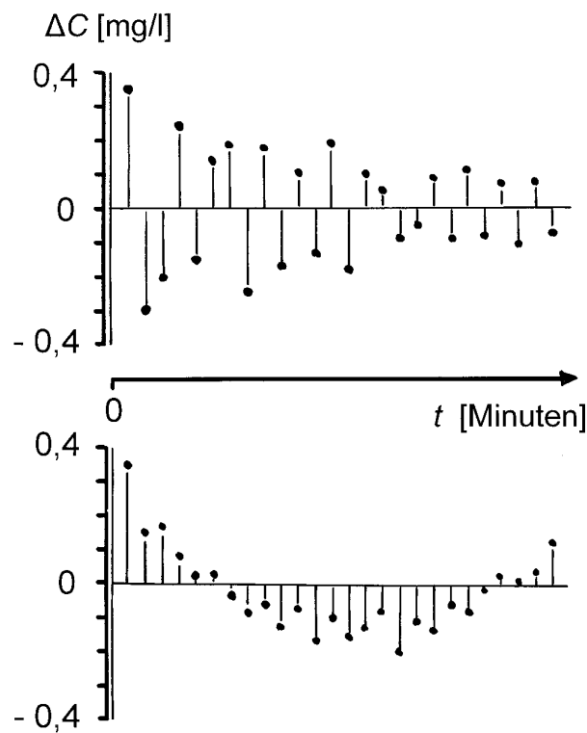


Figure APX 4. Course of the residuals of the oxygen content in a good test (top) and in a failed test (bottom)

Source: DWA-M 209 (2007)



7.2.3 Determination of the carrier's bulk volume and the effective water volume

Prior to determining the carrier's bulk volume and the effective water volume, two investigations were conducted. The first investigation focused on quantifying the number of carriers required to constitute a specific bulk volume. Using 5L plastic beakers, this investigation found that a 50L bulk volume was occupied by 2,300 HXF25KLL carriers.

The second investigation aimed to determine the mass and solid volume of the carriers in relation to their respective number. The results of this investigation are summarized in Table APX 4.

Table APX 4. Investigation of the relationship between the number of carriers, their mass and solid volume

Number of carriers (n)	Mass (M) [kg]	Solid volume ($V_{\text{solid-carrier}}$) ^(*) [L]
110	0.20	0.22
224	0.40	0.45
335	0.60	0.67
447	0.80	0.89
559	1.00	1.12
674	1.20	1.35
788	1.40	1.58
903	1.60	1.81



Number of carriers (n)	Mass (M) [kg]	Solid volume ($V_{\text{solid-carrier}}$) (*) [L]
1014	1.80	2.03
1126	2.00	2.25
1237	2.20	2.47
1351	2.40	2.70
1464	2.60	2.93
1574	2.80	3.15
1685	3.00	3.37
1795	3.20	3.59
1906	3.40	3.81
2016	3.60	4.03
2126	3.80	4.25
2240	4.00	4.48
2351	4.20	4.70
2469	4.40	4.94

(*) The plastic volume of the cylindrical HXF25KLL carrier, with a geometric volume of 12.3 cm^3 and a voidage of 83%, is calculated using the formula $V_{\text{solid-carrier}} = n \cdot (1 - \text{Void}_{\text{carrier}}) \cdot V_{\text{geo.-carrier}}$

Based on the results presented in Table APX 4, Figure APX 5 will be plotted to express the linear relationship between the mass and solid volume.

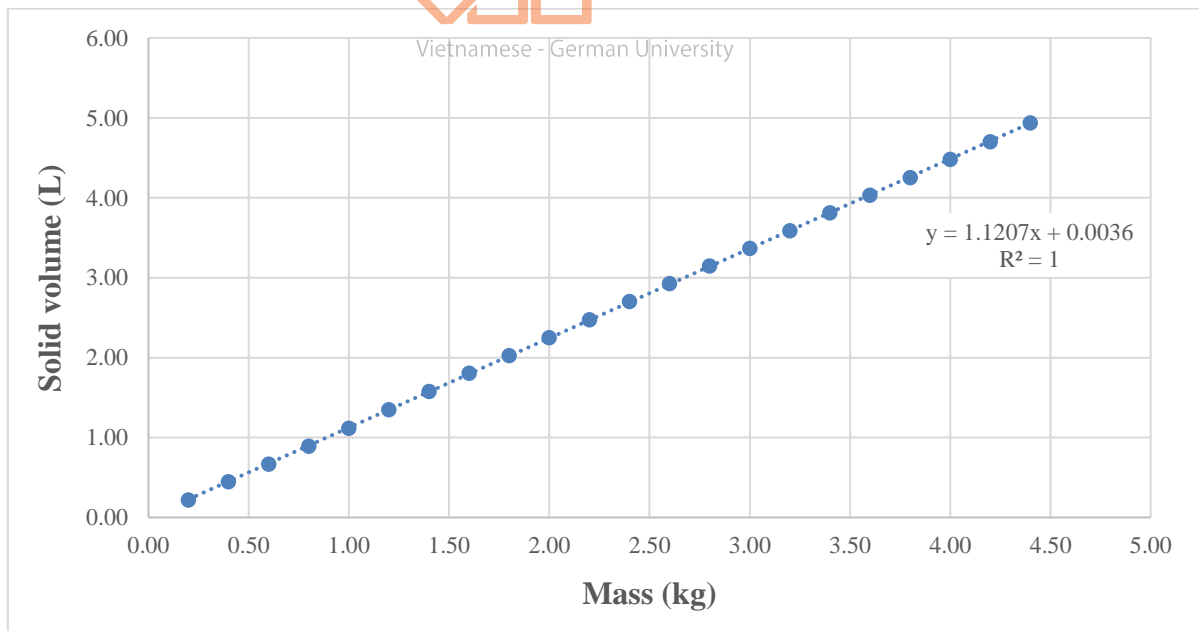


Figure APX 5. The relationship between the mass and the solid volume of the carriers.

Consequently, the effective water volume at a specific filling fraction can be yielded using Eq. (2-3).

The effective water volumes for lab- and pilot-scale experiments will be summarized in Table APX 5.

Table APX 5. Relationship between the effective water volume and filling fraction

Lab-scale			
Filling fraction	Plastic mass (kg)	Plastic volume (L)	Effective water volume (m ³)
10	1.23	1.38	0.149
20	2.46	2.76	0.147
30	3.69	4.14	0.146
40	4.92	5.52	0.144
50	6.15	6.90	0.143
Pilot-scale			
5	69.7	78.12	17.02
10	139.4	156.23	16.94
15	209.1	234.34	16.87
20	278.8	312.45	16.79
25	348.5	390.57	16.71
30	418.2	468.68	16.63
35	487.9	546.79	16.55
40	557.6	624.91	16.48

Example:

For the pilot scale, the total water volume is controlled at 17.1 m³.

- At 5% filling fraction, the carrier's bulk volume should be added, according to Eq. (2-1):

$$V_{bulk-carrier} = \frac{17.1 \cdot 1000 \cdot 5}{100} \approx 850 L$$

- According to the first investigation, a 50L bulk volume was occupied by 2,300 HXF25KLL carriers that weighed 4.1 kg in total. The carrier mass should be added:

$$M = \frac{850}{50} \cdot 4.1 = 69.7 kg$$

- Using barrels to fill the carriers into the reactor. Each barrier contained 4.1 kg of carriers; the number of carriers should be added for 5% filling fraction:

$$n_{barrel} = \frac{69.7}{4.1} = 17$$

- The solid volume of the carrier that was added, according to the second investigation:

$$V_{solid-carrier} = 1.1207 \cdot M + 0.0036 = 78.12 L$$

- The effective water volume at 5% filling fraction will be:

$$V_{eff.} = V_{total} - V_{solid-carrier} = 17.10 - \frac{78.12}{1000} = 17.02 m^3$$

A further increase of 5% will involve the same procedure, in which the total water volume is maintained at 17.1 m³ while filling in 17 barrels containing 4.1 kg carriers into the reactor.

7.2.4 Determination of the blower frequency for reaching the target airflow rate

The first important step to determine the blower frequency is collecting input parameters, as presented in the top row of Table APX 6.

Table APX 6. Investigation of the relationship between the blower frequency and the target airflow rate

Frequency (Hz)	q at To (m3)	q at T1 (m3)	T1-To (s)	qair (m3/h)	Pintake (mbar)	Tintake (oC)	Humidity (%)	Tpipe (oC)	Ppipe (mbar)	qair_stp (Nm3/h)
25.00	378.80	379.20	110	13.09	997.10	28.05	71.40	24.90	342	15.54
35.00	381.30	382.10	94	30.64	997.10	28.15	71.30	24.90	345	36.45
45.00	385.40	387.00	120	48.00	997.20	28.23	71.00	24.90	352	57.39
55.00	399.10	401.10	111	64.86	997.20	28.27	70.20	25.10	360	78.01
65.00	406.30	408.80	111	81.08	997.30	28.29	70.90	24.40	370	98.46
70.00	416.70	419.30	105	89.14	997.40	28.36	70.50	25.60	376	108.31
35.30	86.20	88.80	326	28.71	998.10	29.14	70.00	27.20	379	34.77
23.60	89.20	89.70	211	8.53	997.90	29.31	69.20	27.20	374	10.29

Based on the results presented in Table APX 6, Figure APX 6 can be plotted to express the relationship between the blower frequency with operating airflow rate and standard airflow rate.

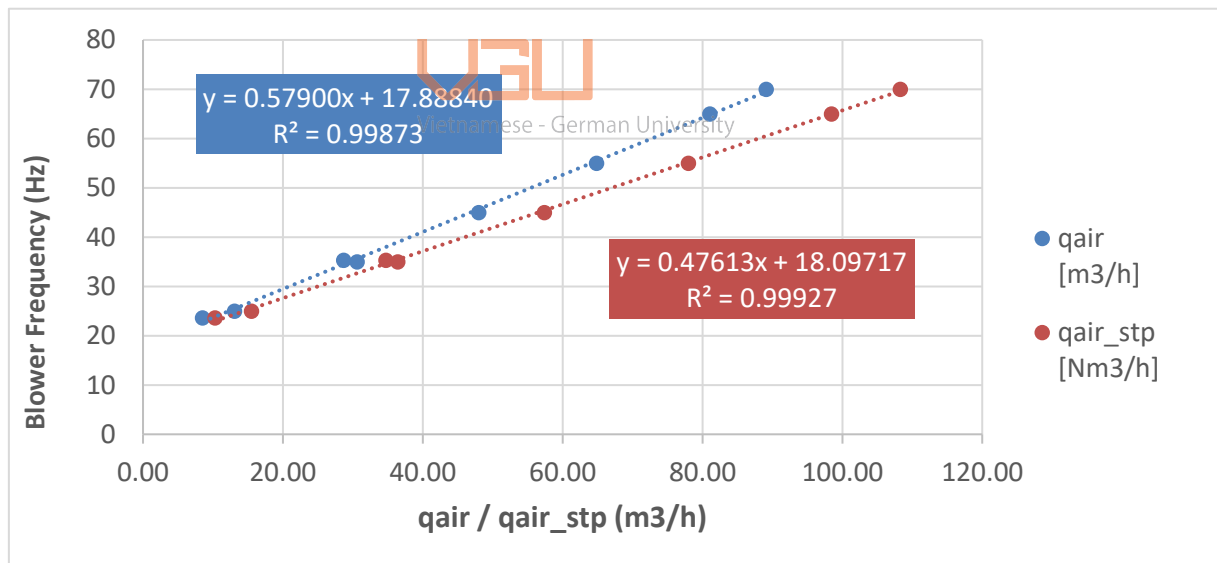


Figure APX 6. Comparison of operating airflow rate and standard airflow rate for setting blower frequency

Finally, the blower frequency can be determined from the linear equation. The resulting frequency required to achieve the target airflow rate will be summarized in Table APX 7. It is of note that these values may vary between days. Therefore, it is necessary to perform this task on a daily basis in order to ensure that the selected frequency will result in an airflow that is close to the desired target airflow.

Table APX 7. Selected blower frequency for pilot-scale experiments

q_{air,stp} [Nm³/h]	Blower Frequency [Hz]
22.23	28.7
42.75	38.5
63.27	48.2
83.79	58.0
104.31	67.8

7.2.5 Determination of the diffuser density

The first step in determining the diffuser density is to identify the effective area of each disc diffuser. It is of note that the effective area of the disc diffuser in this study is defined differently from the manufacturer. The manufacturer defines the effective area as the entire area covered by the EDPM membrane. However, in this study, the effective area is defined as the space extending from the inner slits to the outermost opening slits of the disc (see Figure APX 7). Due to the special properties offered by the manufacturer, the effective area of Disc 2 is considerably smaller than Disc 1, accounting for only 40% that of Disc 1.

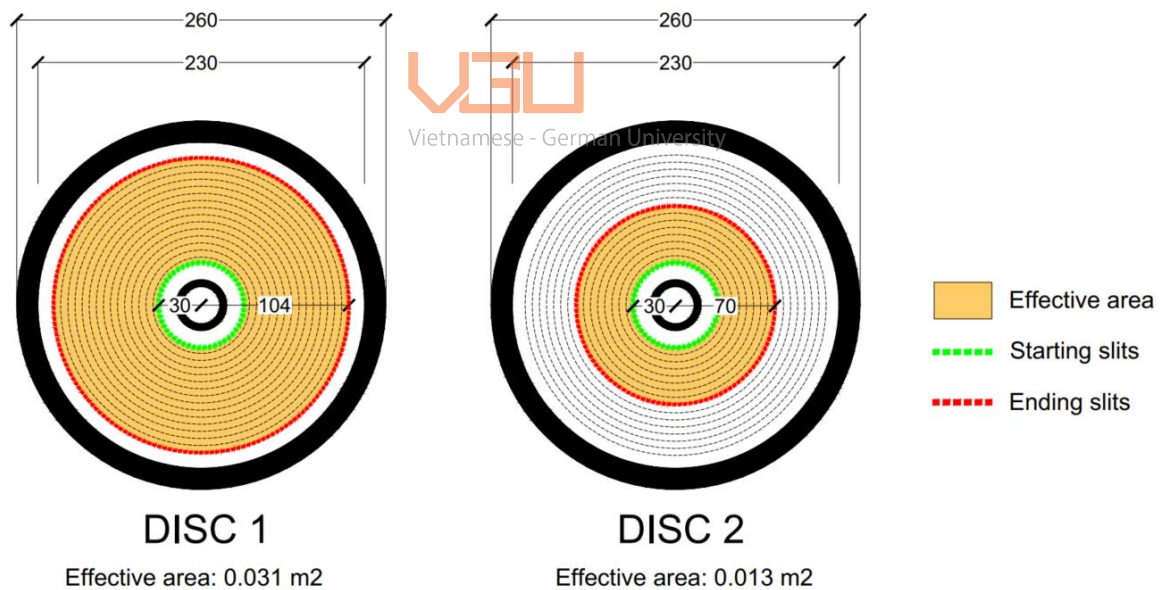


Figure APX 7. Comparison of the effective areas for Disc 1 and Disc 2

Nevertheless, the effective areas in Figure APX 7 basically indicate the theoretical values. In fact, the effective areas vary with different airflow rates (see Figure APX 8). Therefore, the next step is to determine the actual effective areas for different airflow rates, which is achieved in this study through estimation. By observation, the actual effective areas were roughly estimated by 2 steps (a) finding the radius of the outermost opening slits and (b) estimating the proportion of opening slits within the extended radius. Subsequently, the diffuser densities corresponding to distinct airflow rates for Disc 1 and 2 in lab- and pilot-scale experiments can be calculated, with the results summarized in Table APX 8 and Table APX 9.

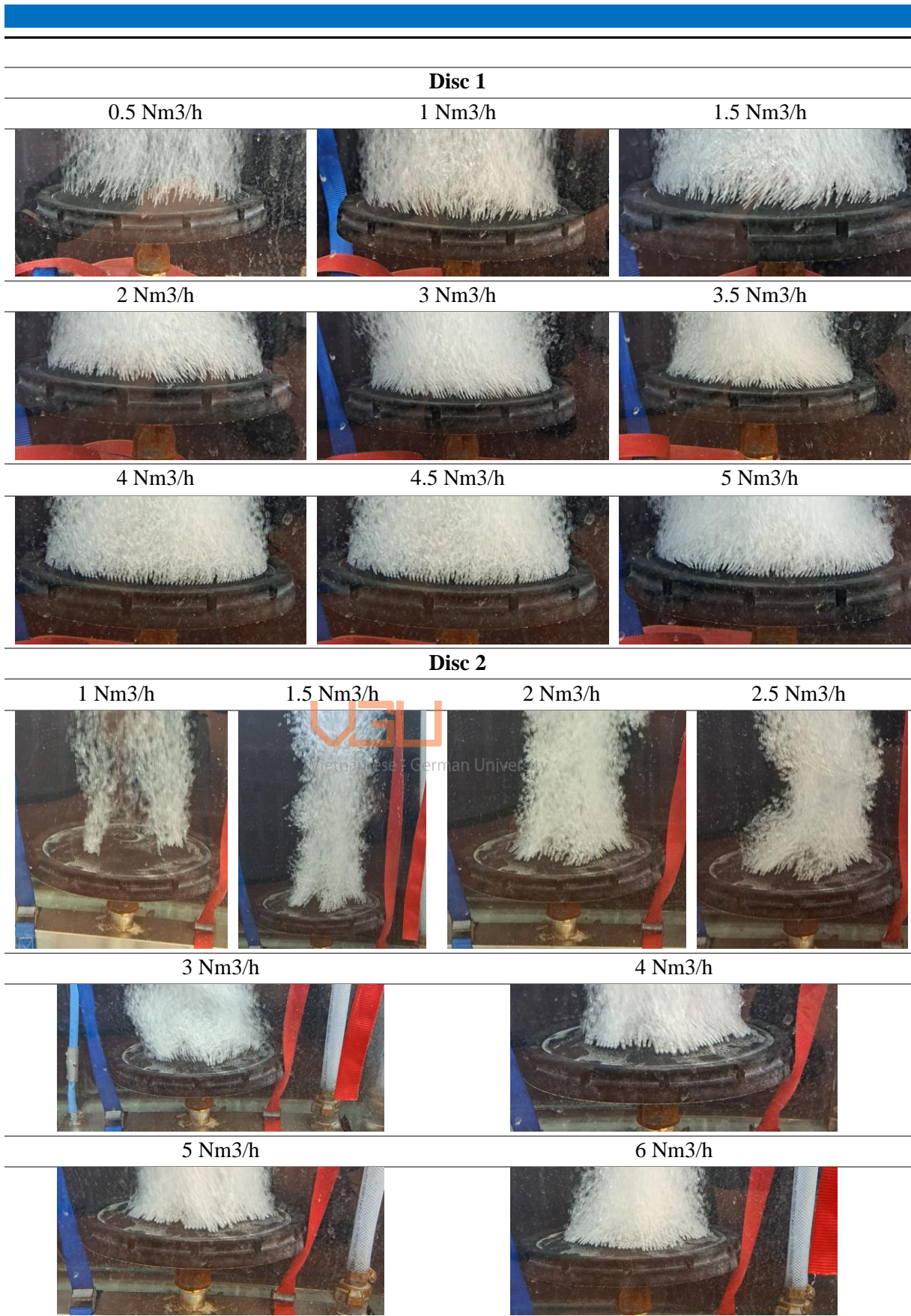


Figure APX 8. Comparison of the effective areas of Disc 1 and 2 with multiple air flow rates

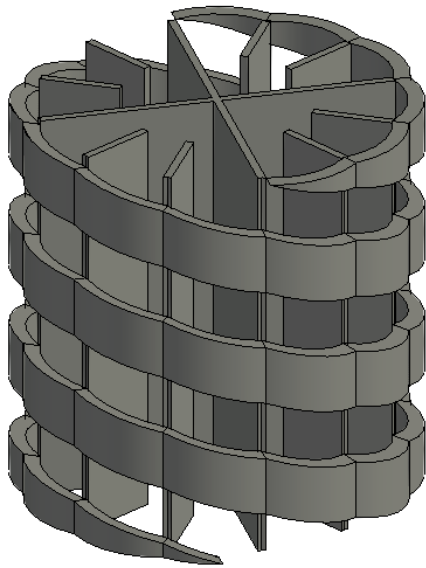
Table APX 8. Diffuser densities with different airflow rates for Disc 1 and 2 in lab-scale experiments

Disc 1							
AFR (Nm ³ /h)	Inner slit radius (m)	Outer slit radius(m)	Effective area between slits (%)	Actual effective area (m ²)	Theoretical effective area (m ²)	AEA/TEA (%)	Diffuser density (%)
0.5	0.03	0.094	50%	0.012	0.031	40%	8%
1		0.097	80%	0.021		69%	14%
1.5		0.099	90%	0.025		81%	17%
2		0.102	95%	0.028		91%	19%
2.5		0.104	95%	0.030		95%	20%
> 3		0.104	100%	0.031		100%	21%
Disc 2							
AFR (Nm ³ /h)	Inner slit radius (m)	Outer slit radius(m)	Effective area between slits (%)	Actual effective area (m ²)	Theoretical effective area (m ²)	AEA/TEA (%)	Diffuser density (%)
0.5	0.03	0.000	0%	0.000	0.013	0%	0%
1		0.055	60%	0.004		13%	3%
1.5		0.060	65%	0.006		18%	4%
2		0.070	75%	0.009		30%	6%
2.5		0.070	80%	0.010		32%	7%
3		0.070	85%	0.011		34%	7%
4		0.070	90%	0.011		36%	8%
5		0.070	95%	0.012		38%	8%
> 6		0.070	100%	0.013		40%	8%

Table APX 9. Diffuser densities with different airflow rates for Disc 1 in pilot-scale experiments

No of diffusers	Q _{total} (Nm ³ /h)	q (Nm ³ /h) per disc	AEA per disc (m ²)	AEA all discs (m ²)	Diffuser density (%)
15	22	1.48	0.025	0.3775	8.4%
	43	2.85	0.031	0.4673	10.4%
	63	4.22	0.031	0.4673	10.4%
	84	5.59	0.031	0.4673	10.4%
	104	6.95	0.031	0.4673	10.4%

7.2.6 Determination of the carrier's voidage



- Carrier information: HXF25KLL
 - Shape: Cylindrical
 - Dimensions: H * D = 25 mm * 25 mm
 - Geometric volume: 0.012 mm³
 - Solid volume: 0.002 mm³
- Void volume = $1 - \frac{0.002}{0.012} = 0.83$



Vietnamese - German University

Bibliography

- Amaral, A., Gillot, S., Garrido-Baserba, M., Filali, A., Karpinska, A. M., Plósz, B. G., De Groot, C., Bellandi, G., Nopens, I., Takács, I., Lizarralde, I., Jimenez, J. A., Fiat, J., Rieger, L., Arnell, M., Andersen, M., Jeppsson, U., Rehman, U., Fayolle, Y., Amerlinck, Y., & Rosso, D. (2019). Modelling gas–liquid mass transfer in wastewater treatment: when current knowledge needs to encounter engineering practice and vice versa. *Water Science and Technology*, *80*(4), page 607-619.
- Aqeel, H., & Liss, S. N. (2022). Fate of sloughed biomass in integrated fixed-film systems. *PLoS One*, *17*(1), page e0262603.
- ASCE. (2022). *Measurement of oxygen transfer in clean water*: American Society of Civil Engineers.
- Barwal, A., & Chaudhary, R. (2015). Impact of carrier filling ratio on oxygen uptake & transfer rate, volumetric oxygen transfer coefficient and energy saving potential in a lab-scale MBBR. *Journal of Water Process Engineering*, *8*, page 202-208.
- Biswas, K., Taylor, M. W., & Turner, S. J. (2014). Successional development of biofilms in moving bed biofilm reactor (MBBR) systems treating municipal wastewater. *Applied Microbiology and Biotechnology*, *98*(3), page 1429-1440.
- Chen, H., Wei, S., Ding, W., Wei, H., Li, L., Saxén, H., Long, H., & Yu, Y. (2021). Interfacial Area Transport Equation for Bubble Coalescence and Breakup: Developments and Comparisons. *Entropy (Basel)*, *23*(9).
Vietnamese - German University
- Chen, S., Cheng, X., Zhang, X., & Sun, D. (2012). Influence of surface modification of polyethylene biocarriers on biofilm properties and wastewater treatment efficiency in moving-bed biofilm reactors. *Water Sci Technol*, *65*(6), page 1021-1026.
- Cheng, W., Liu, H., Wang, M., & Wang, M. (2014). The effect of bubble plume on oxygen transfer for moving bed biofilm reactor. *Journal of Hydrodynamics*, *26*(4), page 664-667.
- Clift, R., Grace, J. R., & Weber, M. E. (1978). Bubbles, drops, and particles. *Dry. Technol.*, *11*, page 263-264.
- Collivignarelli, M. C., Abbà, A., & Bertanza, G. (2019). Oxygen transfer improvement in MBBR process. *Environmental Science and Pollution Research*, *26*(11), page 10727-10737.
- Daigger, G. T., & Boltz, J. P. (2018). Oxygen Transfer in Moving Bed Biofilm Reactor and Integrated Fixed Film Activated Sludge Processes. *Water Environ Res*, *90*(7), page 615-622.
- di Biase, A., Kowalski, M. S., Devlin, T. R., & Oleszkiewicz, J. A. (2019). Moving bed biofilm reactor technology in municipal wastewater treatment: A review. *J Environ Manage*, *247*, page 849-866.

-
- Dias, J., Bellingham, M., Hassan, J., Barrett, M., Stephenson, T., & Soares, A. (2018). Impact of carrier media on oxygen transfer and wastewater hydrodynamics on a moving attached growth system. *Chemical Engineering Journal*, 351, page 399-408.
- Düppe, L. (2020). What The kLa Tells You About The Oxygen Transfer In Your Bioreactor. Retrieved from https://www.infors-ht.com/en/blog/what-the-kla-tells-you-about-the-oxygen-transfer-in-your-bioreactor/?_from_store=de
- DWA-M 209. (2007). *Messung der Sauerstoffzufuhr von Belüftungseinrichtungen in Belebungsanlagen in Reinwasser und in belebtem Schlamm*.
- DWA-M 229-1. (2017). *Systeme zur Belüftung und Durchmischung von Belebungsanlagen - Teil 1: Planung, Ausschreibung und Ausführung*.
- Englande, A. J., Krenkel, P., & Shamas, J. (2015). Wastewater Treatment & Water Reclamation☆. In *Reference Module in Earth Systems and Environmental Sciences*: Elsevier.
- Fanchi, J. R. (2018). Chapter 8 - Wells. In John R. Fanchi (Ed.), *Principles of Applied Reservoir Simulation (Fourth Edition)* (pp. 139-162): Gulf Professional Publishing.
- Gao, F., Zhou, X., Ma, Y., Zhang, X., Rong, X., Xiao, X., Wu, Z., & Wei, J. (2021). Calcium modified basalt fiber bio-carrier for wastewater treatment: Investigation on bacterial community and nitrogen removal enhancement of bio-nest. *Bioresource Technology*, 335.
- Garcia-Ochoa, F., & Gomez, E. (2009). Bioreactor scale-up and oxygen transfer rate in microbial processes: An overview. *Biotechnology Advances*, 27(2), page 153-176.
- Goswami, S., & Mazumder, D. (2016). Comparative study between activated sludge process (ASP) and moving bed bioreactor (MBBR) for treating composite chrome tannery wastewater. *Materials Today: Proceedings*, 3(10, Part A), page 3337-3342.
- Grace, J., Wairegi, T., & Nguyen, T. H. (1976). Shapes and Velocities of Single Drops and Bubbles Moving Freely Through Immiscible Liquids. *Trans Inst Chem Eng*, 54, page 167-173.
- Gu, Q., Sun, T., Wu, G., Li, M., & Qiu, W. (2014). Influence of carrier filling ratio on the performance of moving bed biofilm reactor in treating coking wastewater. *Bioresource Technology*, 166, page 72-78.
- Hem, L. J., Rusten, B., & Ødegaard, H. (1994). Nitrification in a moving bed biofilm reactor. *Water Research*, 28(6), page 1425-1433.
- Henkel, J. (2010). *Oxygen Transfer Phenomena in Activated Sludge* Darmstadt.
- Herrling, M. P., Guthausen, G., Wagner, M., Lackner, S., & Horn, H. (2015). Determining the flow regime in a biofilm carrier by means of magnetic resonance imaging. *Biotechnol Bioeng*, 112(5), page 1023-1032.
- Ju, L. K., & Chase, G. G. (1992). Improved scale-up strategies of bioreactors. *Bioprocess Engineering*, 8(1), page 49-53.

-
- Kawan, J., Abu Hasan, H., Suja, F., Jaafar, O., & Abd-Rahman, R. (2016). A review on sewage treatment and polishing using moving bed bioreactor (Mbbf). *11*, page 1098-1120.
- Leiknes, T., Ødegaard, H., Andersensvei, S., & Phn. (2001). Moving Bed Biofilm Membrane Reactor (MBB-M-R): Characteristics and potentials of a hybrid process design for compact wastewater treatment plants. *The Proceeding of Engineering With Membranes, 1*.
- Li, S.-r., Cheng, W., Wang, M., & Chen, C. (2011). The flow patterns of bubble plume in an MBBR. *Journal of Hydrodynamics, Ser. B, 23(4)*, page 510-515.
- Liu, T., Jia, G., Xu, J., He, X., & Quan, X. (2021). Simultaneous nitrification and denitrification in continuous flow MBBR with novel surface-modified carriers. *Environmental Technology, 42(23)*, page 3607-3617.
- Madan, S., Madan, R., & Hussain, A. (2022). Advancement in biological wastewater treatment using hybrid moving bed biofilm reactor (MBBR): a review. *Applied Water Science, 12(6)*, page 141.
- Magdum, S., & V, K. (2017). Existing biological nitrogen removal processes and current scope of advancement. *RESEARCH JOURNAL OF CHEMISTRY AND ENVIRONMENT, 21*, page 43-53.
- Magdum, S., & V, K. (2019). Evaluation of High Rate MBBR to Predict Optimal Design Parameters for Higher Carbon and Subsequent Ammoniacal Nitrogen Removal. *Current science, 116*, page 2083-2088.
- Martín, M., Montes, F. J., & Galán, M. A. (2006). On the influence of the liquid physical properties on bubble volumes and generation times. *Chemical Engineering Science, 61(16)*, page 5196-5203.
- Martínez-Huerta, G., Prendes-Gero, B., Ortega-Fernández, F., & Mesa-Fernández, J. M. (2009). Design of a carrier for wastewater treatment using moving bed bioreactor. *Proceedings of the 2nd International Conference on Environmental and Geological Science and Engineering, EG '09*, page 44-49.
- Mayra, J., Baeza, R., Jarpa, M., & Vidal, G. (2016). Polyhydroxyalkanoate Biosynthesis from Paper Mill Wastewater Treated by a Moving Bed Biofilm Reactor. *Water, Air, & Soil Pollution, 227(9)*, page 299.
- McQuarrie, J. P., & Boltz, J. P. (2011). Moving bed biofilm reactor technology: process applications, design, and performance. *Water Environ Res, 83(6)*, page 560-575.
- Metcalf & Eddy Inc., Tchobanoglous, G., Burton, F. L., Tsuchihashi, R., & Stensel, H. D. (2013). *Wastewater engineering: Treatment and resource recovery* (5th ed.): McGraw-Hill Professional.
- Moga, I. C., Ardelean, I., Donțu, O. G., Moisescu, C., Băran, N., Petrescu, G., & Voicea, I. (2018). Materials and Technologies Used in Wastewater Treatment. *IOP Conference Series: Materials Science and Engineering, 374(1)*, page 012079.

-
- Mueller, J. A., Boyle, W., & Pöpel, H. J. (2002). *Aeration: Principles and practice*.
- Nguyen, P. T., Hampton, M. A., Nguyen, A. V., & Birkett, G. R. (2012). The influence of gas velocity, salt type and concentration on transition concentration for bubble coalescence inhibition and gas holdup. *Chemical Engineering Research and Design*, 90(1), page 33-39.
- Nogueira, R., Melo, L. s. F., Purkhold, U., Wuertz, S., & Wagner, M. (2002). Nitrifying and heterotrophic population dynamics in biofilm reactors: effects of hydraulic retention time and the presence of organic carbon. *Water Research*, 36(2), page 469-481.
- Ødegaard, H. (2006). Innovations in wastewater treatment: The moving bed biofilm process. *Water Sci Technol*, 53, page 17-33.
- Ødegaard, H., Gisvold, B., & Strickland, J. (2000). The influence of carrier size and shape in the moving bed biofilm process. *Water Science and Technology*, 41, page 383-391.
- Odize, V. O., Novak, J., De Clippeleir, H., Al-Omari, A., Smeraldi, J. D., Murthy, S., & Rosso, D. (2017). Reverse flexing as a physical/mechanical treatment to mitigate fouling of fine bubble diffusers. *Water Sci Technol*, 76(7-8), page 1595-1602.
- Pham, H., Viswanathan, S., & Kelly, R. (2008). Evaluation of Plastic Carrier Media Impact on Oxygen Transfer Efficiency with Coarse and Fine Bubble Diffusers. *Proceedings of the Water Environment Federation*, 2008, page 5069-5079.
- Rosso, D. (2018). *Aeration, Mixing, and Energy: Bubbles and Sparks*: IWA Publishing.
- Rosso, D., Lothman, S. E., Jeung, M. K., Pitt, P., Gellner, W. J., Stone, A. L., & Howard, D. (2011). Oxygen transfer and uptake, nutrient removal, and energy footprint of parallel full-scale IFAS and activated sludge processes. *Water Research*, 45(18), page 5987-5996.
- Rosso, D., & Shaw, A. R. (2015). *Framework for Energy Neutral Treatment for the 21st Century through Energy Efficient Aeration*: IWA Publishing.
- Rosso, D., & Stenstrom, M. K. (2006). Surfactant effects on α -factors in aeration systems. *Water Research*, 40(7), page 1397-1404.
- Rusten, B., Eikebrokk, B., Ulgenes, Y., & Lygren, E. (2006). Design and operations of the Kaldnes moving bed biofilm reactors. *Aquacultural Engineering*, 34(3), page 322-331.
- Safwat, S. (2019). Moving Bed Biofilm Reactors for Wastewater Treatment: A Review of Basic Concepts. *International Journal of Research*, 6, page 85-90.
- Sander, S., Behnisch, J., & Dr. Wagner, M. (2016). Energy, cost and design aspects of coarse- and fine-bubble aeration systems in the MBBR IFAS process. *Water Science and Technology*, 75.
- Santos, A. D., Martins, R. C., Quinta-Ferreira, R. M., & Castro, L. M. (2020). Moving bed biofilm reactor (MBBR) for dairy wastewater treatment. *Energy Reports*, 6, page 340-344.

-
- Sari Erkan, H., Çağlak, A., Soysaloglu, A., Takatas, B., & Onkal Engin, G. (2020). Performance evaluation of conventional membrane bioreactor and moving bed membrane bioreactor for synthetic textile wastewater treatment. *Journal of Water Process Engineering*, 38, page 101631.
- Schwarz, M., Behnisch, J., Trippel, J., Engelhart, M., & Dr. Wagner, M. (2021). Oxygen Transfer in Two-Stage Activated Sludge Wastewater Treatment Plants. *Water*, 2021, page 1964.
- Sonwani, R. K., Jaiswal, R. P., Rai, B. N., & Singh, R. S. (2022). Chapter 15 - Moving bed biofilm reactor- (MBBR-) based advanced wastewater treatment technology for the removal of emerging contaminants. In Maulin Shah, Susana Rodriguez-Couto, & Jayanta Biswas (Eds.), *Development in Wastewater Treatment Research and Processes* (pp. 349-370): Elsevier.
- Sun, L., Zhang, F., Liu, C., Bi, X., Cheng, L., Li, S., Liu, Y., & Qiao, Z. (2015). Effect of bio-carrier filling rate on oxygen transfer coefficient of different diffusers in MBBR process. *Desalination and Water Treatment*, 57, page 1-6.
- Suriasni, P., Faizal, F., Panatarani, C., Hermawan, W., & Joni, I. M. (2023). A Review of Bubble Aeration in Biofilter to Reduce Total Ammonia Nitrogen of Recirculating Aquaculture System. *Water*, 15, page 808.
- Tang, K., Ooi, G. T. H., Litty, K., Sundmark, K., Kaarsholm, K. M. S., Sund, C., Kragelund, C., Christensson, M., Bester, K., & Andersen, H. R. (2017). Removal of pharmaceuticals in conventionally treated wastewater by a polishing moving bed biofilm reactor (MBBR) with intermittent feeding. *Bioresource Technology*, 236, page 77-86.
- Tao, F., Ning, S., Zhang, B., Jin, H., & He, G. (2019). Simulation Study on Gas Holdup of Large and Small Bubbles in a High Pressure Gas-Liquid Bubble Column. 7(9), page 594.
- Vanags, J., & Suleiko, A. (2022). Oxygen Mass Transfer Coefficient Application in Characterisation of Bioreactors and Fermentation Processes. *Latvian Journal of Physics and Technical Sciences*, 59, page 21-32.
- Von Sperling, M. (2007a). *Activated Sludge and Aerobic Biofilm Reactors*: IWA Publishing.
- Von Sperling, M. (2007b). *Basic Principles of Wastewater Treatment*: IWA Publishing.
- Von Sperling, M. (2007c). *Wastewater Characteristics, Treatment and Disposal*: IWA Publishing.
- Wagner, M. R., Pöpel, H. J., & Kalte, P. (1998). Pure oxygen desorption method — A new and cost-effective method for the determination of oxygen transfer rates in clean water. *Water Science and Technology*, 38(3), page 103-109.
- WEF. (2011). *Biofilm Reactors*. WEF Manual of Practice No. 35. Water Environment Federation.
- Wei, Y., Yin, X., Qi, L., Wang, H., Gong, Y., & Luo, Y. (2016). Effects of carrier-attached biofilm on oxygen transfer efficiency in a moving bed biofilm reactor. *Frontiers of Environmental Science & Engineering*, 10(3), page 569-577.

-
- Yang, G. Q., Du, B., & Fan, L. S. (2007). Bubble formation and dynamics in gas–liquid–solid fluidization—A review. *Chemical Engineering Science*, 62(1), page 2-27.
- Yang, W., Wang, J., Wang, T., & Jin, Y. (2001). Experimental study on gas–liquid interfacial area and mass transfer coefficient in three-phase circulating fluidized beds. *Chemical Engineering Journal*, 84(3), page 485-490.
- Zhang, F., & Thoroddsen, S. (2008). Satellite generation during bubble coalescence. *Physics of Fluids - PHYS FLUIDS*, 20.
- Zhao, Y., Cao, D., Liu, L., & Jin, W. (2006). Municipal Wastewater Treatment by Moving-Bed-Biofilm Reactor with Diatomaceous Earth as Carriers. *Water environment research : a research publication of the Water Environment Federation*, 78, page 392-396.
- Zhou, D. (2013). Activated carbon fiber felt and polymer fiber as biofilm carrier in a modified University of Cape Town process for sewage treatment. *Water Sci Technol*, 68(5), page 1151-1157.
- Zhuang, H., Han, H., Jia, S., Zhao, Q., & Hou, B. (2014). Advanced treatment of biologically pretreated coal gasification wastewater using a novel anoxic moving bed biofilm reactor (ANMBBR)–biological aerated filter (BAF) system. *Bioresource Technology*, 157, page 223-230.



Vietnamese - German University

Affidavit

Thesis Statement pursuant to § 22 paragraph 7 of General Examination Terms (GET) of the Technische Universität Darmstadt

I herewith formally declare that I, Thinh Vo Truong, have written the submitted thesis independently pursuant to § 22 paragraph 7 of General Examination Terms of the TU Darmstadt. I did not use any outside support except for the quoted literature and other sources mentioned in the paper. I clearly marked and separately listed all of the literature and all of the other sources which I employed when producing this academic work, either literally or in content. This thesis has not been handed in or published before in the same or similar form.

I am aware, that in case of an attempt at deception based on plagiarism (§38 Abs. 2 GET), the thesis would be graded with 5,0 and counted as one failed examination attempt. The thesis may only be repeated once.

Date:

25/11/2023

Signature



VGU
Vietnamese - German University